Polymer Theory Applied to the Nuclear Pore Complex

Dino Osmanović

London Centre for Nanotechnology
Department of Physics and Astronomy
University College London

October 16, 2014

Thesis submitted for the degree of Doctor of Philosophy

I, Dino Osmanović, confirm that the work presented in this thesis is my own. Where information has been derived from other sources, I confirm that this has been indicated in the thesis.

Abstract

Physically interesting behaviour can arise when soft matter is confined to nanoscale dimensions. A highly relevant biological example of such a phenomenon is the Nuclear Pore Complex (NPC), found perforating the Nuclear Envelope of all eukaryotic cells. In the central conduit of the NPC, of 30-60 nm diameter, a disordered arrangement of proteins regulates all macromolecular transport between the nucleus and the cytoplasm. Its selectivity for larger macromolecules relies on changes in a permeability barrier that is formed by these unstructured proteins, induced by interactions of these proteins with molecules called Nuclear Transport Receptors (NTRs), which can chaperone larger macromolecules through the NPC. The exact mechanism for the transport selectivity is unknown.

To model these unstructured proteins in the nanoscale channel of the NPC, a density functional theory approach is developed that treats the proteins as interacting polymers. This new method is tested against Monte Carlo to show its validity. A detailed comparison between this model system and those previously proposed in the literature is provided. In a parameter range relevant for the NPC, the system shows bimodal behaviour The polymers can alternate between two condensed states: An open state, in which this condensation takes place at the channel wall, and a closed state in which it occurs at the channel centre.

We then extend this model by including explicitly the effect of Nuclear Transport Receptors on the conformations of the polymers. The model takes into account the finite size of the transport receptors relative to the NPC diameter. Mapping the polymer and transport receptor behaviour over a set of physiologically relevant parameters gives different structural scenarios for the various hypothesized transport mechanisms. Further to this, the transport rates for each parameter set can be obtained, showing whether such parameters are consistent with experimental evidence.

In addition to this, we study the effect of relaxing some of the assumptions of our model, specifically by looking at azimuthal symmetry breaking effects in two dimensions. We also compare our model to experimental results measuring the thickness of planar polymer brushes comprised of NPC proteins to further justify parameter choices.

Acknowledgements

I'd like to thank my primary supervisors, Ian Ford and Bart Hoogenboom, for their guidance and support during my research. I extend my thanks to Ariberto Fassati, my secondary supervisor for his input into this work and providing a biological perspective. I'd like to thank the Sackler Foundation and University College London for co-funding my PhD. My gratitude also to my friends and family for their moral support during the years I undertook this work.

Contents

Chapter 1

Introduction to Modelling of the Nuclear Pore Complex

Confinement in soft matter has important implications in biological contexts, for example in the Nuclear Pore Complex (NPC), where unstructured proteins are confined within a roughly cylindrical channel. They are able to perform a highly delicate gating function.

This thesis focusses on the application of physical modelling techniques to determine the conformation of the unstructured proteins. This chapter gives an introduction to the Nuclear Pore Complex and previous attempts to model it.

All eukaryotic cells are subdivided into a nucleus and a cytoplasm. These two compartments of the cell are separated by the Nuclear Envelope, a double membrane which surrounds the nucleus. Permeating the Nuclear Envelope is the Nuclear Pore Complex. The NPC is the main path for translocation of macromolecules between the nucleus and the cytoplasm. It is one of the largest protein complexes within the cell. Its structure and function has been subject to considerable experimental work [1]. The various methods employed, such as cryoelectron tomography, co-immunoprecipitation, fractionation, X-ray crystallography and structural modelling [2, 3], have given us an understanding of the structure of the NPC.

A schematic of the NPC is shown in figure 1.1A. It has an eight-fold symmetry around the central axis, having an outer diameter of 90-120 nm, a height of 30-50 nm and consisting of multiple copies of about 30 different types of proteins, called nucleoporins or nups. There are distinct classes of nups; some are structural and constitute the NPC scaffold, others are non-structural, called phenylalanine-glycine repeat containing nups (FG nups). FG nups contain long natively

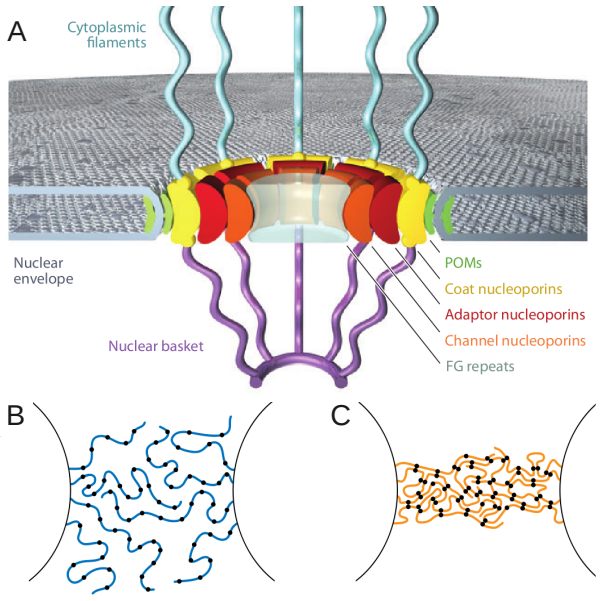

Figure 1.1: A) Simplified representation of the Nuclear Pore Complex, showing approximate locations of natively unfolded proteins within the pore. The disordered FG nups extend through the pore and collectively make up the permeability barrier. Reproduced from Hoelz et al (2011)[1]. B and C show different proposed models for the nature of this barrier. B has more freely fluctuating polymers, as in the virtual gate model, which would maintain a permeability barrier through entropic exclusion. C is the selective phase model, where the polymers interact to form a highly cross-linked gel, forming an energetic barrier to transport.

disordered protein regions, which are enriched by Phe-Gly dipeptides. In addition to this, the FG nups contain structured domains that anchor them to the structural nups. The structural nups form a cytoplasmic and a nuclear ring and delimit a central channel, which is filled by the unfolded FG domains. Transport of macromolecules is via the central conduit of ~30-60 nm diameter, which contains a selective barrier [4]. The barrier allows passive diffusion of solutes less than 5-6 nm in diameter, but prevents passage of inert molecules larger than 9 nm in diameter unless they are chaperoned by Nuclear Transport Receptors (NTRs)[5]. All macromolecules (cargoes) that are transported through the pore contain a Nuclear Localization Signal or a Nuclear Export Signal that binds to a NTR and the NTR bound cargo can then diffuse through the pore. NTRs can be classified as a *importin* if they bind to Nuclear Localization Signals or *exportin* if they bind to Nuclear Export Signals.

Transport through the NPC is directional such that many cargoes are only imported into or

exported from the nucleus, although other cargoes do shuttle in and out continuously. Directionality of transport is mediated by RanGTP gradient across the Nuclear Envelope. The small GTPase Ran in its GTP bound form, induces dissociation of cargoes with a Nuclear Localization Signal from the NTRs. Conversely, it promotes association of cargoes with an Nuclear Export Signal to the NTRs. NTRs, on the other hand, shuttle freely between nucleus and cytoplasm[5]. The RanGTP gradient, high in the nucleus and low in the cytoplasm, ensures that association and dissociation of NTRs and their cargoes happens in the right place and in a directional way [6, 7]. The Ran gradient provides the energy for the entire process of transport, however, individual transport events do not require extra energy input.

Transport of cargoes through the NPC critically depends on the intermolecular interactions between NTRs and nups. NTRs bind to the FG domains of nups via hydrophobic interactions, which must be finely calibrated to allow translocation and final detachment [8, 9, 10, 11]. The complexity of such interactions is further highlighted by the co-existence of different nups with different properties in the central channel [4, 12]. Yet their overall organisation and properties are imperative for the functioning of the permeability barrier, which has a remarkable efficiency allowing 1,000 translocation events per second per NPC [13] and passage of very large complexes, including viruses [14], up to the size of baculovirus with dimensions 30-60 nm in diameter and a length of 250-300 nm [15]. Translocation of a small NTR bound cargo through the barrier is also fast, taking approximately 10 milliseconds [16, 17].

The transport mechanism is generally thought to be strongly dependent on hydrophobic interactions between FG-repeats on the nups and the NTRs [18]. It has also been found that the depletion of certain, more cohesive nups causes the NPC to lose its functionality [19]. To understand the transport mechanism, it is paramount to know the arrangement of the nups that make up the $\sim$30-60 nm diameter central channel. These nups are natively unfolded and intrinsically disordered, however, greatly complicating experimental approaches to study their structure. For example, there is experimental evidence for a "central plug" or "central transporter" in the centre of the channel, but it is still unclear whether this plug is caused by the FG nups themselves or by cargoes passing through the pore. The behaviour of FG-nups in the NPC central channel thus represents a still poorly understood example of confined matter, which is literally vital for the cell (non-functional NPCs can lead to cell death [8]).

1.1 Qualitative models of the NPC

Several simplified and often conflicting paradigms of the NPC barrier have been suggested. The proposed nature of the permeability barrier is dependent on nup cohesiveness. There has been debate about whether the barrier facing inert (i.e. not bound to a NTR) cargoes is mainly entropic or energetic in nature. The virtual gate model[20] (see figure 1B) suggests that the barrier is entropic. In this model the nups within the central channel of the pore are mainly freely fluctuating and non-cohesive, such that any non-NTR bound cargo would be subject to frequent impacts with the nups. NTRs in NTR bound cargo can bind to the FG repeat regions of the nups, thus paying the entropic cost and allowing transport.

At the other end of the spectrum, the selective phase model[13], (see figure 1C) posits that the barrier is mainly energetic. The FG nups within the pore bind strongly to one another, forming a dense gel across the NPC. NTR bound cargoes can pass through by the binding of those NTRs to the FG repeats, with a greater affinity than the FG repeats bind to one another, thereby reversibly dissolving the gel and allowing transport of larger cargoes.

The reduction of dimensionality model [21] for transport supposes that the FG repeats form a film on the circumference of the channel, such that NTR bound cargoes slide across this surface, in effect reducing the dimensionality of the random walk, thus increasing translocation rates for the cargoes. This model postulates that there are also some freely fluctuating peptides in the central channel, meaning non-NTR bound cargoes are kept out by entropic exclusion in the same manner as the virtual gate model.

Such models as these are phenomenological approaches to the question of the nature of the barrier of the NPC, and their predictions are based upon assumptions about the way that FG nups interact with one another. One would prefer to make more quantitative models of NPC function.

Whilst a lot of experimental work has been done on the nature of the NPC, theoretical modelling has so far made a more modest contribution towards our understanding of the NPC. Problems faced in the modelling of the NPC include the complexity of the intermolecular interactions, the full form of which remains unknown. Additionally, the large number (~ 600) of proteins within the NPC make a full computational treatment very difficult. In order to model the NPC, simplifying assumptions are usually applied. For instance, it is convenient to treat the NPC as a cylindrical channel with a ring of polymers representing the FG nups anchored around the circumference of

the cylinder.

The methods used to model the NPC can be broadly split into a few categories, In the "jigsaw puzzle" approach one attempts to incorporate the detailed structure of all individual nups, while neglecting the possibility of significant structural rearrangement due to intermolecular interactions. In the "diffusion equation" approach most structural detail is neglected while focussing on the general characteristics of transport. Other approaches ("molecular dynamics" and "mean-field calculations") include explicit macromolecular arrangements and intermolecular interactions, generally requiring significant simplification of the nups under study, and/or the geometry of the system.

Here we will review the various approaches. We note that there is significant overlap between the question of modelling the NPC and modelling any polymer-grafted pore[22], with any results obtained having general significance in this field. Polymer-grafted pores have possible technological applications to, among others, DNA sequencing or microfluidic control devices [23].

1.2 Jigsaw puzzle approach

One approach to determining the configuration of nups within the pore is to attempt to fit together the nucleoporins from their partially known experimental structures and affinities [24]. The experimental data for such calculations can come from a wide variety of sources such as electron microscopy or sedimentation analysis. Combining all the experimental data using specialised algorithms can give an account of the structure of the NPC. This model predicts a core scaffold, a structured network of nucleoporins coating the channel wall of the NPC. Extending from this core scaffold are the disordered FG nups. The FG nups do not extend all the way to the centre of the channel, thus according to this approach the central plug structure seen in experiments would not be caused by the constituent proteins of the NPC. These FG nups provide an effective reduction in diameter of the NPC, allowing diffusive transport of cargoes smaller than the effective pore diameter. Specificity of transport is caused by entropic exclusion.

Other examples of this type of method can be found in the paper by Yamada et al [25]. Again, by combining the results of single-nup experiments and single nup simulations, they attempt to reconstitute the NPC. Different varieties of nups were identified by this approach. There exist nups which adopt extended coil configurations and those that adopt, at least partially, more globular

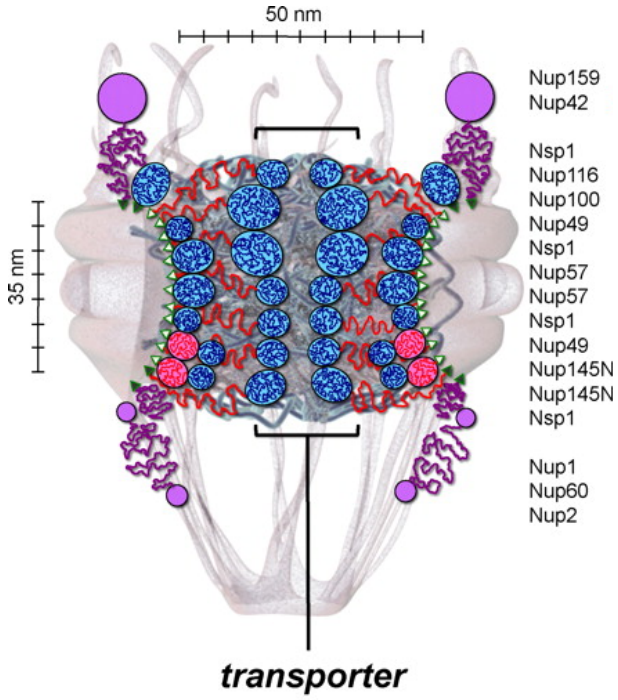

Figure 1.2: An overview of the likely positions for different types of nups within the NPC, as derived from a "jigsaw puzzle approach". The form of the nups is obtained from single-nup experiments and simulations. This information is then used to fit the nups together into a pore structure. The nups have a collapsed/extended dichotomy. The extended nups would be responsible for the "central plug" or "central transporter" mentioned previously.

shapes. One may also find hybrids of these two. The model which fits together all of these nups is described as the "forest" model (see figure 1.2). Amongst the predictions of this model is that there exist multiple transport channels for cargoes. It is suggested that the NPC is a chemically heterogeneous, partially organised structure. This is in contrast to the random coil nature of the nups suggested by the other models of NPC transport.

These methods do not model interactions between the different nucleoporins comprehensively so it is unknown whether a full treatment of interactions would result in a differing structure. The dynamics of such models are also difficult to gauge, especially if the nucleoporins undergo significant restructuring to accommodate NTR bound cargoes. Nevertheless they can give a general overview of likely arrangements of the nups within the NPC.

1.3 Diffusion equations

Perhaps the simplest approach to understand the NPC is to model the entire process of transport as a diffusive process [26, 27, 28, 29, 30]. Such problems bear similarity to evaporation problems [31], where a particle, in this case a cargo, must ascend over a free energy barrier. The general form of the free energy barrier can be estimated using simple physical arguments or calculated using more advanced methods such as Monte Carlo.

These models can be solved numerically without too much difficulty, allowing us to look at transport rates over a range of parameters such as cargo size and interactions between NTR/cargo complex and the nups. For instance, such calculations can confirm the intuitive idea that there exists an optimal binding between the nups and the NTR/cargo complex for greatest transport efficiency[28, 27]. If the interactions were absent then the cargo/NTR complex would not enter the pore. If they were too strong, however, then once the NTR/cargo complex has bound to an FG repeat it would not dissociate and the cargo would be stuck in the pore, blocking transport of other cargoes.

This can be extended further to attempt to understand the selectivity barrier of the NPC. For example, it has been suggested that the barrier is enhanced by the competition between NTR bound cargoes and inert cargoes[29]. Due to the large rate of transport of cargoes through the NPC, any macromolecular cargo which enters the pore will likely find another cargo in the process of being transported ahead of it. Non-NTR bound cargoes do not have long wait times in the pore, due to lack of interactions between the nups and the NTR. Such an inert cargo is thus more likely to be ejected from the pore through diffusion before the cargo already within the pore has translocated. Due to the interactions between the NTR and the nup, an NTR bound cargo will reside longer in the pore, making it more likely that it will still be within the pore once the other cargo has translocated. In this way the permeability barrier of the pore can be amplified just by the presence of other cargoes.

Diffusion equation modelling of the pore can also give a useful starting point for more elaborate calculations.

1.4 Molecular dynamics

Large-scale molecular dynamics (MD) simulations are now the norm in research into protein structure[32]. This approach is based on solving the equations of motion for every particle in the system. For example, MD can be used to study how proteins fold into their three-dimensional structures. By calculating all the pairwise interactions of the particles, these methods are amongst the most accurate ways of determining structures of large ensembles of interacting particles, and additionally the approach allows us to look at the evolution of structures for short time-scales, though the computational cost of such simulations scales rapidly with the complexity of the system and the process time. A difficulty facing modelling the NPC in such a way is that there about 600 proteins within the pore, making full molecular dynamics simulations of the NPC infeasible.

One of two approaches is then typical: either one can model a smaller system with full detail[33] and attempt to infer the full structure from this subsystem, or one can coarse-grain the nups to make molecular dynamics more tractable[34, 35].

Due to the computational cost associated with these approaches, the first studies in this field were obliged to use both assumptions [36]. These early approaches dispense with most of the detail of the pore in an attempt to gain a qualitative account of transport. Despite their simplicity, these simulations give a useful way to test the validity of the different models of barrier organisation. By assuming *a priori* that the centre of the pore is blocked by a network of FG nups, one can test whether the physical mechanisms proposed by such models are realistic. The mesh size of the network gives a size limit for passive diffusion. Particles larger than the mesh size can diffuse through as long as they are bound to an NTR. As postulated by the selective phase model, NTR bound cargoes cause local breakage of the network, thus allowing diffusion of cargoes through the mesh.

When attempting to model a coarse-grained NPC with MD, the form of the interaction can be chosen to represent hydrophobic interactions, which are known to be important among the FG nups. The following form, with some variations, can be used to represent short range repulsion and attractive (e.g hydrophobic) interactions [37]:

$$\phi(\mathbf{r}) = \begin{cases} \infty & |\mathbf{r}| < d \\ \epsilon \exp(-(|\mathbf{r}| - d)/\lambda) & |\mathbf{r}| \geq d \end{cases} \tag{1.1}$$

The parameter ϵ is usually negative, accounting for the fact that the FG repeats are attractive

to one another [38]. d is the diameter of the part of the nup under consideration, usually taken to be spherical for simplicity and λ gives the length scale of the interaction, which is not thought to be more than 1 nm.

The NPC contains many different types of nups, with hydrophilic and hydrophobic domains. Choosing this form of the interaction is implicitly assuming that hydrophobic interactions are the most important interactions in the NPC, though not without experimental justification [39, 40].

The resultant structure of the nups depends upon the parameters chosen to represent the system. MD simulations of cylindrically confined tethered polymers show interesting phase behaviour. Depending on the mutual polymer interaction, one of two regimes is possible. The polymers can swell away from their tethering points, thus blocking the channel, or can collapse back to their tethering points, leaving the centre open. The difference in permeability of these states can be as much as an order of magnitude[41].

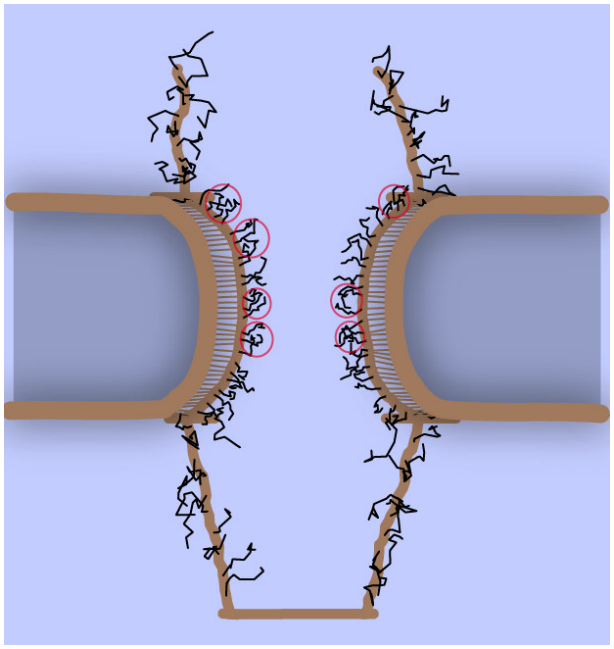

Figure 1.3: Snapshot from a equilibrated MD simulation of a simplified model of nups in the pore. In this simulation, the nups are treated as homopolymers tethered around the edge of an hourglass structure. The black lines represent the nups, in a conformation near the walls of the channel.

These simulations have given support to differing models for transport. In MD simulations, one introduces inert and NTR bound cargoes on one side of the pore and then measures the rate at which these particles translocate to the other side. It has been suggested, with regard to transport, that the NTR/cargo complex remains bound to the same FG nup during its entire translocation.

Once the NTR portion of the NTR/cargo complex is bound to an FG nup, the cargo can diffuse through the pore whilst the FG nups reorganise around it. The cargo is released by RanGTP on the nucleoplasmic side. The required rearrangement of FG nups around the transporting cargo means that greatest transport efficiency is achieved when the FG nups do not interact with one another, providing evidence against the "selective phase" idea. Entropic exclusion alone was found to be enough to exclude non-NTR bound cargo[34].

A more realistic treatment of the interactions [35] using a model similar to equation (6.1) can develop the picture even more. The NTR bound cargo remains bound to FG nups for the majority of its translocation, though not necessarily the same one. The FG nups were found to collapse onto the channel wall, forming a dense gel of FG repeat regions (as in figure 1.3). During translocation cargoes slide across this gel, in the manner suggested by the reduction of dimensionality model. Calculations of translocation times of cargoes in these models can lead to order of magnitude estimates that compare favourably with experiment, even though the pore channel appears remarkably open, in contrast to experimentally observed structures such as the central plug mentioned earlier.

Recently, molecular dynamics modelling of the NPC has been increasing in sophistication[42]. The structure of the FG nups is being taken into account by modelling them as diblock co-polymers. These results suggest that modulation of the inter-nup interactions by NTRs may lead to changes in polymer morphologies, and that this may have a significant role to play in nucleocytoplasmic transport.

The other possibility, namely modelling just a few nups fully and then attempt to infer NPC function from the physical data of such simulations, has yielded impressive results in determining possible structures as well as effective interactions amongst nups and NTRs. These simulations can reproduce the experimentally known locations of FG binding sites on the NTR surface, [43, 44, 45] as well as suggesting new binding locations. Interestingly such studies suggest that the viability of transport does not depend on the number of binding sites on the NTR surface but their density.

Atomistic modelling of the nups yields the most accurate representations of nup dynamics. Atomistic simulations of several nsp1 nucleoporins, grafted on a planar grid [33] show the formation of polymer-brush like structures. The radius of gyration of a protein within this brush is much larger than the corresponding radius of gyration of a single nsp1 protein. This provides evidence that interactions between the nups could be important for overall nup structure. When an NTR

was introduced to this structure [46] it was found to enter into the brush like structure, by binding to the FG repeat regions. In contrast an inert molecule was not found to enter the brush structure to the same extent. When such a simulation was repeated without FG repeats, the NTR did not enter the brush-like structure, emphasising the key role of NTR-FG dipeptide interactions in the diffusion of molecules through the brush-like structure.

Molecular dynamics simulations are an accurate way of determining structure and dynamics. However, the computational cost associated with MD makes it difficult to draw wide ranging conclusions about NPC transport, as assumptions involved in setting up the models can lead to divergent physical mechanisms of transport. It should be expected that as computers improve more of these assumptions could be relaxed, leading to less ambiguous conclusions. For now, however, MD does show quantitatively the key role that NTR-FG interactions have in the translocation of molecular cargoes. All MD simulations of transport have the common theme that inert cargoes will be rejected, though the precise nature of the barrier is still a matter of discussion.

1.5 Mean field theories

In addition to these methods one can also use mean field theories such as density functional theory (of which there is more detail in the next chapter) or Self-Consistent Field Theory to model the pore. It is difficult to capture full molecular detail using these methods, so one would work with the coarse-grained system already described in the molecular dynamics section. In density functional theory, instead of explicitly calculating all the intermolecular interactions, one represents the particles in the system as a number density function. Using well established physical arguments [47] one can then construct a free energy functional of the system that depends upon the number density function. This functional is then optimised so that the form of the number density function is such that the free energy is at a minimum. This is then the best approximation to the true density of the system. Self-Consistent Field Theory is similar, in which the system is described by one or more fields, and the field calculated by assuming that one configuration of the fields dominates in the properties of the system.

The advantage of these methods is generally lower computational cost, which can be reduced even further due to the fact that symmetry assumptions are easier to apply. The accuracy usually compares very well to the more accurate MD methods except under certain special conditions such

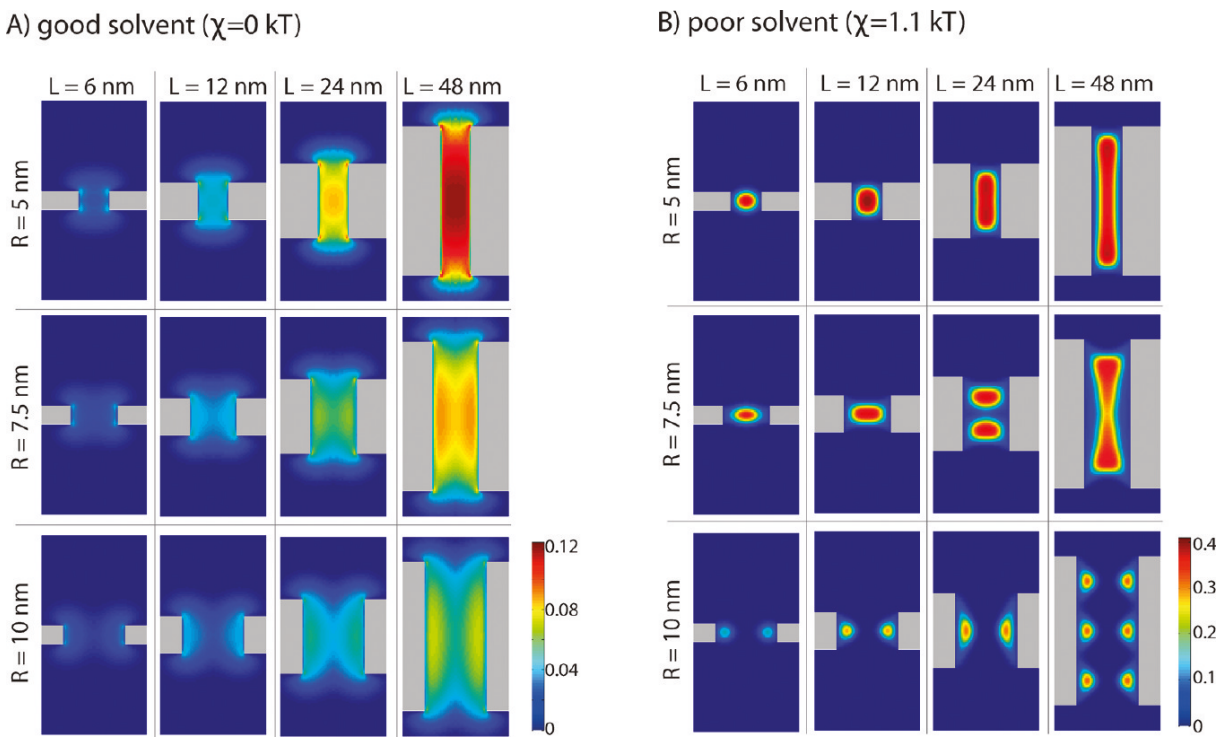

Figure 1.4: Occupied volume fraction (from 0 to 1), shown as coloured contours, for homopolymers end-grafted onto a nanopore, for varying pore radius (R) and axial length (L) in a good and poor solvent. These results show the extent of space filling of the polymers in a pore structure. As can be seen from the figures, there are several different ways that the polymers can be arranged.

as very strong interactions or when the system is near a phase transition. These methods will also give a free energy of the system, allowing phase maps of likely structures for different parameters to be plotted.

The morphologies of polymers bound within a cylindrical pore can take different forms. Several systematic studies have been performed [48] exploring the parameter space of such a system (see figure 1.4).

Common assumptions included in mean field calculations of this sort are that the density of the polymers is independent of the azimuthal angle (the angle as one goes around the circumference of the cylinder). Instead of using mean fields, Monte Carlo (MC) methods attempts to gain insight into the ensemble average of certain quantities, such as the density, by using random moves weighted by the energy change of the move[49]. When conducting MC simulations of the same system[50, 51], however, the assumption that the density is independent of azimuthal angle can be relaxed, showing a wealth of phases that are interesting, not only from a biological perspective,

but from a physical one.

These techniques allow us to see more deeply the role of confinement in the conformations of these disordered proteins. Ordinary polymers in bulk solutions are entropic springs, the entropy of stretched polymers goes down in proportion to the square of their extension. When such polymers are tethered on a planar surface, increasing the attraction between the polymer beads results in their drawing closer to their tethering points, as this is both energetically and entropically favourable. However, when polymers are tethered onto a closed surface, such as the inside of a cylinder, increasing the attraction can make it favourable for the polymers to extend away from their tethering points towards the centre, in a manner reminiscent of the pore filling hydrogel of the selective phase model. The entropic cost of extending towards the centre can be paid with the enthalpic gain arising from the fact that on average the polymer beads will be nearer to one another. This would not occur if the polymer attraction were not sufficiently high, in which case a familiar collapse to the tethering points would be observed. Such an effect would not be seen were the polymers anchored on a planar surface. One can also think of these same interactions in terms of solvent quality, i.e. hydrophobicity of the polymers. Decreasing the quality of the solvent, thus increasing the propensity of the hydrophobic polymers to draw together, would lead to formation of a "central plug" like structure, as long as the polymers are long enough to stretch that far.

In general one can find simple scaling relations for the radius of gyration of homopolymers tethered within a cylindrical geometry, in terms of parameters such as cylinder length, radius, grafting density and length of polymers. The polymers will exist in different scaling regimes depending on the parameters, where a regime refers to the exponent of the power law defining the average end to end extension of the polymer in terms of polymer parameters such as segment length and number of beads. Changing these parameters can lead to crossover between different regimes [52].

Polymers can also extend away from their tethering points due to excluded volume interactions between the polymer beads. This will generally force the polymers to swell due to crowding. When one explicitly includes the effect of a reservoir above and below the cylinder, the polymers can be shown to stretch out of the pore and into the reservoir. Not only does this decrease the effect of the repulsive interactions, but the conformational entropy is also increased as there are more states available for the polymers outside the pore. In general increasing the strength of attractive interactions will lead to more inhomogeneities of the FG nups within the pore.

Introducing other components into this system, such as free (untethered) polymers [53], can be viewed as a simple representation of cargoes interacting with FG nups. As the radius of the pore is decreased one can observe that a free chain penetrates more into the tethered polymer layer, even in the absence of interactions. It was seen that the extent of the overlap between free chains and tethered chains changes non-monotonically. Above a certain radius of the pore the overlap decreases rapidly. However, the significance of this to transport is hard to gauge.

In addition to the extended/collapsed dichotomy identified before, further multiplicity of phases can also be observed, with differing numbers of clumps at the wall. The number of clumps also depends on the parameters chosen. A systematic study of this phenomenon has yet to be performed.

Mean field theories can give quantitatively similar results to more accurate explicitly interacting models at a fraction of the overall computational cost. So long as one uses these theories within their realms of validity, the outputs of such theories give a useful way to determine structures. However, such theories will not be able to capture the molecular detail in the same way as molecular dynamics could. In addition, though dynamical mean field theories exist, application to the NPC has not been attempted. Most modelling of the NPC with mean field theories is restricted to stationary structures of polymer-coated pores, with results that can possibly inform the discussion of NPC function.

Monte Carlo methods have the same problem. As with the mean field theories, dynamical Monte Carlo schemes exist, but to attempt to discern the dynamics of the pore, one may as well use MD.

Despite this, one can attempt to simulate dynamics using mean field theories by calculating a potential of mean force for a cargo[54]. By placing a cargo particle *a priori* at a certain location along the central pore axis the free energy as a function of axial coordinate can be calculated. The free energy barrier to transport can then be estimated. The size of the free energy barrier facing a macromolecular cargo is related to the rate of transport of that cargo, with larger barriers generally meaning lower rates of transport. For example, it can be shown that the free energy barrier facing hydrophobic cargoes is generally smaller than hydrophilic cargoes. In addition, by including the effect of electrostatics, it has been suggested that the nups create a net-positive region inside the NPC, facilitating the transport of negatively charged cargoes. Such approaches have only recently begun to receive attention. Further research along these lines might lead to specific transport rates of various proteins found within the cell, for direct comparison to experiment.

The NPC has received relatively little attention from (bio-)physical modellers (though this is beginning to change), probably due to the complexity of modelling such a large biological system. So far, different modelling approaches strongly suggest that an appreciation of the collective behaviour of nucleoporins is necessary to describe NPC functionality. As may be expected for a structurally flexible and interacting many-particle system, the exact choice of structural and physical/chemical parameters is crucial. Given the present experimental uncertainty on these parameters, it is not surprising that modelling approaches have not yet converged to a unified view on structure and function of the disordered nucleoporins in the central conduit.

Given all the previously mentioned difficulties of modelling the NPC, we must come to a decision regarding the most fruitful way to model the NPC. While molecular dynamics studies of the NPC are possible, such an approach requires a lot of computational power. In addition to this, coarse-graining is necessary as an all-atom simulation would be prohibitively expensive. The number of interactions in the NPC is also a factor to consider before any modelling of the NPC is undertaken. As all the interactions in the NPC are not well known or calculated, a molecular dynamics approach would have to make assumptions about the way the coarse-grained constituents of the NPC are interacting. However, this means that a range of parameters would have to be explored, as even small changes in interaction parameters could lead to large changes in structure. Therefore, the computational cost of such an approach is very large.

We favour mean field theory approaches. Whilst less accurate than molecular dynamics simulations, mean field theories require less computational resources. This allows for a thorough exploration of the parameter space. For a certain set of parameters, mean field and explicit models can be compared to verify mean field approaches. The different methods we use to model the NPC are shown in depth in the coming chapters.

Chapter 2

Theoretical Methods

In this chapter we outline the various physical methods which can be applied to model the NPC. We discuss classical density functional theory, a powerful tool for determining equilibrium distributions of ensembles of classical particle. In addition, the basic theory behind polymer physics is described. We conclude with a description of the Monte Carlo method, which is a useful non-mean field way of taking thermodynamic averages.

2.1 Density functional theory

Density functional theory (DFT) is a well established and widely used theoretical tool in research in condensed matter. There are different implementations of DFT depending on which system is being modelled. Perhaps its most famous use is in the determination of electronic structure[55]. In addition to this electronic structure variant, a DFT dealing with the behaviour of classical gases has also been developed[47]. Both of these variants share similarities in their approach, where the quantity of interest, be it an energy or free energy, is represented as a functional of the particle density. A functional is a mapping of a function onto a number. Thus density functional theory provides a way of relating quantities of interest and the densities in the system. This thesis will be focusing on the classical variant, which is sometimes called classical density functional theory for clarity.

In statistical mechanics, physically meaningful macroscopic variables can be related to the *partition function*, Z, of the system. The canonical partition function for N particles can be

expressed as:

$$Z = \frac{1}{N!h^{3N}} \int \mathrm{d}\mathbf{r}^N \mathrm{d}\mathbf{p}^N \exp\left[-\beta(H(\mathbf{r}^N, \mathbf{p}^N))\right] \tag{2.1}$$

The quantities $\mathbf{r}^N$ and $\mathbf{p}^N$ define the position and momentum coordinates for the particles. The factor β is related to the temperature of the system by $\beta = 1/(k_b T)$ where k_b is the Boltzmann constant and T is the temperature. The factor h^{3N} is inserted to make the partition function dimensionless. The Hamiltonian of the system is $H(\mathbf{r}^N, \mathbf{p}^N)$, the Hamiltonian is often (though not always) the energy of the system given in terms of the position and momenta of the particles. If the particles in the system interact with each other with a potential energy U the Hamiltonian will be given by:

$$H(\mathbf{r}^N, \mathbf{p}^N) = \sum_{i=1}^{N} \frac{\mathbf{p}_i^2}{2m_i} + \frac{1}{2} \sum_{j=1}^{N} \sum_{k=1 \neq j}^{N} U(|\mathbf{r}_j - \mathbf{r}_k|) \tag{2.2}$$

where m_i is the mass of the ith particle. In the partition function, the division by the factor $N!$ is to account for the indistinguishability of each particle.

The partition function is a "sum over states", it sums over all the microstates in the system. Once we are able to calculate the partition function, all relevant thermodynamic quantities can calculated. For instance, the probability of finding any one state with microscopic parameters $\mathbf{r}^N$ and $\mathbf{p}^N$ is given by:

$$P(\mathbf{r}^N, \mathbf{p}^N) = \frac{1}{Z} \exp(-\beta H(\mathbf{r}^N, \mathbf{p}^N)). \tag{2.3}$$

Unfortunately, for all but the simplest form of the Hamiltonian, calculation of the partition function is impossible. In order to make progress, different methods must be used.

A useful thermodynamic potential is the Helmholtz free energy F. At equilibrium, the free energy of a system will be at a minimum. It is given in terms of the partition function by:

$$F = -\ln(Z)/\beta \tag{2.4}$$

or equivalently:

$$F = \langle H \rangle - TS \tag{2.5}$$

where T is the temperature and S is the entropy and where an angular bracket denotes a thermodynamic average:

$$\langle H \rangle = \frac{1}{Z} \int \mathrm{d}\mathbf{r}^N \mathrm{d}\mathbf{p}^N H(\mathbf{r}^N, \mathbf{p}^N) \exp\left[-\beta(H(\mathbf{r}^N, \mathbf{p}^N))\right] \tag{2.6}$$

Density functional theory states as its main premise that the free energy of a system can be represented as a functional of the particle density $\rho(\mathbf{r})$. This theorem has been generally proved [47].

In order to construct free energy functionals, we use the Bogoliubov inequality[56]. This inequality states that when the free energy of a system with a particular Hamiltonian is estimated using the distribution of states from a different system, the free energy will be greater than or equal to the true free energy of the system.

If the system we wish to describe has the Hamiltonian H, we first imagine splitting the Hamiltonian into two different contributions $H = H_0 + H_1$ where H_0 is the Hamiltonian of a simpler system that can be solved. The full partition function of the system is given by:

$$Z = \frac{1}{N!h^{3N}} \int \mathrm{d}\mathbf{r}^N \mathrm{d}\mathbf{p}^N \exp\left[-\beta(H_0(\mathbf{r}^N, \mathbf{p}^N) + H_1(\mathbf{r}^N, \mathbf{p}^N))\right] \tag{2.7}$$

If this partition function is divided by Z_0, the partition function of a system with Hamiltonian H_0, and using equation (2.3) we obtain:

$$\frac{Z}{Z_0} = \int \mathrm{d}\mathbf{r}^N \mathrm{d}\mathbf{p}^N P_0(\mathbf{r}^N, \mathbf{p}^N) \exp\left[-\beta H_1(\mathbf{r}^N, \mathbf{p}^N)\right] \tag{2.8}$$

The right hand side of this equation is equal to $\langle \exp\left[-\beta H_1(\mathbf{r}^N, \mathbf{p}^N)\right]\rangle$, in other words, the average of $\exp\left[-\beta H_1(\mathbf{r}^N, \mathbf{p}^N)\right]$ in the distribution of states given by Z_0. A mathematical property of the exponential function is that $\langle \exp x\rangle \geq \exp\langle x\rangle$. Therefore the following is obtained:

$$\frac{Z}{Z_0} \geq \exp(-\beta\langle H_1\rangle_0) \tag{2.9}$$

where $\langle H_1\rangle_0 = \int \mathrm{d}\mathbf{r}^N \mathrm{d}\mathbf{p}^N P_0(\mathbf{r}^N, \mathbf{p}^N) H_1$. If logarithms of equation (2.9) are taken then:

$$F \leq F_0 + \langle H_1\rangle_0 \tag{2.10}$$

where equation (2.4) has been used. Using equation (2.5) also gives us that $F_0 = \langle H_0\rangle_0 - TS_0$ such that the Bogoliubov inequality is arrived at:

$$F \leq \langle H\rangle_0 - TS_0 \tag{2.11}$$

This inequality states that if the free energy of the system is evaluated using the distribution of states of the simpler reference system, the resulting free energy that is calculated will be an upper bound of the true free energy of the system. A smaller difference between the true and the calculated free energy means that H_0 is a more reasonable representation of the true system. This leads naturally to a variational interpretation, if there is an adjustable parameter included within the Hamiltonian H_0, choosing this parameter such that the resulting free energy is minimised will correspond to the best approximation to the full Hamiltonian H. This should be distinguished from

the dynamic nature of thermodynamic systems to move towards the state of minimum free energy; selecting the conformation with the lowest free energy is merely selecting a set of parameters which best represent the true system.

We can use this important result to derive a general functional for a system with complex many body interactions. We do this by introducing a mean field $W(r)$. The Hamiltonian of a general system $H(\mathbf{r}^N, \mathbf{p}^N) = \sum_{i=1}^{N} \frac{\mathbf{p}_i^2}{2m_i} + \frac{1}{2}\sum_{j=1}^{N}\sum_{k=1\neq j}^{N} \phi(|\mathbf{r}_j - \mathbf{r}_k|)$ is split in the following way:

$$H_0 = \sum_{i=1}^{N} \frac{\mathbf{p}_i^2}{2m_i} + \sum_{i=1}^{N} W(\mathbf{r}_i) \tag{2.12}$$

$$H_1 = \frac{1}{2}\sum_{j=1}^{N}\sum_{k\neq j}^{N} \phi(\mathbf{r_k} - \mathbf{r_j}) - \sum_{i=1}^{N} W(\mathbf{r}_i) \tag{2.13}$$

one can envisage making more subtle Hamiltonian splitting mechanisms, such as splitting the pair potential. The free energy of this system is given by:

$$F = -k_b T \ln\left(Z_0\right) - \left\langle \sum_{i=1}^{N} W(\mathbf{r_i}) \right\rangle_0 + \left\langle \frac{1}{2}\sum_{j=1}^{N}\sum_{k\neq j}^{N} \phi(\mathbf{r_k} - \mathbf{r_j}) \right\rangle_0 \tag{2.14}$$

where Z_0 is the partition function of the reference system. This is the most general form of a free energy functional. Provided there is a way under Hamiltonian H_0 to calculate the density and the partition function, we can calculate an approximate upper bound to the free energy. For instance, in this case the reference system is an ideal gas under an external potential, which is a solvable system. If we search in the space of mean fields $W(r)$ we can find the one that minimises this free energy functional, and is therefore the best approximation to the multi-body interactions in the system.

In most realisations of DFT, the mean field is not immediately apparent. For instance, when the reference system is an ideal gas under external potential, as above, then the functional takes the following form [57]:

$$\begin{aligned} F = {} & k_b T \int \rho^{(1)}(\mathbf{r}) \left(\ln(\rho^{(1)}(\mathbf{r})\lambda^3) - 1\right) \mathrm{d}\mathbf{r} + \int \rho^{(1)}(\mathbf{r}) W(\mathbf{r}) \mathrm{d}\mathbf{r} - \int \rho^{(1)}(\mathbf{r}) W(\mathbf{r})\, \mathrm{d}\mathbf{r} \\ & + \frac{1}{2} \iint \rho^{(2)}(\mathbf{r}, \mathbf{q}) U(\mathbf{r} - \mathbf{q}) \mathrm{d}\mathbf{r}\, \mathrm{d}\mathbf{q} \end{aligned} \tag{2.15}$$

One can see that all the terms containing explicit reference to $W(r)$ cancel away, however one must be aware that the mean field underlies the functional.

2.2 Polymer theory

As mentioned previously, the nups constituting the NPC are intrinsically disordered. This allows the statistical mechanics of polymers to be applied to describe nup behaviour. The goal of this section is to have an expression for the partition function of a polymer. Restating the definition of the partition function from the previous section:

$$Z = \frac{1}{\lambda^{3N} N!} \int \mathrm{d}\mathbf{r}^N \exp\left[-\beta U(\mathbf{r}^N)\right] \tag{2.16}$$

where the integration over the momentum coordinates has been performed, leaving the thermal de Broglie wave length λ, such that the only element of the Hamiltonian that remains is the intermolecular interaction U.

The form of intermolecular interactions in simple polymer models accounts for only the intermolecular interactions between neighbouring monomers along the backbone of the polymer. There are several different choices for the form of this interaction. A popular and analytically straightforward model is the Gaussian chain model where the polymers are subject to a harmonic force from their neighbours, for example for neighbouring monomers at r_1 and r_2 the potential between them is $U(\mathbf{r}_1, \mathbf{r}_2) = \frac{3k_bT}{2b^2}(\mathbf{r}_1 - \mathbf{r}_2)^2$, where b is the root mean square bond length between the monomers.

If we consider a polymer of N monomers, we can write the partition function as follows:

$$Z_0 = \frac{1}{\lambda^{3N} N!} \prod_{j=0}^{N} \int \mathrm{d}\mathbf{r}_j \exp\left(-\frac{3}{2b^2} \sum_{i=1}^{N} |\mathbf{r}_{i-1} - \mathbf{r}_i|^2\right) \tag{2.17}$$

A common extension to this model for analytical calculations is the continuous Gaussian chain model. Instead of discrete monomeric elements, the polymer chain is represented as a space curve $r(s)$ where the s parametrises the position along the polymer. In this case the potential in the exponential of equation 2.17 is changed to the continuum limit:

$$Z_0 = \frac{1}{\lambda^{3N} N!} \int \mathrm{D}\mathbf{r} \exp\left[-\frac{3k_bT}{2b^2} \int_0^N \mathrm{d}s \left|\frac{\mathrm{d}\mathbf{r}(s)}{\mathrm{d}s}\right|^2\right] \tag{2.18}$$

This equation is now a path integral, a integration over all the different possible paths that the polymer can take. This is represented by the change of the integral measure from d to D. Somewhat ironically, the next step is to discretise the path integral once again:

$$Z_0 = \lim_{n\to\infty} \frac{1}{\lambda^{3N} N!} \frac{1}{V} \int \mathrm{d}\mathbf{r}_0 \ldots \int \mathrm{d}\mathbf{r}_n \left(\frac{3}{2\pi \Delta s b^2}\right)^{3n/2} \exp\left[-\frac{3}{2\Delta s b^2} \sum_{k=1}^{n} (\mathbf{r}_k - \mathbf{r}_{k-1})^2\right] \tag{2.19}$$

where $\Delta s = n/N$. A very useful way of representing polymer partition functions such as this is through the use of propagators. If we define the Gaussian function:

$$\Phi_n(x) \equiv \left(\frac{3}{2\pi\Delta s b^2}\right) \exp\left[-\frac{3N}{2\Delta s b^2}x^2\right] \tag{2.20}$$

we can then rewrite the partition function as follows:

$$Z_0 = \frac{1}{\lambda^{3N} N!}\frac{1}{V}\int \mathrm{d}\mathbf{r}_0 \ldots \int \mathrm{d}\mathbf{r}_n \prod_{i=1}^{n} \Phi(\mathbf{r}_i - \mathbf{r}_{i-1}) \tag{2.21}$$

Now if we write the definition of a propagator q as follows:

$$q(\mathbf{r}, s + \Delta s) \equiv \int \mathrm{d}\mathbf{r}' \Phi(\mathbf{r} - \mathbf{r}') q(\mathbf{r}', s) \tag{2.22}$$

The propagator depends on both spatial position $\mathbf{r}$ and contour position along the polymer s. It can be interpreted as the probability for the polymer contour position at s to be at a position $\mathbf{r}$ in space. From this definition equation 2.22 it can be seen that the full partition function is given by:

$$Z_0 = \frac{1}{\lambda^{3N} N!}\frac{1}{V}\int \mathrm{d}\mathbf{r} q(\mathbf{r}, N) \tag{2.23}$$

this equation can be understand intuitively by realising that this partition function is just the sum of probabilities over all possible endpoints of the polymer. By rewriting equation 2.22 in terms of $\Delta\mathbf{r} = \mathbf{r} - \mathbf{r}'$ and Taylor expanding we can write a partial differential equation for q.

$$q(\mathbf{r}, s + \Delta s) = \int \mathrm{d}(\Delta\mathbf{r})\Phi(\Delta\mathbf{r}) q(\mathbf{r} - \Delta\mathbf{r}, s) \quad \text{Taylor expanding:} \tag{2.24}$$

$$q(\mathbf{r}, s) + \Delta s \frac{\partial q(\mathbf{r}, s)}{\partial s} = q(\mathbf{r}, s)\int \mathrm{d}(\Delta\mathbf{r})\Phi(\Delta\mathbf{r}) - \nabla q(\mathbf{r}, s).\int \mathrm{d}(\Delta\mathbf{r})\Delta\mathbf{r}\,\Phi(\Delta\mathbf{r}) \tag{2.25}$$

$$+ \frac{1}{2}\sum_{ij}\frac{\partial^2 q(\mathbf{r}, s)}{\partial r_i \partial r_j}\int \mathrm{d}(\Delta\mathbf{r})\Phi(\Delta\mathbf{r})\Delta r_i \Delta r_j$$

We can use the following identities to simplify this equation:

$$\int \mathrm{d}(\Delta\mathbf{r})\Phi(\Delta\mathbf{r}) = 1 \tag{2.26}$$

$$\int \mathrm{d}(\Delta\mathbf{r})\Delta\mathbf{r}\,\Phi(\Delta\mathbf{r}) = 0 \tag{2.27}$$

$$\int \mathrm{d}(\Delta\mathbf{r})\Phi(\Delta\mathbf{r})\Delta r_i \Delta r_j = \frac{b^2\Delta s}{3}\delta_{ij} \tag{2.28}$$

therefore in the limit $\lim_{s\to 0}$ we obtain the following partial differential equation for the propagator q:

$$\frac{\partial q(\mathbf{r}, s)}{\partial s} = \frac{b^2}{6}\nabla^2 q(\mathbf{r}, s) \tag{2.29}$$

solving this equation under appropriate boundary and initial conditions gives the chain propagator of the polymer, allowing us to calculate the partition function of the polymer.

The extension of this includes the effect of some external potential $W(\mathbf{r})$ acting on the polymer beads. In this case, the potential included in the partition function is given by:

$$U(\mathbf{r}^N) = \sum_{i=1}^{N} h(|\mathbf{r}_i - \mathbf{r}_{i-1}|) + k_b T \sum_{i=0}^{N} W(\mathbf{r}_i) \tag{2.30}$$

where h is the neighbouring monomer interaction. We can rewrite this expression using the microscopic density of beads $\rho(\mathbf{r})$

$$\rho(\mathbf{r}) = \sum_{i=0}^{N} \delta(\mathbf{r} - \mathbf{r}_i) \tag{2.31}$$

$$\sum_{i=0}^{N} W(\mathbf{r}_i) = \int \mathrm{d}\mathbf{r} W(\mathbf{r})\rho(\mathbf{r}) \tag{2.32}$$

such that the continuous Gaussian chain partition function has the following form, when under the influence of an external potential:

$$Z = \frac{1}{\lambda^{3N} N!} \int \mathrm{D}\mathbf{r} \exp\left[-\frac{3k_b T}{2b^2} \int_0^N \mathrm{d}s \left| \frac{\mathrm{d}\mathbf{r}(s)}{\mathrm{d}s} \right|^2 - \int \mathrm{d}\mathbf{r}\, W(\mathbf{r})\rho(\mathbf{r}) \right] \tag{2.33}$$

using similar methods as that for the chain without an external potential described previously, we can write the propagator for a chain under an external potential:

$$q(\mathbf{r}, s + \Delta s; [W]) \equiv \exp\left[-\Delta s\, W(\mathbf{r})\right] \int \mathrm{d}\mathbf{r}' \Phi(\mathbf{r} - \mathbf{r}') q(\mathbf{r}', s) \tag{2.34}$$

where the partition function is given in the same way as before:

$$Z = \frac{1}{V} \int \mathrm{d}\mathbf{r}\, q(\mathbf{r}, N; [W]) \tag{2.35}$$

and the partial differential equation that q satisfies is given by:

$$\frac{\partial q(\mathbf{r}, s)}{\partial s} = \frac{b^2}{6} \nabla^2 q(\mathbf{r}, s) - W(\mathbf{r}) q(\mathbf{r}, s) \tag{2.36}$$

using appropriate boundary conditions and calculating the partition function allows the partition function to be determined.

Returning now to the definition of the partition function:

$$Z[W] = \frac{1}{\lambda^{3N} N!} \int \mathrm{D}\mathbf{r} \exp\left[-\frac{3k_b T}{2b^2} \int_0^N \mathrm{d}s \left| \frac{\mathrm{d}\mathbf{r}(s)}{\mathrm{d}s} \right|^2 - \int \mathrm{d}\mathbf{r}\, W(\mathbf{r})\rho(\mathbf{r}) \right] \tag{2.37}$$

We have made the functional dependence of Z upon W by explicitly including it within the square brackets. As in the ordinary calculus of functions, there exists a derivative of functional. By analogy with ordinary differentiation, functional differentiation measures the change of a general functional G as the function ϕ of which G is a functional of changes. The functional derivative is defined by:

$$\frac{\delta G[\phi(x)]}{\delta \phi(y)} = \lim_{\varepsilon \to 0} \frac{G[\varphi(x) + \varepsilon \delta(x-y)] - F[\varphi(x)]}{\varepsilon} \tag{2.38}$$

It can be shown that:

$$\rho(\mathbf{y}) = -\frac{\delta \ln Z[W]}{\delta W(\mathbf{y})} \tag{2.39}$$

We show this by explicitly performing the functional differentiation of the partition function $Z[W]$. We introduce the notation $U_0[\mathbf{r}]$ to represent the forces along the polymer backbone which do not depend explicitly on the mean field W.

$$\begin{aligned}
&\frac{\delta Z[W]}{\delta W(\mathbf{y})} = \\
&\lim_{\epsilon \to 0} \frac{1}{\epsilon} \left[\int \mathrm{D}\mathbf{r} \exp\left(-U_0[\mathbf{r}] - \int \hat{\rho}(\mathbf{r}')(W(\mathbf{r}') + \epsilon \delta(\mathbf{r}' - \mathbf{y}))\mathrm{d}\mathbf{r}' \right) \right. \\
&\left. - \int \mathrm{D}\mathbf{r} \exp\left(-U_0[\mathbf{r}] - \int \hat{\rho}(\mathbf{r}') W(\mathbf{r}')\, \mathrm{d}\mathbf{r}' \right) \right] \\
&= - \int \mathrm{D}\mathbf{r} \hat{\rho}(\mathbf{y}) \exp\left(-U_0[\mathbf{r}] - \int \hat{\rho}(\mathbf{r}') W(\mathbf{r}')\, \mathrm{d}\mathbf{r}' \right),
\end{aligned} \tag{2.40}$$

such that we can define $\rho(\mathbf{y}) = \langle \hat{\rho}(\mathbf{y}) \rangle$

$$\begin{aligned}
\rho(\mathbf{y}) &= \frac{1}{Z} \int D\mathbf{r} \hat{\rho}(\mathbf{y}) \exp\left(-U_0[\mathbf{r}] - \int \hat{\rho}(\mathbf{r}') W(\mathbf{r}')\, \mathrm{d}\mathbf{r}' \right) \\
&= -\frac{1}{Z[W]} \frac{\delta Z[W]}{\delta W(\mathbf{y})} = -\frac{\delta \ln Z[W]}{\delta W(\mathbf{y})},
\end{aligned} \tag{2.41}$$

The use of this relation now means that an expression for the segment density in terms of the chain propagator may be written:

$$\rho(r; [W]) = \frac{1}{V Z[W]} \int_0^N q(\mathbf{r}, N-s; [W]) q(\mathbf{r}, s; [W]) \mathrm{d}s \tag{2.42}$$

In order to determine the density profile of a polymer tethered at a point, such as the proteins within the nuclear pore complex, equation (2.36) is to be solved with initial condition $\delta(\mathbf{r} - \mathbf{r}')$ where r' specifies the tethering point. The density will then be given by:

$$\frac{1}{Q(\mathbf{r}'; [W])} \int_0^N G(\mathbf{r}', \mathbf{r}, N-s; [W]) q(\mathbf{r}, s; [W]) \mathrm{d}s \tag{2.43}$$

where the new notation $G(\mathbf{r}', \mathbf{r}, N-s; [W])$ has been used to specify the solution of the equation:

$$\frac{\partial G(\mathbf{r}', \mathbf{r}, s; [W])}{\partial s} = \frac{b^2}{6}\nabla^2 G(\mathbf{r}', \mathbf{r}, s; [W]) - W(r)G(\mathbf{r}', \mathbf{r}, s; [W]) \tag{2.44}$$

with the delta function initial condition. and $Q(\mathbf{r}'; [W])$ is the partition function of a tethered polymer chain $\int G(\mathbf{r}', \mathbf{r}, N; [W])\mathrm{d}r$. The entire density for N segments can be rewritten in terms of this G as:

$$\rho(r) = \frac{\iint G(\mathbf{r}', \mathbf{r}, N-s; [W])G(\mathbf{r}, \mathbf{q}, s; [W])\,\mathrm{d}\mathbf{q}\,\mathrm{d}s}{\int G(\mathbf{r}', \mathbf{q}, N; [W])\,\mathrm{d}\mathbf{q}} \tag{2.45}$$

G is sometimes known as the "Green's Function" of the polymer, the equations (2.43) and (2.45) give equivalent solutions, however the former is much less computationally expensive to determine. The latter has its uses in analytical calculations. $G(r', r, N)$ is also the statistical weight for a polymer of N beads starting at $\mathbf{r}'$ to be found at $\mathbf{r}$.

2.3 Monte Carlo

Another way of modelling large ensembles of interacting particles is through Monte Carlo (MC) techniques. MC involves treating all the particles individually, without making assumptions about mean fields. Monte Carlo techniques seek to take a sample of the true statistics of the system. Though MC techniques can be applied to many different situations, we will here expand upon the most pertinent for statistical physics, the "Metropolis" Method.

The metropolis method as used in statistical physics takes as its start point an initial state, from this initial state, subsequent states are generated based on a probability given by the energy difference between the initial state and the next state. The main constraint upon Monte Carlo simulations are that they must obey the "detailed balance" condition.

$$P_n(t)W_{n\to m} = P_m(t)W_{m\to n} \tag{2.46}$$

Here the time t is not the same as real time, but instead refers to the "time of progress" along the Monte Carlo simulation. Where $P_n(t)$ is the probability that the state is in state n at "time" t and $W_{n\to m}$ is the transition rate for $n \to m$. This condition essentially specifies that the probability of observing a state does not change with simulation time as we go to long simulation times (i.e. as we approach equilibrium).

As mentioned in previous sections, the probability of observing a particular state of an ensemble is given by:

$$P_n(t) = \frac{1}{Z} \exp\left(-\beta E_n\right) \tag{2.47}$$

where E_n is the total energy of state n. The denominator is unknown, but if we generate a Markov chain, in the sense that we generate every new configuration from a slight change in the previous one, the relative probability is a ratio between the two different states. Such that the only factor that affects whether the new system is adopted is the energy difference between the two states m and n, $\Delta E = E_n - E_m$.

The generalised algorithm for Monte Carlo of a fluid is then as follows:

1. Generate a ensemble with the particles at random positions.
2. Randomly select a particle in the ensemble.
3. Move the particle to a new position.
4. Calculate the energy change between the states before and after moving.
5. Compute the Boltzmann factor of the particle move $\exp(-\beta\Delta E)$ and generate a random number R_n in the range $[0, 1]$.
6. If $\Delta E < 0$, save the new state. If $\Delta E > 0$, then check whether the Boltzmann factor is greater than the random number R_n. If this is true save the new state, if not then discard the new state.
7. Go back to step 2.

This process is repeated for how ever long it takes to reach convergence. Once the system has been converged, statistical averages of thermodynamic quantities can be taken. However, in order to get accurate results it is imperative to wait until the system has equilibrated.

In this chapter, we reviewed some of the fundamentals behind the theory which we will use to develop a model of the NPC. We expanded on several key parts of density functional theory, polymer theory and Monte Carlo. In the next chapter, we apply the methods discussed in this chapter to build a simplified model of the NPC.

Chapter 3

Modelling of Polymer Coated Nanopores

This chapter develops a simple physical model of the NPC. By using simplifying assumptions, a minimal model of the NPC is created. We then use our minimal model to explore possible scenarios that could be of relevance to the NPC.

3.1 Models of nucleoporin behaviour

Using the methods developed in the previous chapter, we can develop a simplified model of the Nuclear Pore Complex, focussing on the conformations of the natively unfolded proteins in the central channel.

Nucleoporins in the NPC channel have been shown to separate into two distinct categories: those that form short globular conformations, and longer polymers that tend to be able to extend further away from their tethering point at the NPC rim [25]. As cylindrical confinement will mostly affect those nucleoporins with contour length much greater than the pore radius, we focus on this latter category as we construct an initial model for the NPC. We choose polymers with 100 nm contour length, end-grafted on a ring around the inner wall of a long cylinder with a radius $R = 25$ nm (figure 3).

We model the polymers as freely jointed chains of beads of diameter $d = 1$ nm, with a segment length $b = 1$ nm. This implies a persistence length of 0.5 nm, in agreement with single-molecule pulling experiments on nucleoporin cNup153 [58], where the persistence length is the length over which the average angular correlations along the chain decays by $1/e$. Excluded-volume effects are modelled as a hard-sphere repulsion between the beads. They are supplemented by longer-ranged

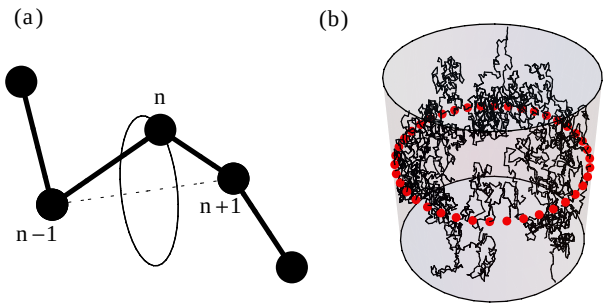

Figure 3.1: (a) Illustration of the Monte Carlo move, where bead n is constrained to lie on a circle such that the length of the bonds to beads $n-1$ and $n+1$ is unchanged. In our Monte Carlo simulations, polymer bead n would be chosen to lie anywhere on the circle. (b) Snapshot of a Monte Carlo simulation with 40 non-interacting polymers of contour length 100 nm, bead diameter $d = 1$ nm and bond length $b = 1$ nm, end-grafted to the thick dots in a cylindrical pore of 25 nm radius.

attractive interactions between the polymers, consistent with those that appear to operate in the NPC [59, 60, 61, 1]. The combined bead-bead pair potential therefore takes the form

$$\phi(\mathbf{r}) = \begin{cases} \infty & |\mathbf{r}| < d \\ -\epsilon \exp[-(|\mathbf{r}| - d)/\lambda] & |\mathbf{r}| \geq d\,, \end{cases} \tag{3.1}$$

where $\mathbf{r}$ is the vector connecting the centres of the beads, and λ and ϵ are range and strength parameters, respectively. A variety of interaction mechanisms might be represented by an appropriate choice of d, λ and ϵ in equation (3.1), including, for example, the hydrophobic interaction that is thought to play a significant role in these systems [37].

As a first approach to determine typical polymer configurations, we study the system by Monte Carlo (MC) simulations. We employ the Metropolis algorithm described in the previous chapter. The only addition we make to this algorithm is the addition of a constraint in the movement of single beads such that they attempt moves on a circular path defined by the constant distance b to their nearest neighbours, whilst remaining restricted to the inner volume of the cylinder as illustrated in figure 3. The first bead for each polymer, located on the cylinder inner surface, is fixed in position, whilst the last bead is free to move on the surface of the sphere of radius b centred on the penultimate bead. The restriction of constant segment length simplifies the description of each MC move, but can slow down the exploration of configuration space. Nevertheless, all polymer conformations are accessible from one another. We perform simulations of 250000 attempted

moves per bead. Relaxation to equilibrium is confirmed by noting convergence of the system energy, therefore we use the second half of each simulation to generate mean bead profiles. The simulations indicate an interesting range of behaviour, as can be seen in figure 3.2 for 40 polymers, each of length 100 beads, tethered uniformly around a ring. Different dominant configurations may be observed depending on the parameters chosen, though they can be roughly divided into two categories: conformations in which the density is peaked in the centre, and those in which it is peaked closer to the wall. Sometimes profiles from both categories emerge even for the same parameter choice, depending on the starting configuration. This suggests that there exist thermodynamically stable and metastable states for a particular parameter set.

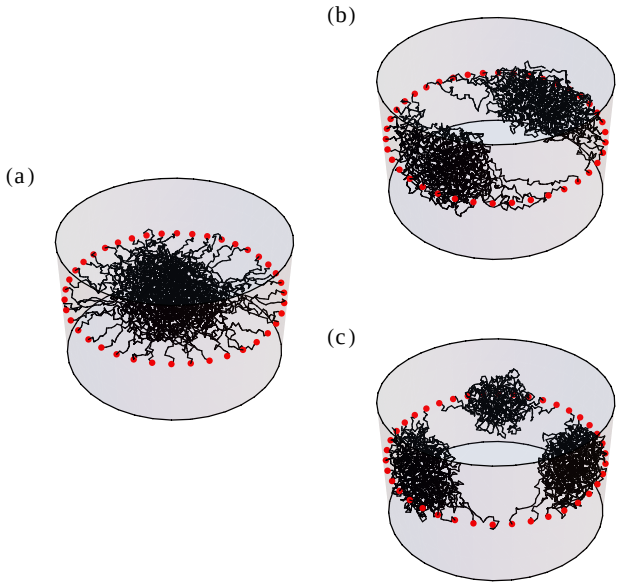

Figure 3.2: Snapshots taken from converged Monte Carlo simulations as in figure 3, showing different results for polymers that are subject to the same excluded volume and attractive interactions, as defined by equation 5.22 with $\epsilon = 0.1\, k_B T$ and $\lambda = 1.0$ nm. (a): Condensation in the centre. (b) and (c): Different numbers of clumps can be found when the polymers condense closer to the wall.

In order to categorise these phases more fully, and in particular to investigate the relative stability of wall and central configurations, we will develop the variational mean field density functional theory of a many-polymer systems using the ideas from the previous chapter. Density functional theory provides a natural framework for evaluating the free energy of large numbers of interacting particles [47], though certain modifications are necessary for it to be suitable as a

model of a system of polymers. It shares many of the features of a self-consistent statistical field theory of polymers [62], and has the capacity to include finite-range interactions, as expressed in the pair-potential $\phi(\mathbf{r})$. The polymer entropy is estimated by solving an equivalent Brownian motion problem, in contrast to other approaches that are also based on the minimization of a free energy functional but estimate the entropy by numerically generating a large set of sample configurations [48]. Our model can be implemented using an efficient numerical algorithm that runs on a standard desktop PC. It can be used to explore the equilibrium behaviour of the system. Dynamical versions of DFT have been developed to include relaxational phenomena [63, 64], and the model we develop has the potential to be extended in this direction.

We focus our interest on the statistical properties of a Hamiltonian H_0 for a polymer of N point-like beads at positions $\{\mathbf{r}_i\}$ in a dimensionless external potential W, given by $H_0 = U_0(\{\mathbf{r}_i\}) + k_BT\sum_{i=1}^{N} W(\mathbf{r}_i)$, where $U_0(\{\mathbf{r}_i\}) = \sum_i h(\mathbf{r}_{i+1}, \mathbf{r}_i)$ is a function that imposes the constraints on bond length, in our case the form of the interaction that we use is that of the Gaussian chain. The bead at $\mathbf{r}_1$ is constrained with respect to the tether point at $\mathbf{r}_0$. As discussed previously, the partition function of the system is (see equation 2.40)

$$Z_0 = \int \prod_{j=1}^{N} \mathrm{d}\mathbf{r}_j \exp\left[-U_0/k_BT - \sum_{i=1}^{N} W(\mathbf{r}_i)\right]. \tag{3.2}$$

The configuration-dependent bead density over continuous spatial position $\mathbf{r}$ is defined as $\hat{\rho}(\mathbf{r}, \{\mathbf{r}_k\}) = \sum_{i=1}^{N} \delta(\mathbf{r} - \mathbf{r}_i)$, which allows us to write Z_0 as

$$Z_0[W] = \int \mathrm{D}\mathbf{r} \exp\left(-U_0[\mathbf{r}]/k_BT - \int \hat{\rho}(\mathbf{r}) W(\mathbf{r}) \mathrm{d}\mathbf{r}\right), \tag{3.3}$$

where $D\mathbf{r}$ represents the integration over bead positions and we compress the notation of $\hat{\rho}$ for clarity.

ρ is a functional of the external potential W. The explicit functional dependence is given by (see equation 2.45):

$$\rho(\mathbf{r}) = \frac{\int_0^N \mathrm{d}s \int \mathrm{d}\mathbf{r}' G(\mathbf{r}_0, \mathbf{r}, N-s; [W]) G(\mathbf{r}, \mathbf{r}', s; [W])}{\int \mathrm{d}\mathbf{r}' G(\mathbf{r}_0, \mathbf{r}', N; [W])}. \tag{3.4}$$

where G_N is the *Green's function* of the polymer (as defined before) and is given as the solution to the equation (see equation 2.44):

$$\frac{\partial G(\mathbf{r}_0, \mathbf{r}, s; [W])}{\partial s} = \left(\frac{b^2}{6}\nabla^2 - W(\mathbf{r})\right) G(\mathbf{r}_0, \mathbf{r}, s; [W]) \tag{3.5}$$

The only adaptation we have to make to this equation in order to model Gaussian Polymers tethered within a cylinder is the addition of initial and boundary conditions. The initial condition is $G = \delta(\mathbf{r} - \mathbf{r}_0)$ at $s = 0$, and the boundary conditions are $G = 0$ at the cylinder wall and zero radial gradient at the centre.

Now we discuss a self-interacting polymer described by the Hamiltonian

$$H = U + \frac{1}{2}\sum_{j=1}^{N}\sum_{i\neq j}^{N}\phi(\mathbf{r}_i - \mathbf{r}_j)\,, \tag{3.6}$$

incorporating a potential ϕ acting between all bead pairs. We write $H = H_0 + H_1$ with

$$H_1 = \frac{1}{2}\sum_{j=1}^{N}\sum_{i\neq j}^{N}\phi(\mathbf{r}_i - \mathbf{r}_j) - k_BT\sum_{i=1}^{N}W(\mathbf{r}_i)\,, \tag{3.7}$$

and employ the Bogoliubov inequality $F \leq F_0 + \langle H_1\rangle$. As before, the brackets denote an average over the ensemble associated with H_0, and where F is the free energy of the system described by Hamiltonian H, and $F_0 = -\ln Z_0$ is the free energy of the reference system described by H_0, in units of k_BT. As seen in the previous chapter, the general form of the free energy for a system is given by:

$$F = -k_bT\ln(Z_0) - \left\langle\sum_{i=1}^{N}W(\mathbf{r_i})\right\rangle_0 + \left\langle\frac{1}{2}\sum_{j=1}^{N}\sum_{k\neq j}^{N}\phi(\mathbf{r_k} - \mathbf{r_j})\right\rangle_0 \tag{3.8}$$

Now, we can apply the general results taken from polymer theory to derive a functional description of polymers. In particular, the partition function for a polymer tethered at point $\mathbf{r}_0$ under an external potential W is given by:

$$Z_0 = \int G(\mathbf{r}_0, \mathbf{r}, N; [W]) \tag{3.9}$$

Proceeding to the next term:

$$\begin{aligned}\left\langle\sum_{i=1}^{N}W(\mathbf{r}_i)\right\rangle &= \frac{1}{Z_0}\int[\mathrm{d}\mathbf{r}_i]\int\hat{\rho}(\mathbf{y})W(\mathbf{y})\,\mathrm{d}\mathbf{y}\exp\left(-\frac{U_0}{k_BT} - \int\hat{\rho}(\mathbf{r})W(\mathbf{r})\,\mathrm{d}\mathbf{r}\right)\\ &= \int\rho(\mathbf{y})W(\mathbf{y})\,\mathrm{d}\mathbf{y}.\end{aligned} \tag{3.10}$$

In a similar fashion the mean of the pairwise terms is

$$\begin{aligned}\left\langle\sum_{j=1}^{N}\sum_{i\neq j}^{N}\phi(\mathbf{r}_i - \mathbf{r}_j)\right\rangle &= \frac{1}{Z_0}\int[\mathrm{d}\mathbf{r}_i]\int\hat{\rho}_2(\mathbf{x},\mathbf{y},\{\mathbf{r}_k\})\phi(\mathbf{x}-\mathbf{y})\mathrm{d}\mathbf{x}\mathrm{d}\mathbf{y}\times\exp\left(-\frac{U_0}{k_BT} - \int\hat{\rho}(\mathbf{r})W(\mathbf{r})\mathrm{d}\mathbf{r}\right)\\ &= \int\rho_2(\mathbf{x},\mathbf{y})\phi(\mathbf{x}-\mathbf{y})\mathrm{d}\mathbf{x}\mathrm{d}\mathbf{y},\end{aligned} \tag{3.11}$$

where $\hat{\rho}_2(\mathbf{x},\mathbf{y},\{\mathbf{r}_k\}) = \sum_{i\neq j}\delta(\mathbf{x}-\mathbf{r}_i)\delta(\mathbf{y}-\mathbf{r}_j)$ is the two-point configuration-dependent bead distribution and $\rho_2(\mathbf{x},\mathbf{y}) = \langle\hat{\rho}_2(\mathbf{x},\mathbf{y},\{\mathbf{r}_k\})\rangle$ is its mean in the H_0 ensemble. For simplicity, we take a random phase approximation and represent $\rho_2(\mathbf{x},\mathbf{y})$ by $\rho(\mathbf{x})\rho(\mathbf{y})$. Thus the free energy of the self-interacting polymer is bounded by the inequality

$$F \leq -\ln Z_0[W] - \int\rho(\mathbf{y})W(\mathbf{y})\mathrm{d}\mathbf{y} + \frac{1}{2}\int\rho(\mathbf{x})\rho(\mathbf{y})\bar{\phi}(\mathbf{x}-\mathbf{y})\mathrm{d}\mathbf{x}\mathrm{d}\mathbf{y}, \tag{3.12}$$

where $\bar{\phi}$ is the pair potential divided by k_BT, which can be separated into an attractive part $u(\mathbf{x}-\mathbf{y})$ and a repulsive part. The latter's contribution to the right hand side may be represented by a functional $F_{\mathrm{hc}}[\rho]$ given by:

$$F_{\mathrm{hc}} = \int\rho(\mathbf{r})\left[\frac{4\eta(\mathbf{r})-3\eta(\mathbf{r})^2}{[1-\eta(\mathbf{r})]^2} - \left(1-\frac{1}{N}\right)\ln\left(\frac{2-\eta(\mathbf{r})}{2[1-\eta(\mathbf{r})]^3}\right)\right]\mathrm{d}\mathbf{r}$$

where $\eta(\mathbf{r})$ is the bead packing fraction given by $\pi\rho(\mathbf{r})d^3/6$. This functional has been found to capture the thermodynamic properties of hard chains: freely jointed polymers of finite size hard spheres [65][66]. The free energy then satisfies

$$\begin{aligned} F \leq F_{\mathrm{mf}}[W] &= -\ln Z_0[W] + F_{\mathrm{hc}}[\rho] - \int\rho(\mathbf{y};[W])W(\mathbf{y})\,\mathrm{d}\mathbf{y} \\ &+ \frac{1}{2}\int\rho(\mathbf{x};[W])\rho(\mathbf{y};[W])u(\mathbf{x}-\mathbf{y})\,\mathrm{d}\mathbf{x}\mathrm{d}\mathbf{y}, \end{aligned} \tag{3.13}$$

where the functional dependence of ρ on the mean field W is explicitly noted.

The model so far has been constructed for a single polymer, but a system of M polymers in a pore can be treated by multiplying F_0 by M, by interpreting ρ in the remaining terms in equation (3.13) as the superposition of bead density profiles of the M polymers attached to their separate tether points, and by regarding the entire free energy F_{mf} as a functional of a mean field W that we assume, for simplicity, to exhibit the cylindrical symmetry of the pore.

This functional description of the free energy describes both the entropy and enthalpy of the polymer beads. There are several contributions to the total entropy of the system which we can identify from this description. The Green's function $G(\mathbf{r_0},\mathbf{r},N;[W])$ enumerates the statistical weight of the polymer of contour length N to go from point $\mathbf{r_0}$ to $\mathbf{r}$ under the external field W. By integrating this statistical weight over all possible end points $\mathbf{r}$ we determine the total free energy of a polymer tethered at r_0.

It is instructive to numerically estimate this free energy in the absence of external potential in order to estimate the effect that entropy has on polymers tethered in the cylinder. Under these

conditions, the Green's function of the polymer can be determined exactly, for a polymer starting at r_0, z_0 and finishing at r, z:

$$G(r_0, r, z0, z, N) = \sum_{k=1}^{\infty} \frac{J_0\left(\frac{r j_{0,k}}{R}\right) J_0\left(\frac{r_0 j_{0,k}}{R}\right) \exp\left(-\frac{\kappa N \left(j_{0,k}\right)^2}{R^2} - \frac{(z-z_0)^2}{4\kappa t}\right)}{2\sqrt{\pi}\sqrt{\kappa t} J_1\left(j_{0,k}\right)^2} \tag{3.14}$$

where J_k is the Bessel function of rank k and $j_{l,k}$ is the kth zero of Bessel function l.

Assuming $r_0 = 24.375$, $z_0, z = 0$ and using the parameters defined before allows us to calculate the entropy of a single polymer at different r positions.

Position (nm)	$-TS(k_bT)$
0	16.552
2	16.164
4	15.351
6	14.4778
8	13.6633
10	12.946
12	12.3441
14	11.871
16	11.5404
18	11.3721
20	11.4024
22	11.7216
24	12.7441

This table allows us to clearly see the entropic effects acting on a single polymer, without considering other interactions. There is an entropic cost to the polymer stretching towards the centre of the pore. In addition, there is an entropic penalty for the polymer to be too close to edge of the cylindrical wall. The preferred end point for the polymer is at $r = 19nm$.

When we include the other interactions into the model, the entropic effects become more difficult to quantify. However, we can make qualitative estimates of the effect of these entropic effects on our model. We have included a "hard-sphere" term into our functional. This hard sphere term accounts for the finite size of individual polymer beads. This interaction is infinite when polymer beads overlap and is zero otherwise. Thus, this term does not add any enthalpic contribution to

the free energy, it's impact is purely entropic. This term goes as $\frac{1}{(1-\eta)^2}$, which has the effect of "smearing" out the polymer density. It pushes the polymer beads further away from each other.

The best estimate of F is identified by functional minimization of the mean field formulation $F_{\mathrm{mf}}[W]$ over all possible W, to be achieved by setting the functional derivative $\delta F_{\mathrm{mf}}/\delta W(\mathbf{r})$ to zero. Several contributions to the derivative arise. We already have $\delta \ln Z_0/\delta W(\mathbf{r}) = -\rho(\mathbf{r};[W])$ from equation (2.41), and furthermore, regarding F_{hc} as a functional of either W or ρ,

$$\frac{\delta F_{\mathrm{hc}}[W]}{\delta W(\mathbf{r})} = \int \frac{\delta F_{\mathrm{hc}}[\rho]}{\delta \rho(\mathbf{y})} \frac{\delta \rho(\mathbf{y};[W])}{\delta W(\mathbf{r})} \mathrm{d}\mathbf{y} = \int \mu_{\mathrm{hc}}(\mathbf{y}) \frac{\delta \rho(\mathbf{y};[W])}{\delta W(\mathbf{r})} \mathrm{d}\mathbf{y}, \tag{3.15}$$

where μ_{hc} represents the functional derivative of F_{hc} with respect to ρ, together with

$$\frac{\delta}{\delta W(\mathbf{r})} \int \rho(\mathbf{y};[W]) W(\mathbf{y}) \mathrm{d}\mathbf{y} = \rho(\mathbf{r};[W]) + \int \frac{\delta \rho(\mathbf{y};[W])}{\delta W(\mathbf{r})} W(\mathbf{y}) \mathrm{d}\mathbf{y} \tag{3.16}$$

and

$$\begin{aligned} &\frac{\delta}{\delta W(\mathbf{r})} \int \rho(\mathbf{x};[W]) \rho(\mathbf{y};[W]) u(\mathbf{x}-\mathbf{y}) \mathrm{d}\mathbf{x}\mathrm{d}\mathbf{y} \\ &= 2 \int \frac{\delta \rho(\mathbf{y};[W])}{\delta W(\mathbf{r})} \rho(\mathbf{x};[W]) u(\mathbf{x}-\mathbf{y}) \mathrm{d}\mathbf{x}\mathrm{d}\mathbf{y}, \end{aligned} \tag{3.17}$$

giving the minimization condition as:

$$\begin{aligned} \frac{\delta F_{\mathrm{mf}}[W]}{\delta W(\mathbf{r})} &= -\int \frac{\delta \rho(\mathbf{y};[W])}{\delta W(\mathbf{r})} W(\mathbf{y}) \mathrm{d}\mathbf{y} + \int \mu_{\mathrm{hc}}(\mathbf{y}) \frac{\delta \rho(\mathbf{y};[W])}{\delta W(\mathbf{r})} \mathrm{d}\mathbf{y} \\ &+ \int \frac{\delta \rho(\mathbf{y};[W])}{\delta W(\mathbf{r})} \rho(\mathbf{x};[W]) u(\mathbf{x}-\mathbf{y}) \, \mathrm{d}\mathbf{x}\mathrm{d}\mathbf{y} = 0. \end{aligned} \tag{3.18}$$

Since

$$\frac{\delta F_{\mathrm{mf}}[W]}{\delta W(\mathbf{r})} = \int \frac{\delta F_{\mathrm{mf}}[\rho]}{\delta \rho(\mathbf{y})} \frac{\delta \rho(\mathbf{y};[W])}{\delta W(\mathbf{r})} \, \mathrm{d}\mathbf{y}, \tag{3.19}$$

this is equivalent to the condition

$$\frac{\delta F_{\mathrm{mf}}[\rho]}{\delta \rho(\mathbf{y})} = -W(\mathbf{y}) + \mu_{\mathrm{hc}}(\mathbf{y}) + \int \rho(\mathbf{x}) u(\mathbf{x}-\mathbf{y}) \mathrm{d}\mathbf{x} = 0, \tag{3.20}$$

which can be regarded as a requirement that the optimal mean field acting on each bead is a suitable embodiment of the pairwise interactions.

It is important to recognise that the mean field in DFT is a single-bead potential that is introduced to emulate the real polymer self-interactions as closely as possible. The reference Hamiltonian H_0 describes the behaviour of N freely jointed beads in the potential W, and the absence of additional bead-bead interactions simplifies its analysis considerably. The DFT-derived bead density profiles represent polymer configurations adopted in response to a mean field potential

instead of the actual self-interactions. This can be a reasonable approximation if the mean field is optimised, as can be recognised through use of the Bogoliubov inequality. Within such an approach, the best description of the interacting polymer system can be obtained by minimizing the free energy.

We now discuss algorithms to determine the optimal mean field W and associated density ρ that satisfy this condition. A steepest descent method could be employed such that ρ is updated incrementally and repeatedly in a direction down the local slope of the $F_{\rm mf}[\rho]$ surface. This can be regarded as an evolution of ρ in a fictitious time t according to

$$\frac{\partial \rho(\mathbf{y},t)}{\partial t} = -\frac{\delta F_{\rm mf}[\rho]}{\delta \rho(\mathbf{y},t)}, \tag{3.21}$$

until convergence at a time-independent density profile where the left hand side vanishes. But the right hand side of this equation requires W as a functional of ρ, which is not readily available. It is easier to determine ρ for a given W, through equation (3.4), and we might therefore consider a scheme

$$\frac{\partial W(\mathbf{r},t)}{\partial t} = -\frac{\delta F_{\rm mf}[W]}{\delta W(\mathbf{r},t)}, \tag{3.22}$$

but the problem here is that the right hand side, given by equation (3.19), requires a specification of the functional derivative $\delta\rho(\mathbf{y};[W])/\delta W(\mathbf{r})$. Instead, we employ the following arguments to formulate a third scheme. From the definition of ρ, we can write

$$\begin{aligned}\frac{\delta\rho(\mathbf{y};[W])}{\delta W(\mathbf{r})} &= -\frac{\delta}{\delta W(\mathbf{r})}\left[\frac{1}{Z_0[W]}\frac{\delta Z_0[W]}{\delta W(\mathbf{y})}\right] \\ &= \frac{1}{(Z_0[W])^2}\frac{\delta Z_0[W]}{\delta W(\mathbf{r})}\frac{\delta Z_0[W]}{\delta W(\mathbf{y})} - \frac{1}{Z_0[W]}\frac{\delta^2 Z_0[W]}{\delta W(\mathbf{r})\delta W(\mathbf{y})},\end{aligned} \tag{3.23}$$

and in view of equations (2.40) and (2.41) this becomes

$$\frac{\delta\rho(\mathbf{y};[W])}{\delta W(\mathbf{r})} = \rho(\mathbf{r})\rho(\mathbf{y}) - \langle\hat{\rho}(\mathbf{r})\hat{\rho}(\mathbf{y})\rangle\,. \tag{3.24}$$

Using the definitions of $\hat{\rho}$ and $\hat{\rho}_2$ this gives

$$\frac{\delta\rho(\mathbf{y};[W])}{\delta W(\mathbf{r})} = \rho(\mathbf{r})\rho(\mathbf{y}) - \rho_2(\mathbf{r},\mathbf{y}) - \left\langle\sum_i \delta(\mathbf{r}-\mathbf{r}_i)\delta(\mathbf{y}-\mathbf{r}_i)\right\rangle. \tag{3.25}$$

The random phase approximation that we have employed asserts that $\rho_2(\mathbf{r},\mathbf{y}) = \rho(\mathbf{r})\rho(\mathbf{y})$, so we have

$$\frac{\delta\rho(\mathbf{y};[W])}{\delta W(\mathbf{r})} \approx -\left\langle\sum_i \delta(\mathbf{r}-\mathbf{r}_i)\delta(\mathbf{y}-\mathbf{r}_i)\right\rangle, \tag{3.26}$$

and we reach the important conclusion that, if viewed as a matrix, to this level of approximation the off-diagonal elements of $\delta\rho(\mathbf{y};[W])/\delta W(\mathbf{r})$ are zero, and the diagonal elements are never positive.

Now we define a functional $\mathcal{F}[W]$ that satisfies

$$\frac{\delta\mathcal{F}[W]}{\delta W(\mathbf{r})} = -\frac{\delta F_{\rm mf}[\rho]}{\delta\rho(\mathbf{r})}, \tag{3.27}$$

and compare the variational properties of $\mathcal{F}$ with those of $F_{\rm mf}$. In view of equation (3.19), the mean field at a stationary point of $\mathcal{F}$, where $\delta\mathcal{F}[W]/\delta W(\mathbf{r}) = 0$, will minimise $F_{\rm mf}$. Next we establish that an increment in W in the direction of steepest descent of the functional $\mathcal{F}$ gives rise to a decrease in the value of the functional $F_{\rm mf}$. We show this by evaluating the analogue in function space of the dot product between two gradient vectors. We calculate, using equations (3.26) and (3.27), the projection of the functional derivative of $F_{\rm mf}[W]$ along the direction in W space of the functional derivative of $\mathcal{F}[W]$, namely the integral:

$$\begin{aligned}\int \frac{\delta\mathcal{F}[W]}{\delta W(\mathbf{r})}\frac{\delta F_{\rm mf}[W]}{\delta W(\mathbf{r})}{\rm d}\mathbf{r} &= -\int \frac{\delta F_{\rm mf}[\rho]}{\delta\rho(\mathbf{r})}\frac{\delta F_{\rm mf}[\rho]}{\delta\rho(\mathbf{y})}\frac{\delta\rho(\mathbf{y})}{\delta W(\mathbf{r})}{\rm d}\mathbf{y}{\rm d}\mathbf{r} \\ &\approx \left\langle \sum_{i=1}^{N} \frac{\delta F_{\rm mf}[\rho]}{\delta\rho(\mathbf{r}_i)}\frac{\delta F_{\rm mf}[\rho]}{\delta\rho(\mathbf{r}_i)} \right\rangle,\end{aligned} \tag{3.28}$$

so that $\int[\delta\mathcal{F}[W]/\delta W(\mathbf{r})][\delta F_{\rm mf}[W]/\delta W(\mathbf{r})]{\rm d}\mathbf{r} \geq 0$ to this level of approximation. The functional $\mathcal{F}$ has a minimum at the mean field W that minimises $F_{\rm mf}$, and an infinitesimal move along a path of steepest descent of the $\mathcal{F}$ surface also takes us downhill on the $F_{\rm mf}$ surface.

All this provides support for an algorithm for identifying the optimal mean field and free energy based on solving the equation

$$\frac{\partial W(\mathbf{r},t)}{\partial t} = -\frac{\delta\mathcal{F}[W]}{\delta W(\mathbf{r},t)} = \frac{\delta F_{\rm mf}[\rho]}{\delta\rho(\mathbf{r},t)}, \tag{3.29}$$

which is free of the above-mentioned problems of schemes (3.21) and (3.22).

Putting this scheme into practice, and using equation (3.20), we discretise the spatial variable and the time and employ a forward Euler numerical scheme with update rule

$$\begin{aligned}W^{n+1}(\mathbf{y}_k) = W^n(\mathbf{y}_k) + \Delta t\Big[&-W^n(\mathbf{y}_k) + \mu^n_{\rm hc}(\mathbf{y}_k) \\ &+ \sum_j \rho^n(\mathbf{x}_j)u(\mathbf{x}_j - \mathbf{y}_k)\Delta\mathbf{x}\Big],\end{aligned} \tag{3.30}$$

where n labels discrete time and subscripts j and k label discrete spatial points, and $\Delta\mathbf{x}$ is the volume element. At each iteration starting with a mean field $W^n(\mathbf{y}_k)$, we use equations 2.44 and

2.45 to generate the reference system bead density profile $\rho^n(\mathbf{y}_j)$ that is associated with this choice. Through equation (3.30) with a given timestep Δt this gives us a new mean field $W^{n+1}(\mathbf{y}_k)$ and the process is repeated until the change in mean field falls below a chosen tolerance. The converged field gives a minimised free energy $F_{\rm mf}$ which provides an upper limit to the actual free energy F of the self-interacting polymer system.

In fact, it proves to be more efficient to conduct the minimization of $F_{\rm mf}[W]$ using a modified conjugate gradient scheme. It is well known that such a scheme normally takes the form of repeated line minimization of the functional along directions chosen in W space that are selected according to the local gradient $\delta F_{\rm mf}/\delta W(\mathbf{r})$ and the direction of the preceding line search. We employ the Polak-Ribiere version of this scheme but our modification is to select directions based on the functional derivative $\delta\mathcal{F}/\delta W(\mathbf{r})$ instead. This is in the same spirit as the use of equation (3.29) instead of equation (3.22). The minimization of $F_{\rm mf}$ is performed numerically by stepping along the chosen direction in a space spanned by the discrete $W^n(\mathbf{y}_k)$ until we encounter a change in sign of the difference $\Delta F_{\rm mf}$ with respect to the previous value. A new search direction is then established and the process repeated. The scheme appears to be numerically robust in practice, an indication that our consideration of the properties of the functionals $F_{\rm mf}$ and $\mathcal{F}$ is sound.

3.2 Comparison between MC and DFT

A key test of the DFT model, and of the numerical scheme, is to compare bead density profiles with those obtained by MC simulation. We look first at polymers interacting only through hard sphere repulsion, represented in the DFT by the contribution in equation (3.13). The comparison shown in figure 3.3 shows a good agreement between the two schemes, indicating that the DFT approach captures the essence of the excluded volume behaviour.

Next, we include long range interactions and make a similar comparison between DFT and MC results. This test is more challenging since there is now competition between polymer attraction and repulsion, giving rise to quite distinct configurations, as we saw earlier for the MC alone. Whilst the DFT can treat cases with different radial density profiles, it presently does not explicitly allow for azimuthal clumping. figure 3.4(a-b) illustrates two converged density profiles obtained from the DFT approach, arising from different choices for the initial mean field. They are the counterparts to the wall and central phases observed in Monte Carlo simulations seen in figure 3.2, and use the

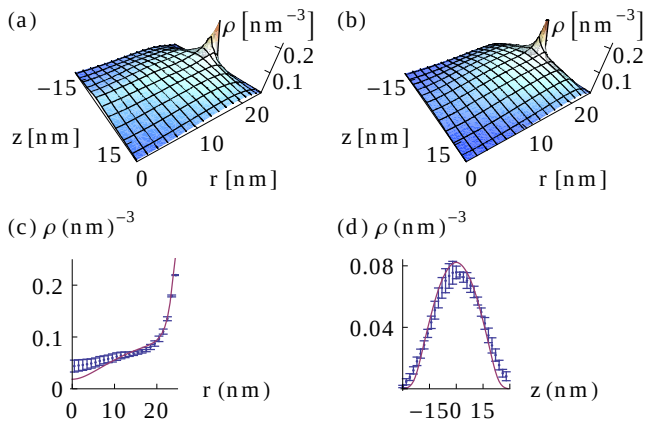

Figure 3.3: Mean bead density profiles for Monte Carlo (MC) simulations (a) and DFT calculations (b) for 40 polymers, composed of 100 beads each, tethered within a cylinder, and interacting only through hard sphere interactions. The plots are given for a range of radial (r) and axial (z) coordinates. (c) and (d) show more detailed comparisons of the profiles as a function of, respectively, the radial direction in the plane of the tethering ring ($z = 0$), and the axial direction at a radius $r = 17.5$ nm. DFT results are given by the solid lines and the statistical uncertainty in the MC results is indicated with error bars.

same set of interaction parameters, namely $\epsilon = 0.1\, k_B T$ and $\lambda = 1.0$ nm. A detailed comparison of the centrally peaked profiles with MC results in Figs. 3.4(d) and (f) suggests that the radial and axial spread of the polymers determined from each approach are consistent with one another. For the wall phase, the DFT and MC profiles do differ, as illustrated radially and axially in Figs. 3.4(c) and (e). The differences might be due to the angular symmetry breaking, or clumping, observed in the Monte Carlo simulations, but this would not be expected to affect the qualitative conclusions about the stability or metastability of the two phases that we now explore. We shall explore the effect of this symmetry breaking in the next chapter.

3.3 Phases of cylindrically bound polymers

The great benefit of the DFT model is that it provides thermodynamic properties of the interacting polymers within the pore, not just the structural properties that are available using MC. It provides estimates of the free energy, such that it is possible to determine which phase, central or wall, is thermodynamically stable or metastable under a range of interaction conditions.

In figure 3.5 we plot the difference in free energy between wall and central profiles $\Delta F_{\rm p}$, per

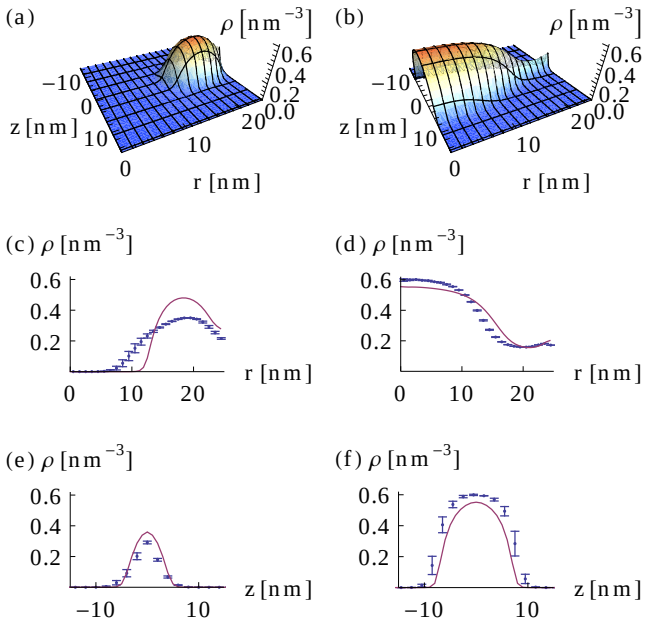

Figure 3.4: Converged polymer configurations and bead density profiles calculated for an attractive pair potential of depth $\epsilon = 0.1\,k_BT$ and range $\lambda = 1.0$ nm in a pore of 25 nm radius. The data in the left and right column correspond to initial conditions with the 40 polymers concentrated at the wall and at the centre, respectively. (a-b) DFT results with parameters corresponding to the Monte Carlo simulations, as a function of radial (r) and axial (z) position. (c-d) Comparison of Monte Carlo (with error bars) and DFT (smooth curves) radial profiles for $z = 0$, the plane of the tethering points. Axial profiles (e) for the wall phase at $r = 22.5$ nm and (f) for the central phase at $r = 2.5$ nm.

polymer and in units of k_BT, against interaction range λ and strength ϵ. The plot illustrates the free energy difference as a surface extending across regions where, respectively, the central phase ('Centre stable, wall metastable') and the wall phase ('Centre metastable') are thermodynamically stable and the other phase is metastable. The region in the foreground ('Wall only') denotes conditions where only the wall phase appears to exist. Similarly, there is a corresponding region where only the central phase exists towards the back of the diagram ('Centre only'). There is a binodal line, or phase boundary, where wall and central phase coexist, together with spinodals denoting the extremes of metastability of one of the phases with respect to the other. When we extend the range of ϵ to larger values, i.e. stronger attractions than those shown, we find that the phase boundary continues in such a manner such that a central phase is increasingly favoured.

The metastability diagram demonstrates that central polymer condensation is a natural result

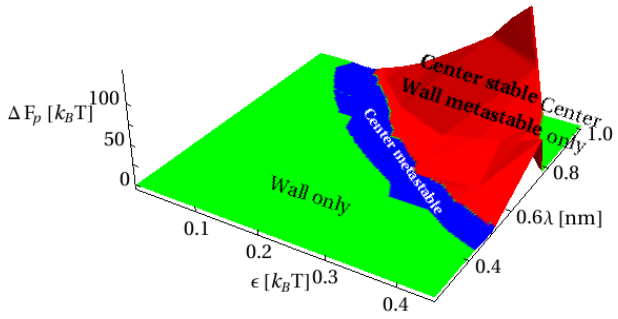

Figure 3.5: Metastability diagram of the polymer phases (wall phase and central phase) as a function of strength ϵ and range λ of the attractive interactions. ΔF_{p} indicates the free energy difference per polymer between the wall and central phases, for parameters where they can both exist as a stable and metastable state. The coexistence conditions lie along the boundary between blue and red regions. In the green region, only one phase is found to be possible: the metastability of the other has been lost.

of attractive interactions, provided that their range and strength are sufficiently large. This is in accord with intuition, which suggests that a central phase can be stabilised by a reduction in energy to balance the cost in entropy of extending the polymers away from the wall. A long range attractive potential will favour this by allowing polymers to interact with more of their counterparts across the other side of the pore. If the range were reduced, then the required strength of the attraction would have to be greater to produce the same effect. Repulsive interactions do not drive bistable phase behaviour. Instead the polymer condensate becomes more homogeneous as the strength of the repulsion is increased: such behaviour is equivalent to that of a good solvent.

In our model system we do not explicitly include water, instead it takes an implicit role as the cause of the interactions between the polymer beads, which we view as hydrophobic. Including water within the simulation could potentially lead to several effects:

- Perhaps most obviously, the water physically occupies space in the Nuclear Pore Complex, limiting the freedom of the polymers to move around the pore.

- Water will aggregate around hydrophilic regions of the nups. This will increase the effective diameter of these regions. Due to the hard sphere term this would lead to the nups being more spread out.

- Hydrophobic regions of the polymers will no longer have an explicit enthalpic interaction

with one another. Instead, the attraction between hydrophobic regions of the polymer would be treated as repulsive interaction with water, causing hydrophobic regions to aggregrate together.

In our model, we assume the inclusion of water would be similar to changing the effective interaction parameters between the polymers. In other words, whilst the inclusion of water may change the polymer distribution, we would still expect to find central or wall phases depending on the parameters chosen.

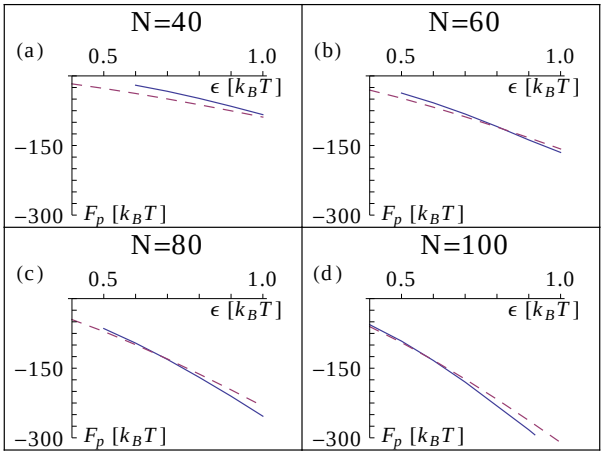

Figure 3.6: Free energies of the central phases (solid) and wall phases (dashed) for systems with a range of bead number N, per polymer, for interaction range $\lambda = 0.5$ nm, plotted as a function of interaction strength ϵ. The phase with the lower free energy is thermodynamically stable. The limited extent of the curve of higher free energy, in some cases, is an illustration of the limits of the metastability of that phase, equivalent to spinodal behaviour. As N increases, the central phase becomes stable over a larger range of ϵ.

In addition to changing the strength and range of the polymer interactions, we can also explore the effect of a change in the number of beads N in each polymer. For constant segment length b, this is equivalent to altering the length of the polymer. Reducing N has the dual effect of increasing the entropic cost of stretching a polymer towards the centre of the pore, and of decreasing the binding energy that can be experienced by each polymer. Both effects hinder central phase formation, and this is borne out in calculations of free energies for the two phases as a function of interaction strength ϵ for a range of N, as shown in figure 3.6 for $\lambda = 0.5$ nm. Shortening the length of the polymers requires a stronger attractive potential for the polymers to condense towards the pore

centre, as is to be expected.

We also explored the effect of increasing the number of polymers tethered around the edge of the ring. By looking at $M = 80$ and $M = 200$ we can observe how the density of tethering points effects the distribution of the polymers. Increasing the number of polymers tethered around the same ring reduces the difference between the central and wall phases. Essentially, by adding more polymers around the edge of the cylinder we are increasing the importance of the steric repulsion between the polymers. This leads to a more uniform distribution of polymers across the whole pore, even in the absence of attractive interactions. For 200 polymers tethered around a ring, there is no "central" or "wall" phase.

On the basis of these Monte Carlo and density functional theory calculations, we find that polymers tethered around a ring inside a cylindrical geometry can exhibit bistable behaviour, switching between a wall- and a centrally condensed phase depending on the interaction parameters. Interestingly, this behaviour is observed for a geometry and polymer structural properties that closely resemble the NPC [59, 60, 61, 1], for entirely realistic ranges ($\lambda \lesssim 1$ nm) and strengths ($\epsilon \lesssim 1\, k_B T$) of intermolecular interactions [37] within the NPC. The existence of a central polymer condensate is reminiscent of the central 'plug' or 'transporter' structure of nucleoporins that has been observed by cryo-electron microscopy of the nuclear pore complex (NPC) [1, 25], though our model would need to be developed to treat a more realistic geometry if it were to be considered a proper representation. Nevertheless, our thermodynamic model suggests that a phase transition from the central to the wall phase occurs when the effective strength or range of the attraction between polymer segments is decreased. Equivalently, the transition might be induced by increasing the prevailing temperature. If we were to apply our model to the NPC, this feature would be in agreement with the experimentally observed dissolution of the central plug at higher temperature [2]. A similar effect has been seen upon incubation of the NPC with nuclear transport receptors [67]. A possible interpretation of this effect is that the nuclear transport receptors are responsible for a weakening of the nucleoporin self-attraction and that their influence on the polymer plug provides a mechanism for the differential permeability of the NPC. In this scenario, a sufficiently high concentration of nuclear transport receptors disturbs the thermodynamic stability of the central structure to the extent that the polymers withdraw towards the wall, leaving a free passage to be occupied and traversed by receptors and receptor-bound cargoes. Such a mechanism, if it operates, could be exploited in the design of artificial nanopores that might perform similar differential

transport of a variety of molecular species.

In conclusion, in this chapter we have studied the conformations of polymers in a cylinder, which we take as our simplified model of nucleoporins in the NPC. The key finding is that such a system has a bimodal distribution of polymers. That is to say, depending on the interaction strength, there is a phase where the polymers can aggregate in the centre of the pore, and there is a phase where the polymers stay close to their tethering points at the channel wall. These two phases can exist for the same parameter set. We then observe how these phases are affected by other parameters such as tethering density at the wall and length of the polymers.

As has been mentioned, these results assume that the density of the polymers is independent of the angle around the central axis of the pore. In the next chapter, we revisit this assumption in detail.

Chapter 4

Rotational Symmetry Breaking

Throughout the previous results we have employed the assumption that the *polymer* density of the system is independent of the angle around the centre of the channel. In this chapter, we revisit this assumption and justify its use by carrying out simulations on a two dimensional pore. This simplified system allows us to explore the phenomenology of angular symmetry breaking.

In general, tethered polymer systems have differing phase behaviour depending on the intermolecular interactions. These phases are categorised by the scaling behaviour of the radius of the gyration of the polymers[68], and labelled as "mushrooms" or "brushes". As shown in chapter 3, when the polymers are tethered to the inside of a curved surface, such as the circumference of a nanopore, these behaviours are complemented further by two gross phases that differ from the simple swelling and collapsing of a polymer brush. They can broadly be categorised as "wall phases" where the majority of the polymer density is found closer to their tethering points, and a "central phase" where the polymers stretch away, at an entropic cost, from their tethering points and meet in the central channel of the nanopore, as can be seen from the previous chapter and other studies [48].

The primary driver of this change in conformation is the minimization of the surface area of the polymer condensate. However, the wall phase can further reduce its surface area by condensing in separate clumps along the circumference of the pore, such that the average position of the polymers is still close to the wall, but they form into separate regions of large polymer density arranged around the nanopore circumference. Such clumping will have an impact upon the phase diagram of polymer conformations by lowering the free energy of the wall phase.

In order to understand this better, we determine how rotational symmetry breaking affects the

stability of the previously observed central phase. We do this using several methods: Monte Carlo simulations, density functional theory calculations and a simple analytical treatment.

4.1 Two dimensional density functional theory

Our study builds upon the three dimensional analysis where we observed rotational symmetry breaking in Monte Carlo simulations of a polymer-coated cylinder. For simplicity and computational tractability we restrict our analysis to two dimensional systems, i.e., here we consider only variations as a function of radial and azimuthal coordinates. The model system is as follows: a number M of polymers consisting of N identical disks tethered around the circumference of a circle of radius R, as schematically illustrated in figure 4.1A. The disks are separated from each other by a bond length b, and as before the polymers interact with each other through the following potential:

$$\phi(\mathbf{r}) = \begin{cases} \infty & |\mathbf{r}| < d \\ -\epsilon \exp(-(|\mathbf{r}| - d)/\lambda) & |\mathbf{r}| \geq d \end{cases} \tag{4.1}$$

where d is the diameter of the disk, $\mathbf{r}$ is the vector connecting the centres of both beads, ϵ is the potential depth and λ represents the range of the interaction. The system was studied using Monte Carlo, density functional theory and analytical calculations. The Monte Carlo simulations were performed using the Metropolis algorithm[49] on systems of tethered polymers and the density functional theory is adapted from the functional used in the previous chapter (equation 3.13). The analytical work is based on simple representations of polymer behaviour.

Monte Carlo simulations of 2D polymers with a fixed bond length constraint have difficulties with convergence. If we consider three consecutive disks along a polymer there are only two positions that the central disk of the three can take that preserve the fixed bond length constraint. Because there is only one possible move per disk for any conformation that keeps the bond length constant, Monte Carlo performed in this way is slow to converge. The disk at the end of the polymer is the only one which has a continuous range of possible moves. Moves that rotate a greater number of disks around a fixed disk could be considered, but the difficulty of avoiding disk overlap limits the likelihood that updates which move a large number of disks would be accepted. Therefore the Monte Carlo results presented here should be viewed more as indicative of the equilibrium structure rather than exact quantitative representations of it.

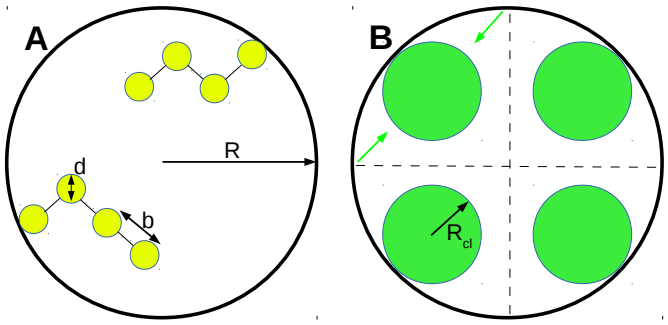

Figure 4.1: A) An overview of our model system. We consider M polymers of N disks tethered on the inner surface of a circle, illustrated here for the case $M = 2$ and $N = 4$. B) Basis of the analytical model used to interpret the results. We divide the pore into N_c sections, in each of the tethered polymers stretch to form a clump in the centre of the section, as indicated by the green arrows. In this case $N_c = 4$. The change in total free energy is given by the entropic cost of extending the polymers together with the total energy of the polymer phase which depends on the change in the length of the interface it forms with the surrounding medium.

A more robust but necessarily simplified density functional theory of the system was also used to obtain the equilibrium densities of the polymers. For density functional theory calculations we use the following free energy functional, slightly modified from the previous three dimensional case, for the system considered here. In particular, modifications to the excluded volume term to account for the change in dimension.

$$\beta F[W(\mathbf{r})] = -\sum_{r_0} \ln Z[W(\mathbf{r}), \mathbf{r_0}] - \int W(\mathbf{r})\rho(\mathbf{r})\,\mathrm{d}\mathbf{r} + \int V(\mathbf{r})\rho(\mathbf{r})\mathrm{d}\mathbf{r} + \int \mathrm{d}\mathbf{r}\,\left\{\Phi^{HD}(\mathbf{r}) + \Phi^{ch}(\mathbf{r})\right\} \tag{4.2}$$

$$+ \frac{1}{2}\iint \mathrm{d}\mathbf{r}\mathrm{d}\mathbf{r}'\rho(\mathbf{r})\rho(\mathbf{r}')\phi(\mathbf{r}-\mathbf{r}')$$

where F is the total free energy of the system. $W(\mathbf{r})$ is a "mean-field" potential, which can be mapped to a disk density $\rho(\mathbf{r})$. $V(\mathbf{r})$ is the external potential that acts on the polymers, here set to 0. Φ^{HD} gives the excess free energy density arising from the excluded volume imposed by the hard disks, and is given by[69]

$$\Phi^{HD}(\mathbf{r}) = \rho(\mathbf{r})\left(\frac{\eta(\mathbf{r})}{1-\eta(\mathbf{r})} - \ln(1-\eta(\mathbf{r}))\right) \quad , \tag{4.3}$$

where $\eta(\mathbf{r})$ is the packing fraction in two dimensions, given by $\rho(\mathbf{r})\pi d^2/4$ with d as the diameter of the disk. Φ^{ch} is the "chain connectivity" term, which accounts for excess free energy due to the

fact the hard disks are joined together. It is given by[65, 66]

$$\Phi^{ch}(\mathbf{r}) = \frac{1-N}{N} \ln\left(\frac{2-\eta(\mathbf{r})}{2(1-\eta(\mathbf{r}))^3}\right) \tag{4.4}$$

We introduce a Green's function $G(\mathbf{r}_0, \mathbf{r}, s; [W])$ that satisfies

$$\frac{\partial G(\mathbf{r}_0, \mathbf{r}, s; [W])}{\partial s} = \left(\frac{b^2}{4}\nabla^2 - W(\mathbf{r})\right) G(\mathbf{r}_0, \mathbf{r}, s; [W]) \tag{4.5}$$

where b is the segment length of the polymer. This equation is the same form as the previously defined Green's functions, however, as we are now working in two dimensions, the factor in front of the Laplacian becomes $b^2/4$ rather than $b^2/6$. This equation is to be solved for every tethering point $\mathbf{r_0}$ of the polymers around the circumference of the circle. From $G(\mathbf{r}_0, \mathbf{r}, s; [W])$ we calculate the density in the following way:

$$\rho(\mathbf{r}) = \frac{\int_0^N \mathrm{d}s \int \mathrm{d}\mathbf{r}' \sum_{r_0} G(\mathbf{r}_0, \mathbf{r}, N-s; [W]) G(\mathbf{r}, \mathbf{r}', s; [W])}{\int \mathrm{d}\mathbf{r}' \sum_{r_0} G(\mathbf{r}_0, \mathbf{r}', N; [W])} \tag{4.6}$$

thereby taking into account polymers arranged to every tethering point $\mathbf{r_0}$ in the system. $Z[W(\mathbf{r}), \mathbf{r_0}]$ represents the partition function of a polymer tethered at $\mathbf{r_0}$ and is given by:

$$Z[W(\mathbf{r}), \mathbf{r_0}] = \int G(\mathbf{r}_0, \mathbf{r}, N; [W]) \mathrm{d}\mathbf{r} \quad , \tag{4.7}$$

The method for obtaining equilibrium densities requires the minimization of the free energy $F[W(\mathbf{r})]$. We use a steepest descent scheme involving the functional derivative of F:

$$\frac{\partial W(\mathbf{y})}{\partial t} = \frac{\delta F[W(\mathbf{r})]}{\delta W(\mathbf{y})} \tag{4.8}$$

where we have introduced a fictional time variable t. Discretizing this equation leaves us with the following form, which is useful for calculations:

$$W^{n+1}(\mathbf{y}) = W^n(\mathbf{y}) + \Delta t \frac{\delta F[W(\mathbf{r})]}{\delta W^n(\mathbf{y})} \tag{4.9}$$

The complete method for solving for equilibrium densities is thus: the mean field is initialised to a certain value W_0, from which equation (4.5) and equation (4.6) are used to obtain the density ρ. Once the density is obtained, the value of the functional derivative of the free energy at this mean field and density is calculated, and this is then used to update the mean field according to equation (4.9). This process is repeated until the system has reached convergence, i.e. the free energy and density no longer change after updates. This process is repeated ten times for each parameter set in order to find the global minimum for each case. The field W_0 is initialised to random values using a random number generator. This ensures that the rotational symmetry is broken: if this were not imposed, the algorithm would maintain the symmetry.

4.2 Analytical approach to symmetry breaking in nanopores

By considering the change in entropy of the polymers as they stretch away from their tethering points together with the the total energy of each clump, we can write down a simple form for the change in free energy upon breaking the the rotational symmetry of the wall phase.

We denote the number of clumps as N_c and we make the following assumptions about them and the rest of the system:

- The clumps are circular with a radius R_{cl}. If the clumps lie against the wall their centres will be a distance R_{cl} from the wall. If there is only one clump it will be in the centre. The clumps are identical.

- The system maintains "maximal symmetry" for instance, if there 3 clumps, a rotation of the system by $\frac{2\pi}{3}$ will leave the system invariant. In other words, the clumps will be on the vertices of a regular polygon. For practical purpose we divide the circle into N_c equal sectors, and all polymers tethered within one section would form one clump at the centre of that section.

- The density of disks within any clump is constant, and is related to the inverse of the disk diameter squared.

- The entropy difference between different states is given by the differing entropic costs of extending the polymers from their tether points to the centre of each clump.

- The entropic contribution to the free energy will be given by the cost of extending the polymers, given by:

$$\Delta S_1(\mathbf{r}) = -\frac{k_b}{Nb^2} r^2 \tag{4.10}$$

  where $\mathbf{r}$ is the end to end distance, k_b is the Boltzmann constant and T is the temperature

The system being treated is shown in figure (4.1). In this case, $N_c = 4$. The polymers stretch from each quadrant edge towards the centre of that quadrant's clump.

The free energy change of this system is given by:

$$\Delta F = \Delta E - T\Delta S \tag{4.11}$$

We will work out all of these terms one by one. The total entropy change will be given by the entropy change of extending the polymers.

$$T\Delta S = -N_c \frac{k_b T}{Nb^2} \sum_{i=1}^{M/N_c} \left(R^2 + (R - R_c)^2 - 2(R - R_c) R \cos(\theta_i) \right) \ . \tag{4.12}$$

This can be understood as a summation of the contributions of all the polymers in a quadrant N_c as they stretch from $r = R$ and $\theta = \theta_i$ to $r = R_{cl}$ and $\theta = 0$. For analytical reasons, we assume that the polymers are tethered uniformly and continuously along the circumference of the circle, in which case we would modify our discrete representation to:

$$T\Delta S(N_c \geq 2) = -N_c \frac{k_b T}{Nb^2} \rho_s \times \int_{-\pi/N_c}^{\pi/N_c} \left(R^2 + (R - R_c)^2 - 2(R - R_c) R \cos(\theta) \right) \mathrm{d}\theta$$

where ρ_s is the angular tethering density, i.e $2\pi\rho_s = M$

This integral can be evaluated to yield:

$$T\Delta S(N_c \geq 2) = -N_c \frac{M k_b T}{2\pi N b^2} \times \left(\frac{2\pi \left(R^2 + (R - R_c)^2 \right)}{N_c} + 4R(R_c - R) \sin\left(\frac{\pi}{N_c} \right) \right)$$

R_c has a subtly different meaning to R_{cl}, the radius of the clump. When the clump number is greater than 2, R_c will be given by R_{cl}, however in the case of $N_c = 1$ then $R_c = R$, as the clump will be in the centre rather than at the wall. R_c quantifies the radial position of the clump away from the wall, whereas R_{cl} is the radius of the clump, in our model they are the same except when $N_c = 1$, such that when $N_c = 1$ the following is the form of the entropy change:

$$T\Delta S(N_c = 1) = -\frac{M k_b T R^2}{Nb^2} \tag{4.13}$$

To calculate the clump radius R_{cl}, we use the incompressibility condition to calculate the clump radius:

$$\frac{NM}{N_c \pi R_{cl}^2} = \frac{4\eta}{\pi d^2} \tag{4.14}$$

$$R_{cl} = \sqrt{\frac{NM}{4N_c \eta}} d \tag{4.15}$$

where η sets the packing fraction, of the same type as seen in density functional theory.

The total internal energy of a clump is given by the sum of intermolecular interactions within the clump. We assume that the inter-clump interactions are negligible. This assumption will hold when there aren't many clumps, such that the distance between clumps is large.

$$E_c = \frac{1}{2} \int \rho(\mathbf{r}') \rho(\mathbf{r}) \phi(\mathbf{r} - \mathbf{r}') \mathrm{d}\mathbf{r} \mathrm{d}\mathbf{r}' \tag{4.16}$$

The full form of the intermolecular interaction is as follows:

$$\phi(\mathbf{r}-\mathbf{r}') = \epsilon \exp\left(-\frac{|\mathbf{r}-\mathbf{r}'|-d}{\lambda}\right)\Theta\left(|\mathbf{r}-\mathbf{r}'|-d\right) \tag{4.17}$$

where Θ is the Heaviside step function. In its full form $|\mathbf{r}-\mathbf{r}'|$ is given by:

$$|\mathbf{r}-\mathbf{r}'| = (r^2 + r'^2 - 2rr'\cos\theta)^{\frac{1}{2}} \tag{4.18}$$

Using the assumption that the density of the clump is constant and rearranging we obtain:

$$E_c = \epsilon\rho^2\pi \exp\left(\frac{d}{\lambda}\right)\int_0^{R_c}\mathrm{d}r\int_0^{R_c}\mathrm{d}r'\int_0^{2\pi}\mathrm{d}\theta rr' \exp\left(-\frac{|\mathbf{r}-\mathbf{r}'|}{\lambda}\right) \times \Theta\left(|\mathbf{r}-\mathbf{r}'|-d\right) \tag{4.19}$$

If we assume that the diameter of the bead is small in comparison to the radius of the clump (again true for low numbers of clumps) then we ignore the Heaviside function for analytical tractability, giving:

$$E_c = \pi\epsilon\rho^2 \exp\left(\frac{d}{\lambda}\right) R_c^4\int_0^1\mathrm{d}x\int_0^1\mathrm{d}x'\int_0^{2\pi}\mathrm{d}\theta xx' \exp\left(-\frac{R_c}{\lambda}|\mathbf{x}-\mathbf{x}'|\right) \tag{4.20}$$

where $x = r/R_c$ and $x' = r'/R_c$. The integral can be evaluated approximately to give:

$$E_c = \epsilon\rho^2 \exp\left(\frac{d}{\lambda}\right)\pi^2 R_c^2\lambda^2\left(1-\exp\left(-\frac{R_c}{\lambda}\right)\left(1+\frac{R_c}{\lambda}\right)\right) \tag{4.21}$$

such that the total energy will be given by $E = N_c E_c$. Using the relation between R_c and N_c allows us to write the energy in terms of clump number.

$$E = \epsilon \exp\left(\frac{d}{\lambda}\right) NM\lambda^2\pi\rho \times \left(1-\exp\left(-\frac{1}{\lambda}\sqrt{\frac{NM}{\pi N_c\rho}}\right)\left(1+\frac{1}{\lambda}\sqrt{\frac{NM}{\pi N_c\rho}}\right)\right) \tag{4.22}$$

where we can see that the energy change upon changing the number of clumps is given by:

$$\Delta E = -\epsilon \exp\left(\frac{d}{\lambda}\right) NM\lambda^2\pi\rho \times \exp\left(-\frac{1}{\lambda}\sqrt{\frac{NM}{\pi N_c\rho}}\right)\left(1+\frac{1}{\lambda}\sqrt{\frac{NM}{\pi N_c\rho}}\right) \tag{4.23}$$

Combining the energy and the entropy gives us the free energy, and is thus given by:

$$\Delta F(N_c) = -N_c\frac{Mk_bT}{2\pi Nb^2} \times \left(\frac{2\pi(R^2+(R-R_c)^2)}{N_c}+4R(R_c-R)\sin\left(\frac{\pi}{N_c}\right)\right) - \epsilon\exp\left(\frac{d}{\lambda}\right)NM\lambda^2\pi\rho\exp\left(-\frac{1}{\lambda}\sqrt{\frac{NM}{\pi N_c\rho}}\right)\left(1+\frac{1}{\lambda}\sqrt{\frac{NM}{\pi N_c\rho}}\right) \tag{4.24}$$

A plot of the form of the free energy change against clump number is shown in figure 4.2

The only free parameter in this simple analytical model is the polymer disk density ρ, and since this parameter varies when we modify ϵ and λ, we take this parameter from the theoretical results obtained in density functional theory.

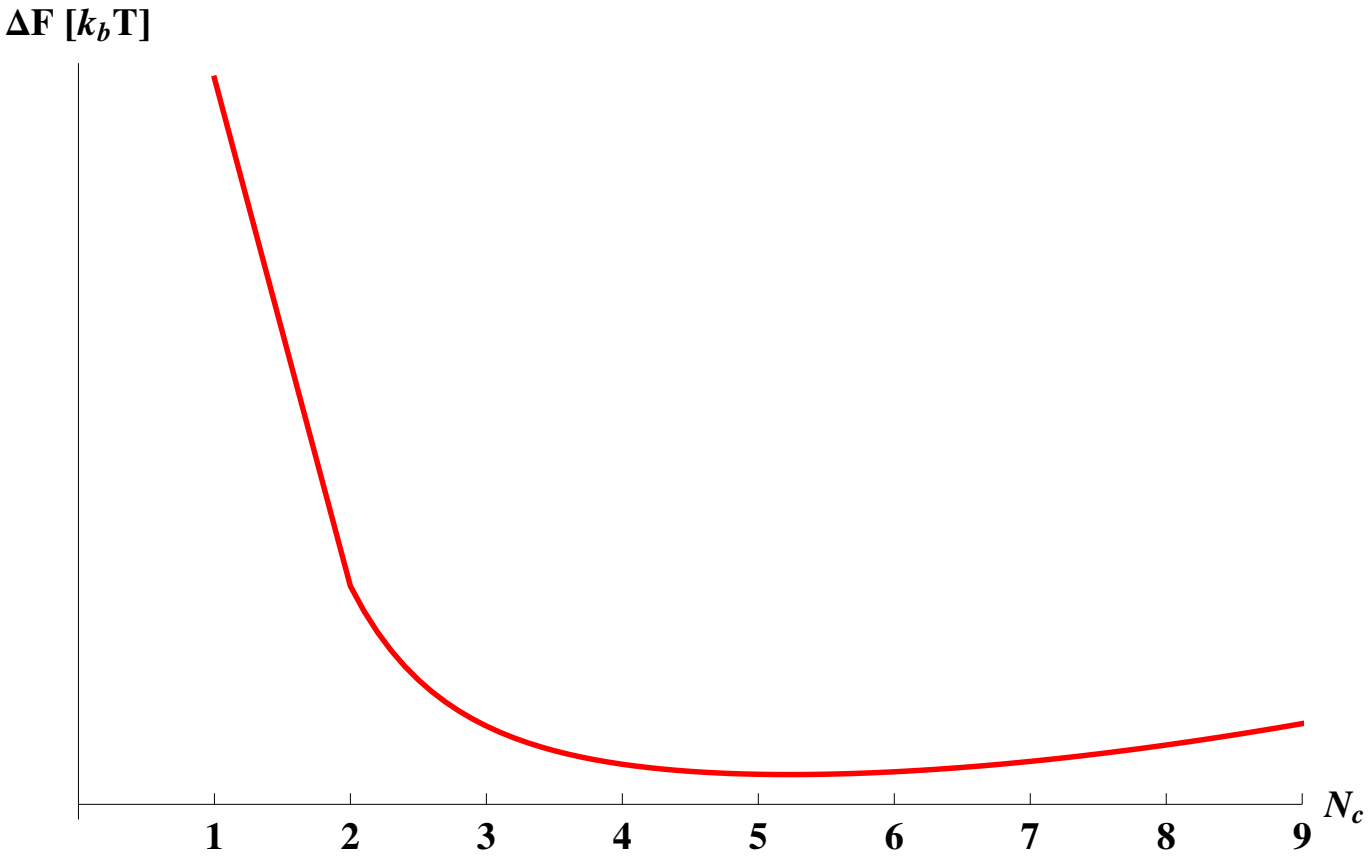

Figure 4.2: Form of the analytic free energy change against the clump number N_c for a specific set of parameters: $N = 100$, $M = 25$, $d = 0.25\,\mathrm{nm}$, $R = 25\,\mathrm{nm}$, $b = 1\,\mathrm{nm}, \epsilon = 0.07\,\mathrm{k}_b T$, $\lambda = 0.5\,\mathrm{nm}$ at these parameter sets the packing fraction η is 0.383989. Plotted is the change in free energy ΔF as the number of clumps in the system is changed. The curve has a minimum for some value of N_c, corresponding to the number of preferred clumps at equilibrium.

4.3 Impact of rotational symmetry breaking on polymer phases

The calculations were performed with the parameters $M = 25$, $N = 100$, $b = 1.0$ nm, $d = 0.25$ nm and $R = 25$ nm. The behaviour of the system was established for a range of the interaction parameters ϵ and λ.

Monte Carlo simulations can illustrate the propensity of the system to display rotationally asymmetric behaviour. figure 4.3 gives an example of the clumping behaviour of polymers in a pore, as well as figure 3.2 from chapter 3. The system breaks rotational symmetry for certain

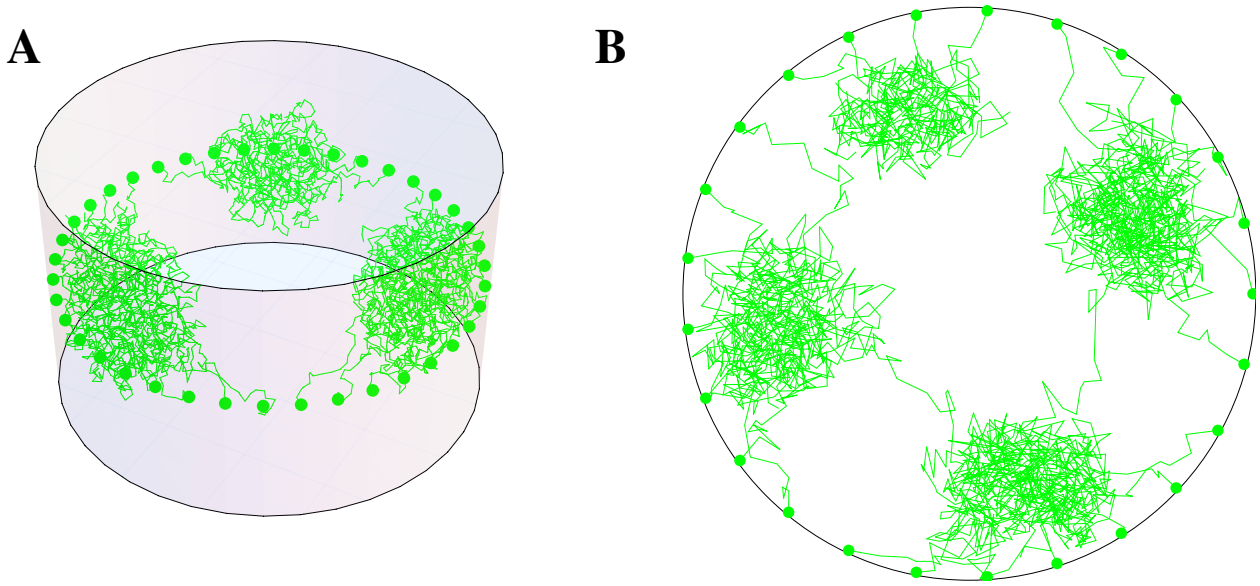

Figure 4.3: Monte Carlo snapshots of polymers tethered to a circular ring on the inside of a 3D cylinder (A) and to the inside of a circle in 2D (B). The Monte Carlo simulations show that clumping behaviour can emerge in both two and three dimensions for interaction parameters (A) $\epsilon = 0.1, \lambda = 1.00$ (B)$\epsilon = 0.04, \lambda = 1.25$, motivating more quantitative methods for determining the clump phase.

parameters in both two and three dimensions.

Convergence issues with Monte Carlo, discussed before, potentially limit the reliability of this approach. Therefore we use the density functional theory. We perform calculations with and without the rotational symmetry constraint. By comparing the resulting phase diagrams, the effect of rotational symmetry breaking on the phase of the system can be determined. We verify density functional theory results for the predicted clump number by Monte Carlo simulations for the same parameters.

Because of the problems in the convergence of Monte Carlo, precise quantitative agreement between density functional theory and Monte Carlo is hard to achieve. Nevertheless, there is a qualitative similarity in the obtained results from the two different methods, as can be seen from figure 4.4.

figure 4.5 shows an example of the various phases obtained from the density functional theory approach. It is observed that there is a multiplicity of wall states, with different numbers of clumps. There exist many metastable states for each parameter set, necessitating the calculations to be

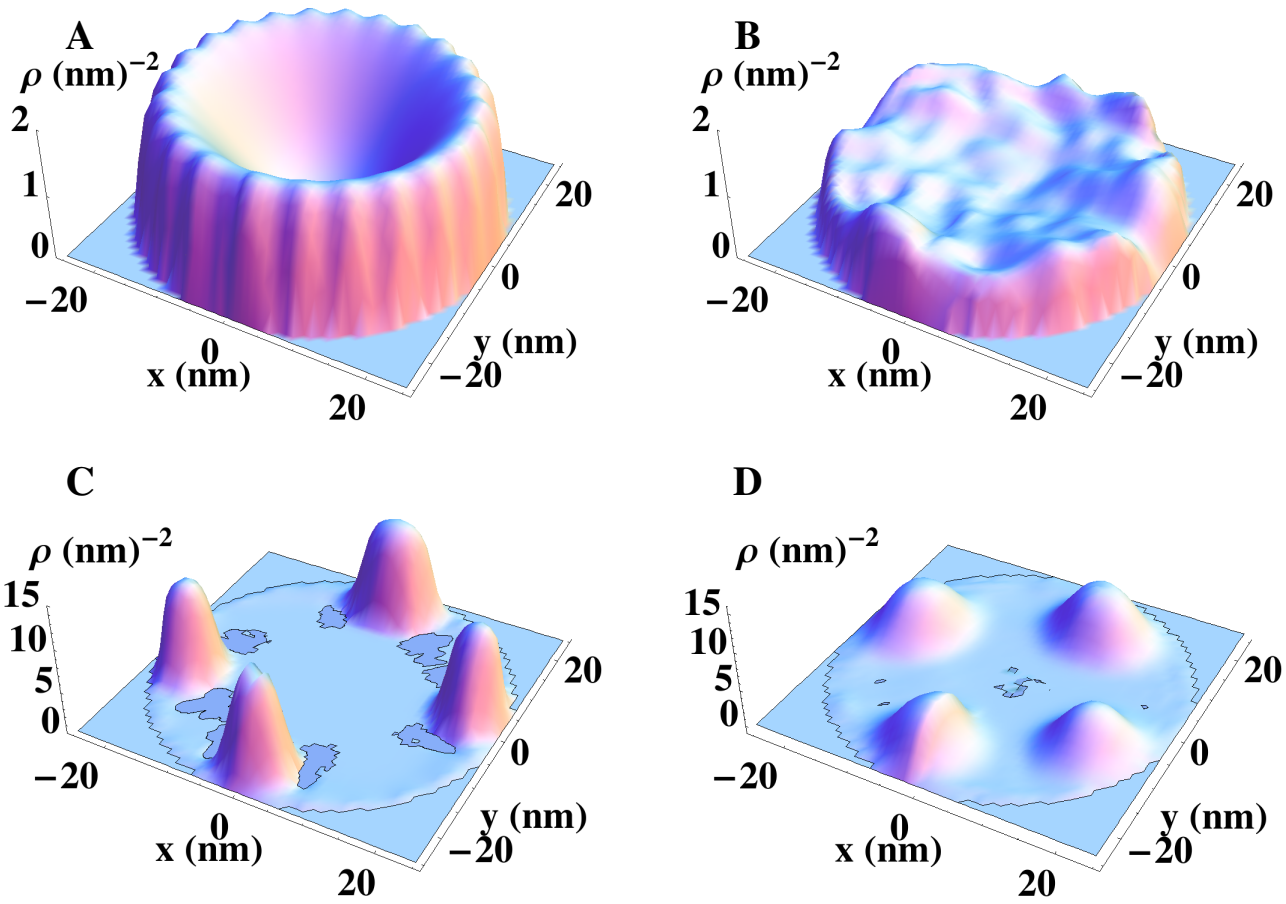

Figure 4.4: Equilibrium densities of polymer disks inside a circle of 25nm for density functional theory and Monte Carlo, for $\epsilon = 0.01 k_b T$ and $\lambda = 0.75$ nm (A and B respectively) and for $\epsilon = 0.04 k_b T$ and $\lambda = 1.25$ nm (C and D respectively). Both methods yield similar results.

repeated many times to determine the phase with the lowest free energy. The central and the wall phase can both exist at the same parameter set.

The wall phase can consist of any number of clumps up to the number of polymers in the system. Despite the differing numbers of clumps, it appears that the position of the clumps reflect maximal symmetry, in the sense that when there are six clumps they appear to be positioned on the vertices of a hexagon; when there are five clumps they lie on the vertices of a pentagon and so forth. Additionally, all the clumps are similar in terms of disk density and spatial extent.

According to the analytical model described previously, the total entropy cost is, very approximately, inversely proportional to the clump number. So large numbers of clumps carry little entropic cost of formation compared to a single central clump. Again approximately, the total

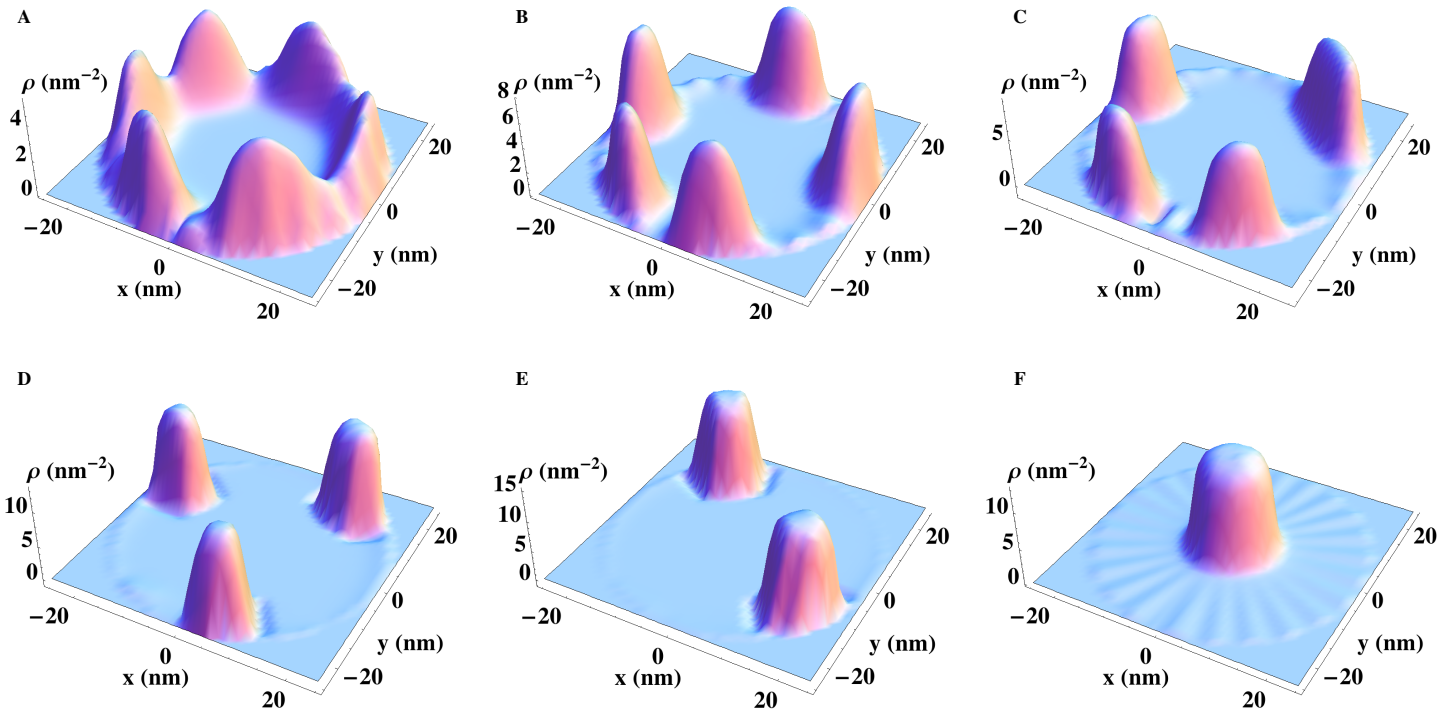

Figure 4.5: Density in a circle of radius $R = 25$ nm of 2D constrained polymers with parameters $M = 25, b = 1, N = 100, d = 0.25$ and various ϵ and λ (A) $\epsilon = 0.03, \lambda = 0.75$, (B) $\epsilon = 0.04, \lambda = 0.75$, (C) $\epsilon = 0.05, \lambda = 0.75$, (D) $\epsilon = 0.06, \lambda = 1.25$, (E) $\epsilon = 0.07, \lambda = 1.75$, (F) $\epsilon = 0.05, \lambda = 1.25$, obtained from density functional theory. There exists both the central phase (F) and various wall phases (A-E) with different numbers of clumps.

energy cost increases logarithmically with clump number (up to an asymptote). The clumping number is determined by the delicate balance between these energetic and entropic contributions to the free energy.

Using the density functional theory method we can test whether the rotational symmetry assumption has a large impact on the threshold interaction parameters the system has to choose between central and wall states. We can then investigate how the simple analytical model can describe what is occurring in the phase transition.

figure 4.6 shows the phase diagram of the polymers in terms of central/wall phases for the cases with the rotational symmetry assumption (A) and without it (B). We can see clearly that relaxing this assumption leads to a wall phase that persists over a larger range λ and ϵ. However, the overall effect is not too large, indeed a shift of around 0.25 nm in λ would lead to phase diagrams that are

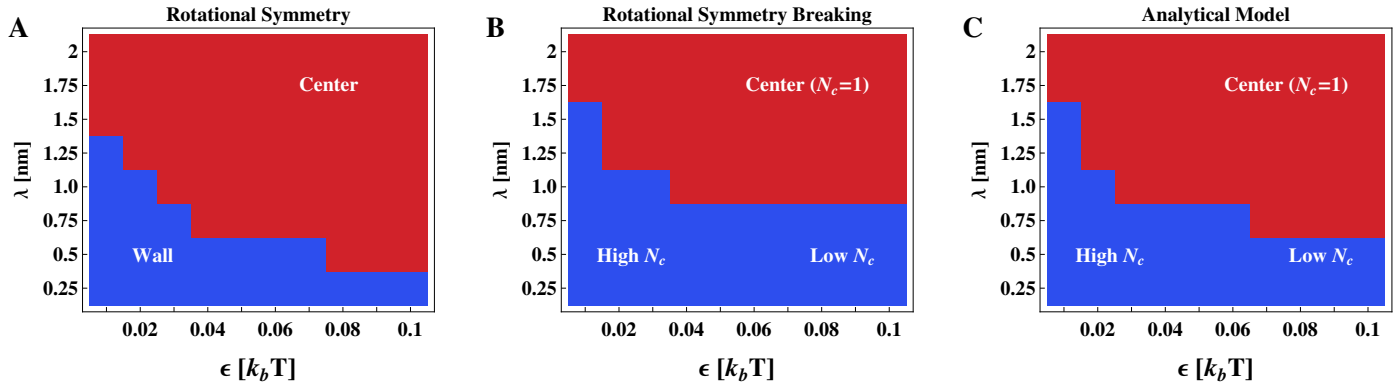

Figure 4.6: Phase diagram for 2D polymers indicating whether the polymers are more likely to be at the wall (blue) of the center (red) for different interaction parameters with A) imposed rotational symmetry assumption, B) broken rotational symmetry and C) the analytical model. These phase diagrams show quantitatively the effect of the rotational symmetry assumption on central phase stability.

very similar. The analytical model (C) captures the behaviour, despite its many simplifications.

The success of the analytical model confirms that the clumping behaviour results from a competition between the entropy of stretching the polymers against the energy penalty of creating a larger surface area. When there are large numbers of clumps, the polymers do not need to stretch very far, as the clump is likely to be close to the polymer tethering point, and therefore the entropic cost of forming more numerous clumps is lower. However, a larger number of clumps will have a greater surface area compared to fewer clumps, which will increase the energy penalty. This competition determines the equilibrium phase, and as we decrease the strength of the attraction the system will begin to favour states with more clumps. The analytical model gives a simple way of quantifying, for a particular set of parameters, how this behaviour emerges.

In this chapter we have shown that a system of polymers tethered around the circumference of a nanopore can break rotational symmetry, leading to the formation of clumps at the wall. The number of clumps can be predicted from the system parameters, such as the interaction strength and the radius of the pore. Previous theoretical results showed that tethered polymers could adopt wall or central phases, and this phase description remains valid even if the rotational symmetry assumption is dropped. When the rotational symmetry assumption is relaxed, the wall phase divides into multiple clumps which leads to a slight lowering of the free energy of the wall phase compared to the symmetric case, shrinking the boundaries of central phase stability.

This effect will be largely dependent on the parameters chosen. For instance, cylindrical pores of small radii with long polymers will likely always be completely clogged by polymer, regardless of rotational symmetry breaking. This is similar to what is to be expected in three dimensions, such that previous results obtained in three dimensions are not qualitatively altered.

We have developed a simple analytic model of the system that compares favourably with density functional theory calculations. By considering only the simplest form contributions to the free energy might take, we derived an equation that gives the change in free energy as the number of clumps is varied. This simple form of the free energy can serve to guide intuition.

In terms of the NPC, this chapter has demonstrated that the impact of rotational symmetry on the polymer profiles can have a reasonable impact, but does not lead to qualitative differences in the phase diagram. The NPC is known to have eight-fold symmetry[1]. The symmetry breaking mechanism explained in this chapter might explain this eight fold symmetry. However, this is only a speculative idea at the moment.

So far, our model has only treated the nups within the NPC. However, as mentioned in chapter 1, there are potentially many proteins other than the nups that can influence the structure of the NPC. We also demonstrated in chapter 3 that only small differences in inter-polymer interactions can lead to large changes in the polymer structure. In the next chapter we will attempt to incorporate the effect of Nuclear Transport Receptors on the NPC. This will require us to modify our functional.

Chapter 5

Modelling of Nanopores with Tethered Polymers and Free Fluid Particles

In the confinement of a cylindrical nanopore, polymer-polymer interactions have been shown in the previous chapters to yield a wide and rich pattern of possible morphologies. Particularly, in chapter 3, we have demonstrated the bi-stable collective behaviour, with the polymers switching between an open-pore state in which the polymers collapse towards their anchoring points at the pore wall ("wall phase") and, for stronger attractive interactions, a centrally condensed, closed-pore state ("central phase") [48]. The collective behaviour of such polymers yields a wide and rich pattern of possible morphologies, which is critically dependent on the interaction parameters, as has been demonstrated by numerical simulations, [48, 35, 34, 53]. For the NPC, these and other models have a major shortcoming in not incorporating the presence of NTRs in the pore, as discussed in chapter 1. Experimental data suggest the simultaneous presence of 10s if not 100 transport receptors per NPC under physiological conditions [70], which would correspond to a significant fraction of the available volume in the NPC central channel. NTRs have also been suggested as integral components of the NPC selectivity barrier [71, 72, 73]. In this chapter we therefore set out to explore the effects of NTRs on the polymeric structure in the NPC channel. This work can be compared directly to superresolution fluorescence microscopy measurements of positions of proteins within the NPC, along the lines of [74].

Thus, in this chapter we introduce NTRs into our previous polymer-only model. We measure the effects that the NTRs have on the polymer distribution. We then speculate about the physiological consequences of these results

In order to introduce NTRs into our model, we treat them as another free colloidal fluid component, we have to modify our functional to account for this extra component. The NTR we model is importin-β.

5.1 Derivation of functional

density functional theory of Simple Fluids in Confined within a Cylinder

We employ the following free energy functional for an ideal single component fluid [57]:

$$\beta\Omega_f[\rho_f(r)] = \int \rho_f(\mathbf{r})(\ln(\lambda^3\rho_f(\mathbf{r})) - 1)\,\mathrm{d}\mathbf{r} \tag{5.1}$$
$$+ \int V_f(\mathbf{r})\rho_f(\mathbf{r})\mathrm{d}\mathbf{r} - \mu\int \rho_f(\mathbf{r})\mathrm{d}\mathbf{r}$$

where ρ_f is the density of fluid particles, V_f is an external potential acting upon the particles, λ is the thermal de Broglie wavelength and μ is the chemical potential. This functional describes point-like particles interacting with an external potential. In order to model the particles as hard spheres we shall proceed using the approach proposed by Rosenfeld [75]. Compared to our previous chapters, where we modelled the hard sphere terms using the Carnahan-Starling term, this new non-local functional description of the hard sphere terms is necessary in order to account for the manner in which we are modelling the importins. The Rosenfeld functional makes use of six weighted densities, which are convolutions of the fluid density with respect to different weight functions. The set of weight densities, for a general mixture of fluids with N_c components, $\{n_\alpha\}$ are given by [76]:

$$n_\alpha(\mathbf{r}) = \sum_{j=1}^{N_c} n_{\alpha j}(\mathbf{r}) = \sum_{j=1} \int \rho_j(\mathbf{r}')w_j^{(\alpha)}(\mathbf{r}-\mathbf{r}')\mathrm{d}\mathbf{r}' \tag{5.2}$$

Where j refers to the component, $\rho_j(\mathbf{r}')$ is the density at point r' of component j. The weight functions $w_j^{(\alpha)}(\mathbf{r}-\mathbf{r}')$ are given by:

$$w_j^{(2)}(\mathbf{r}-\mathbf{r}') = \delta(R_j - |\mathbf{r}-\mathbf{r}'|) \tag{5.3}$$

$$w_j^{(3)}(\mathbf{r}-\mathbf{r}') = \Theta(R_j - |\mathbf{r}-\mathbf{r}'|) \tag{5.4}$$

$$\boldsymbol{w_j^{(v2)}}(\mathbf{r}-\mathbf{r}') = \frac{\mathbf{r}-\mathbf{r}'}{|\mathbf{r}-\mathbf{r}'|}\delta(R_j - |\mathbf{r}-\mathbf{r}'|) \tag{5.5}$$

$$w_j^{(0)}(\mathbf{r}-\mathbf{r}') = \frac{w_j^{(2)}(\mathbf{r}-\mathbf{r}')}{4\pi R_j^2} \tag{5.6}$$

$$w_j^{(1)}(\mathbf{r}-\mathbf{r}') = \frac{w_j^{(2)}(\mathbf{r}-\mathbf{r}')}{4\pi R_j} \tag{5.7}$$

$$\boldsymbol{w_j^{(v1)}}(\mathbf{r}-\mathbf{r}') = \frac{\boldsymbol{w_j^{(v2)}}(\mathbf{r}-\mathbf{r}')}{4\pi R_j} \tag{5.8}$$

The details of calculating the weighted densities are given in the next section.

The excess free energy with respect to an ideal gas due to hard sphere interactions is given by:

$$\beta F_{HS} = \int \mathrm{d}\mathbf{r}\, \Phi^{HS}\left[\{n_\alpha\}\right](\mathbf{r}) \tag{5.9}$$

Where Φ^{HS} is given by:[75]:

$$\Phi^{HS}\left[\{n_\alpha\}\right] = -n_0 \ln\left(1-n_3\right) + \frac{n_1 n_2 - \mathbf{n}_{v1}.\mathbf{n}_{v2}}{1-n_3} + \frac{\frac{1}{3}n_2^3 - n_2 \mathbf{n}_{v2}.\mathbf{n}_{v2}}{8\pi(1-n_3)^2} \tag{5.10}$$

Such that the combined functional for a hard sphere fluid is:

$$\beta\Omega_F = \beta\Omega_f + \beta F_{HS} \tag{5.11}$$

We can test this functional against Monte Carlo simulations as seen in figure 5.1. We shall be studying cases where the number of particles within the pore is low, thus figure 5.2 is also plotted comparing Monte Carlo and DFT densities for low numbers of fluid particles under an external potential. This is to demonstrate the veracity of the DFT method for small numbers of fluid particles.

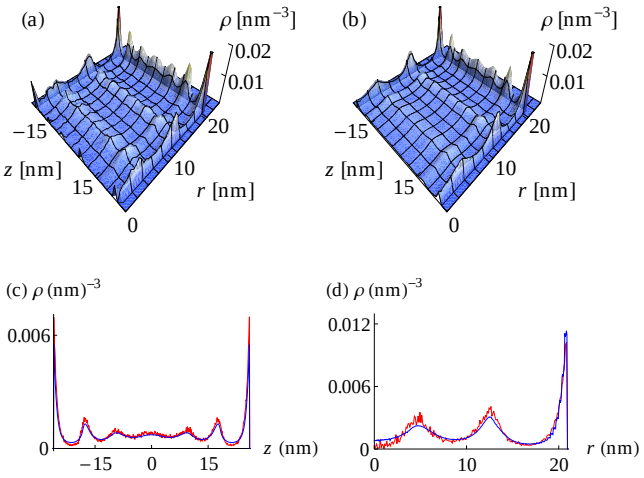

Figure 5.1: Comparison between densities for the case of 150 monomeric hard spheres of 8 nm diameter in a pore of 60 nm height and 25 nm radius. The particles have no interaction beyond the hard sphere repulsion. (a) and (b) are the full Monte Carlo and DFT densities in the r and z axes. (c) and (d) are slices along a certain axis where Monte Carlo is in Red and DFT is blue and dotted. The comparison is very good. For these tests, we closed the top and bottom of the pore, such that the fluid does not undergo number exchange.

5.2 Extension to fluid-polymer mixtures

To derive the combined functional for a mixture of polymers and fluids we use a variation of the functional defined in chapter 3:

$$\beta F_p[W(\mathbf{r})] = -M \ln Z[W(\mathbf{r})] - \int W(\mathbf{r})\rho_p(\mathbf{r})\,\mathrm{d}r + \int V_p(\mathbf{r})\rho_p(\mathbf{r})\mathrm{d}\mathbf{r} \tag{5.12}$$

For now, the contribution to the free energy of the hard spheres is being ignored. Where M is the number of polymers, $W(r)$ is the polymer mean field, and ρ_p is the density of beads making up the polymer. V_p is an external potential acting upon the polymers. $Z[W(r)]$ is the partition function of a single polymer interacting under the total potential, and is given in the same way as defined before [62]:

$$Z[W(\mathbf{r})] = \int G(\mathbf{r}_0, \mathbf{r}, N; [W])\mathrm{d}\mathbf{r} \tag{5.13}$$

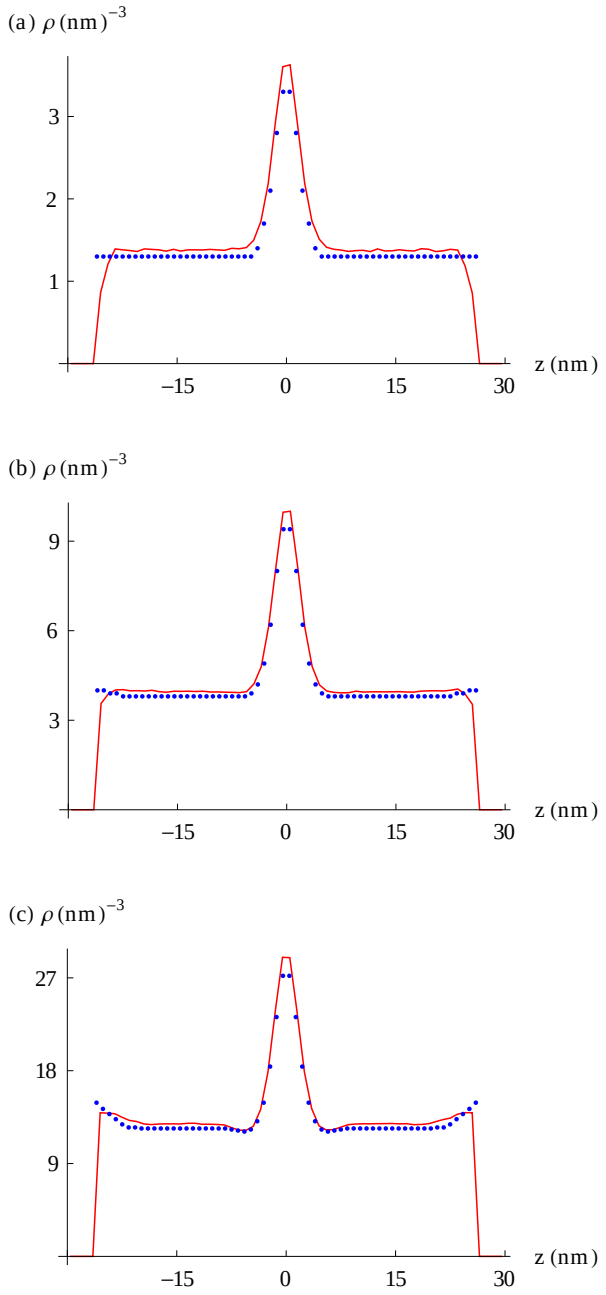

Figure 5.2: Comparison between Monte Carlo (Red) and DFT (blue, dotted) 8nm monomeric particle densities for the case of 1, 3 and 10 fluid particles respectively under a Gaussian external potential centered at $z = 0$. These figures shows that the DFT approach remains valid even for a small number of particles.

where r_0 is the tethering point of the polymer, and N is the chain length. As before, G can be found as the solution to the following partial differential equation [62]:

$$\frac{\partial G(\mathbf{r}_0, \mathbf{r}, s; [W])}{\partial s} = \left(\frac{b^2}{6} \nabla^2 - W(\mathbf{r}) \right) G(\mathbf{r}_0, \mathbf{r}, s; [W]) \tag{5.14}$$

From the function $G(\mathbf{r}_0, \mathbf{r}, s; [W])$ the density can be calculated in the following way:

$$\rho(\mathbf{r}) = \frac{\int_0^N \mathrm{d}s \int \mathrm{d}\mathbf{r}' G(\mathbf{r}_0, \mathbf{r}, N-s; [W]) G(\mathbf{r}, \mathbf{r}', s; [W])}{\int \mathrm{d}\mathbf{r}' G(\mathbf{r}_0, \mathbf{r}', N; [W])}. \tag{5.15}$$

This functional describes ideal polymers made up of point-like beads. Further details about this functional and its full derivation can be found in chapter 3. Note that the functional of the polymers, equation (5.12), is a free energy functional as the polymers do not undergo a number exchange with the bath as they are anchored to the wall of the nanopore. However, the functional of the fluid (equation 5.1) is a grand potential as the fluid is allowed to undergo number exchange with the bath. We make this explicit by using F to describe the functional of the polymers and Ω to describe the functional of the fluid.

We propose that the functional of a combined fluid-polymer system will be given by:

$$\beta\Omega = \beta F_p[W(\mathbf{r})] + \beta\Omega_f[\rho_f(r)] + \beta F_{pf}^{int}[W(r), \rho_f(r)] \tag{5.16}$$

This equation gives a semi-grand potential, as only some of the components are allowed to undergo number exchange. F_p describes point-like beads bound in a polymer, correspondingly Ω_f describes an ideal fluid. The term F_{pf}^{int} describes all the inter-particle interactions in the system. This is the excess free energy due to all the repulsive and attractive interactions within the system. It is given by:

$$\begin{aligned} F_{pf}^{int}[W(\mathbf{r}), \rho_f(\mathbf{r})] &= \iint \rho_p(\mathbf{r})\rho_f(\mathbf{r}')\phi_{pf}^l(\mathbf{r}-\mathbf{r}')\mathrm{d}\mathbf{r}\mathrm{d}\mathbf{r}' \\ &+ \int \mathrm{d}\mathbf{r} \left\{\Phi^{HS}\left[\{n_\alpha\}\right](\mathbf{r})\right\} + \left\{\Phi^{ch}\left[\{n_\alpha\}\right](\mathbf{r})\right\} \\ &+ \frac{1}{2}\iint \rho_f(\mathbf{r}')\rho_f(\mathbf{r})\phi_{ff}^l(\mathbf{r}-\mathbf{r}')\mathrm{d}\mathbf{r}'\mathrm{d}\mathbf{r} \\ &+ \frac{1}{2}\iint \rho_p(\mathbf{r})\rho_p(\mathbf{r}')\phi_{pp}^l(\mathbf{r}-\mathbf{r}')\mathrm{d}r\mathrm{d}\mathbf{r}' \end{aligned} \tag{5.17}$$

These interaction terms include the hard sphere terms of a two component fluid. In addition this, the polymers will have an additional chain-connectivity term [65, 77], that accounts for the fact that the hard spheres are joined together.

$$\Phi^{ch}\left[n_\alpha\right] = \frac{1-N}{N} n_{01}\zeta_1 \log y_{11} \tag{5.18}$$

$$y_{11} = \frac{1}{1-n_3} + \frac{n_2 R_p \zeta}{2(1-n_3)^2} + \frac{n_2^2 R_p^2 \zeta}{18(1-n_3)^3} \tag{5.19}$$

$$\zeta = 1 - \frac{\mathbf{n}_{v2}.\mathbf{n}_{v2}}{n_2^2} \tag{5.20}$$

$$\zeta_1 = 1 - \frac{\mathbf{n}_{v21}.\mathbf{n}_{v21}}{n_{21}^2} \tag{5.21}$$

Where N is the number of beads on the polymer and R_p is the polymer bead radius. We model the interaction as an infinite repulsive hard sphere interaction and a longer range attractive tail. We use the following form of the pairwise interaction between a particle of type i and another particle of type j :

$$\phi_{ij}^{l}(\mathbf{r}) = \begin{cases} 0 & |\mathbf{r}| < R_i + R_j \\ -\epsilon_{ij} \exp(-(|\mathbf{r}| - (R_i + R_j))/\lambda_{ab}) & |\mathbf{r}| \geq R_i + R_j \end{cases} \tag{5.22}$$

ϵ_{ij} is a measure of the 'strength' of the interaction between particles of type i and j, λ specifies the decay range of the interaction, R_i and R_j are the hard sphere radii of the particle types i and j. This interaction is chosen to represent hydrophobic interactions [37]. In reality, the system we are attempting to model has an infinite repulsive energy when $|\mathbf{r}| < R_i + R_j$, however, for numerical reasons the infinite part of the potential is set to 0 and the finite size of the particles is modelled using a hard sphere term, which gives an excess free energy due to hard sphere diameter as a functional of the density. This is a more accurate way of representing singular potentials.

This functional is minimised over the density and polymer mean field in order to gain equilibrium density profiles and free energies.

5.3 Derivation of cylindrical weight functions

FMT weight functions in cylindrical geometry have been calculated before by Malijevsky [78] and Mariani et al [79]. The derivations are reproduced here, with the additional detail that we are working in both the axial and radial dimensions. The weight functions are given by:

$$w_j^{(2)}(\mathbf{r} - \mathbf{r}') = \delta(R_j - |\mathbf{r} - \mathbf{r}'|) \tag{5.23}$$

$$w_j^{(3)}(\mathbf{r} - \mathbf{r}') = \Theta(R_j - |\mathbf{r} - \mathbf{r}'|) \tag{5.24}$$

$$\boldsymbol{w_j^{(v2)}}(\mathbf{r} - \mathbf{r}') = \frac{\mathbf{r} - \mathbf{r}'}{|\mathbf{r} - \mathbf{r}'|} \delta(R_j - |\mathbf{r} - \mathbf{r}'|) \tag{5.25}$$

$$w_j^{(0)}(\mathbf{r} - \mathbf{r}') = \frac{w_j^{(2)}(\mathbf{r} - \mathbf{r}')}{4\pi R_j^2} \tag{5.26}$$

$$w_j^{(1)}(\mathbf{r} - \mathbf{r}') = \frac{w_j^{(2)}(\mathbf{r} - \mathbf{r}')}{4\pi R_j} \tag{5.27}$$

$$\boldsymbol{w_j^{(v1)}}(\mathbf{r} - \mathbf{r}') = \frac{\boldsymbol{w_j^{(v2)}}(\mathbf{r} - \mathbf{r}')}{4\pi R_j} \tag{5.28}$$

We wish to apply these weighted densities to a mixture of polymers and fluids within a cylindrical channel. The integrals can be understood physically in the following way: The n_3 weighted density is a volume integral of the density within the interior of a sphere, and the n_2 is the integrated surface density of the sphere, $\mathbf{n_2}$ is the vector surface area. All other weighted densities are the same to within a constant factor that depends on the radius of the sphere. As stated before, we assume that the density within the pore has azimuthal symmetry. n_3 is given by:

$$n_3(\mathbf{r}) = \int \mathrm{d}\mathbf{r}'\rho(\mathbf{r}')\Theta(R_j - |\mathbf{r} - \mathbf{r}'|) \tag{5.29}$$

Rewriting this in cylindrical coordinates and using the azimuthal independence of the pore gives:

$$w_m(r, r', z, z') = \tag{5.30}$$
$$\int_0^{2\pi} \mathrm{d}\beta\, \Theta\Big(R_j - \big[r^2 + r'^2 - 2rr'\cos(\beta) + (z - z')^2\big]^{\frac{1}{2}}\Big)$$

$$n_3(r, z) = \iint r'\mathrm{d}r'\mathrm{d}z'\rho(r', z')w_m(r, r', z, z') \tag{5.31}$$

Where β is the angle between the two vectors $\mathbf{r}$ and $\mathbf{r'}$. The integral can be evaluated analytically:

$$w_m(r, r', z, z') = 2\pi - 2\arccos\left(\frac{R_j^2 - r^2 - r'^2 - (z - z')^2}{2rr'}\right) \tag{5.32}$$

and combining the previous two equations gives us an integral for the weighted density n_3

$$n_3(r, z) = \iint 2r'(\pi - \arccos\left(\frac{R_j^2 - r^2 - r'^2 - (z - z')^2}{2rr'}\right)) \tag{5.33}$$
$$\rho(r', z')\mathrm{d}r'\mathrm{d}z$$

In order to work out the integral for n_2 we use the general relation for a surface integral:

$$\int_S f\, dS = \iint_T f(\mathbf{x}(r, z)) \left|\frac{\partial \mathbf{x}}{\partial r} \times \frac{\partial \mathbf{x}}{\partial z}\right| dr\, dz \tag{5.34}$$

Where the vector $\mathbf{x}$ is some parametrization of the surface, $f(\mathbf{x}(\mathbf{r}, \mathbf{z}))$ is some function (in our case this will be ρ). In order for $|r - r'|$ to be on the surface the following relation must hold:

$$r^2 + r'^2 + (z - z')^2 + 2rr'cos(\beta) = R^2 \tag{5.35}$$

I.e the distance between the two vectors is equal to the radius of the sphere. We can rearrange this equation to give:

$$\beta = \arccos\left(\frac{R^2 - r^2 - r'^2 - (z - z')^2}{2rr'}\right) \tag{5.36}$$

A general position vector, lying on the surface of the sphere centred at (r, z), in cylindrical coordinates is then given by:

$$\mathbf{x} = (r' \cos\beta, r' \sin\beta, z') \tag{5.37}$$

Using this allows us to calculate the individual elements in the surface integral (5.34)

$$\frac{\partial \mathbf{x}}{\partial r} = (\frac{-r'}{r}, \frac{r'}{r}\frac{r^2 - r'^2 + R^2 - (z-z')^2}{a}, 0) \tag{5.38}$$

$$\frac{\partial \mathbf{x}}{\partial z} = (\frac{z-z'}{r}, \frac{(z'-z)\left(R^2 - r^2 - r'^2 - (z-z')^2\right)}{ra}, 1) \tag{5.39}$$

with

$$a = \left(\left[R^2 - (r-r')^2 - (z-z')^2\right]\left[(r'+r)^2 - R^2 + (z-z')^2\right]\right)^{\frac{1}{2}} \tag{5.40}$$

Where we have defined the parameter a for simplicity due to the fact that it appears in a lot of places. This then allows us to calculate n_2:

$$\begin{aligned} n_2 &= \int_{\text{Sphere}} \rho \mathrm{d}S \\ &= \int_{\text{Max}(0,r-R)}^{r+R} \mathrm{d}r' \int_{z-\sqrt{R^2-(r-r')^2}}^{z+\sqrt{R^2-(r-r')^2}} \mathrm{d}z' \rho(r', z') \frac{r'}{a} \end{aligned} \tag{5.41}$$

Using the previous vector $\mathbf{x}$ also allows us to calculate the vector weighted density components, in the r and the z directions (we assume azimuthal symmetry), these are given by:

$$\mathbf{n}_2(\mathbf{r}) = \int f(\mathbf{x}(r,z)) \frac{\partial \mathbf{x}}{\partial r} \times \frac{\partial \mathbf{x}}{\partial z} dr\, dz \tag{5.42}$$

Therefore:

$$\mathbf{n}_2^r(r, r', z, z') = \int \mathrm{d}r' \mathrm{d}z' \rho(r', z') 2 \frac{r'}{r} \frac{r'^2 + (z-z')^2 - r^2 - R^2}{a} \tag{5.43}$$

$$\mathbf{n}_2^z(r, r', z, z') = \int \mathrm{d}r' \mathrm{d}z' \rho(r', z') \frac{4(z-z')r'}{a} \tag{5.44}$$

All the integrals for the weight functions are the same as the integrals defined above multiplied by some constant related to the sphere radius.

5.4 Numerical details of integration

There are two different methods we may use for the calculation of the weighting functions. one uses a hybrid method involving both Fourier transforms and real space integrals. We first note

that the form of all the weight functions is:

$$n_\alpha(r,z) = \int \rho(r',z')W(r,r',z-z')\mathrm{d}r'\mathrm{d}z' \tag{5.45}$$

I.e the integrals are all convolutions in the z dimension. This suggests the following scheme for their evaluation:

$$n_\alpha(r,z) = \int \mathrm{d}r' FT^{-1}\{FT\{\rho(r',z')\}FT\{W(r,r',z')\}\} \tag{5.46}$$

where FT is the Fourier transform $FTf(z') = \int f(z')\exp(ikz')$ and FT^{-1} is the inverse Fourier transform.

The other method is a straightforward numerical integration of the weighting equations involving double integrals over the r' and z' coordinates. Standard methods of quadrature may be used, however all weight functions other than w_3 contain square root singularities along the integration range. There are also special considerations to be made when $r = 0$.

r=0

When $r = 0$, we can make use of residue theorem to reduce the integrals to 1D integrals. At $r = 0$, $\mathbf{n}_2^r$ is equal to 0. The other weight functions are:

$$\mathbf{n}_2^z = 2\pi\int_0^R r'\Big[\rho\Big(r', z-(R^2-r'^2)^{\frac{1}{2}}\Big) - \rho\Big(r', z-(R^2-r'^2)^{\frac{1}{2}}\Big)\Big]\ \mathrm{d}r' \tag{5.47}$$

$$n_2 = 2\pi R\int_0^R \frac{r'}{\sqrt{R^2-r'^2}}\Big(\rho(r', z-\sqrt{R^2-r'^2}) \tag{5.48}$$
$$+\ \rho(r', z+\sqrt{R^2-r'^2})\Big)\,\mathrm{d}r'$$

$$n_3 = 2\pi\iint \rho(r',z')r'\,\mathrm{d}r'\mathrm{d}z' \tag{5.49}$$

$\mathbf{r}+\mathbf{r}' < \mathbf{R}$

When $r+r' < R$ we have more singularities within the integration range. The surface integrals defined above contain square root singularities at the end points, however when $r+r' < R$ there are two additional square root singularities located at $z\pm\sqrt{R^2-(r+r')^2}$. It is therefore recommended that the integral limits are modified such that we perform 4 integrals, with the 4 singularities at the endpoints. See figure 5.3.

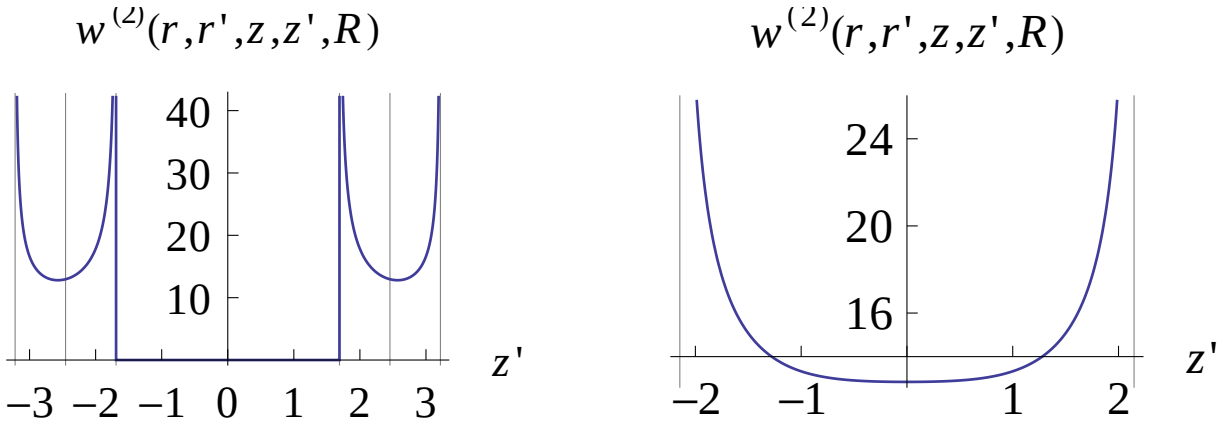

Figure 5.3: n_2 weight function for given R,z,r' and r as z' is varied. The left hand diagram shows the function when $r' + r < R$ and the right hand diagram shows the function when $r' + r > R$. When $r' + r < R$ there are four square root singularities within the integration range, which need to be treated with caution in order to obtain accurate results of the integral.

5.5 Iterative scheme

Here we show the derivation of the DFT equations. We take as the starting point the semi-grand potential:

$$\begin{aligned}
\beta\Omega = &-M \log Z_p[W(\mathbf{r})] - \int W(\mathbf{r})\rho_p(\mathbf{r})\,\mathrm{d}\mathbf{r} \\
&+ \int \mathrm{d}\mathbf{r}\,\left(\Phi^{HS}\left[n_\alpha\right] + \Phi^{ch}\left[n_\alpha\right]\right) \\
&+ \frac{1}{2}\int \rho_p(\mathbf{r})\rho_p(\mathbf{r})\phi^l_{pp}(\mathbf{r}-\mathbf{r}')\mathrm{d}\mathbf{r}\mathrm{d}\mathbf{r}' \\
&+ \int \rho_f(\mathbf{r})(\log(\lambda^3\rho_f(\mathbf{r})) - 1)\,\mathrm{d}\mathbf{r} \\
&+ \int \rho_f(\mathbf{r})\rho_p(\mathbf{r}')\phi^l_{fp}(\mathbf{r}-\mathbf{r}')\,\mathrm{d}\mathbf{r}\mathrm{d}\mathbf{r}' \\
&+ \frac{1}{2}\int \rho_f(\mathbf{r})\rho_f(\mathbf{r}')\phi^l_{ff}(\mathbf{r}-\mathbf{r}')\,\mathrm{d}\mathbf{r}\mathrm{d}\mathbf{r}' - \mu\int \rho_f(\mathbf{r})\,\mathrm{d}\mathbf{r} \\
&+ \int V_{\mathrm{P}ext}(\mathbf{r})\rho_p(\mathbf{r})\,\mathrm{d}\mathbf{r} + \int V_{\mathrm{F}ext}(\mathbf{r})\rho_f(\mathbf{r})\,\mathrm{d}\mathbf{r}
\end{aligned}$$

The equilibrium state is defined by minimizing the grand potential with respect to the fluid density and polymer mean field W but the latter is equivalent to minimizing the free energy with respect

to the polymer profile, as shown in chapter 3.

$$\frac{\delta\beta\Omega}{\delta W(r)} = \int \mathrm{d}r\Bigg(- W(r) + c_p(r) + \int \rho_f(r')\phi_{pf}(r-r')\mathrm{d}r' + \int \rho_p[W(r')]\phi_{pp}(r-r')\mathrm{d}r'\Bigg)\frac{\delta\rho[W(r)]}{\delta W(y)} = 0 \tag{5.50}$$

and

$$\begin{aligned}\frac{\delta\beta\Omega}{\delta\rho_f(r)} &= c_f(r) + \log\left(\lambda^3\rho_f\right) + \int \rho_p(r')\phi_{pf}(r-r')\mathrm{d}r' \\ &+ \int \rho_f(r')\phi_{ff}(r-r')\mathrm{d}r' - \mu = 0\end{aligned} \tag{5.51}$$

Where $c_i(r) = \frac{\delta}{\delta\rho_i(r)}\int \mathrm{d}\mathbf{r}\,\left(\Phi^{HS}\left[n_\alpha(\mathbf{r})\right] + \Phi^{ch}\left[n_\alpha(\mathbf{r})\right]\right)$ and i refers to the species under consideration. We split μ into ideal and excess parts:

$$\mu = -\log\left(\frac{1}{\lambda^3\rho_{fb}}\right) + \mu_{ex} \tag{5.52}$$

Where ρ_{fb} is the bulk density of the fluid. This leaves:

$$\begin{aligned}\log\left(\lambda^3\rho_f\right) &= \mu_{ex} + \log\left(\lambda^3\rho_{fb}\right) - c_f(r) - \int \rho_p(r')\phi_{pf}(r-r')\mathrm{d}r' \\ &- \int \rho_f(r')\phi_{ff}(r-r')\mathrm{d}r'\end{aligned} \tag{5.53}$$

$$\begin{aligned}\rho_f(r) = \rho_{fb}\exp\Bigg[&\mu_{exc} - c_f(r) - \int \rho_p(r')\phi_{pf}(r-r')\mathrm{d}r' \\ &- \int \rho_f(r')\phi_{ff}(r-r')\mathrm{d}r'\Bigg]\end{aligned} \tag{5.54}$$

as the equation which minimises the functional over the fluid density, and the corresponding equation over the polymer density is given by:

$$W(r) = c_p(r) + \int \rho_f(r')\phi_{pf}(r-r')\mathrm{d}r' + \int \rho_p[W(r')]\phi_{pp}(r-r')\mathrm{d}r' \tag{5.55}$$

In order to solve these equation we introduce a fictitious time variable into the equations, leaving us with a pair of simultaneous differential equations:

$$\begin{aligned}\frac{\partial\rho_f(r)}{\partial t} &= -\rho_f(r) + \rho_{fb}\exp\Bigg[\mu_{exc} - c_f(r) \\ &- \int \rho_p(r')\phi_{pf}(r-r')\mathrm{d}r' - \int \rho_f(r')\phi_{ff}(r-r')\mathrm{d}r'\Bigg]\end{aligned} \tag{5.56}$$

$$\begin{aligned}\frac{\partial W(r)}{\partial t} &= -W(r) + c_p(r) + \int \rho_f(r')\phi_{pf}(r-r')\mathrm{d}r' \\ &+ \int \rho_p[W(r')]\phi_{pp}(r-r')\mathrm{d}r'\end{aligned} \tag{5.57}$$

Using the numerical representation of the derivative we can write these equations in terms of update rules. Starting with an initial guess of $W(r)$ and $\rho_f(r)$ we can then iterate onwards until the solution is no longer changing.

$$\begin{aligned}\rho_f^{n+1}(r) &= (1-\Delta t)\rho_f^n(r) + \Delta t \rho_{fb} \exp\Bigg[\mu_{exc} - c_f(r) \\ &- \int \rho_p^n(r')\phi_{pf}(r-r')\mathrm{d}r' - \int \rho_f^n(r')\phi_{ff}(r-r')\mathrm{d}r'\Bigg] \qquad (5.58)\\ w^{n+1}(r) &= (1-\Delta t)w^n(r) + \Delta t\Bigg(c_p(r) + \int \rho_f(r')\phi_{pf}(r-r')\mathrm{d}r' \\ &+ \int \rho_p[W(r')]\phi_{pp}(r-r')\mathrm{d}r'\Bigg) \qquad (5.59)\end{aligned}$$

5.6 Interaction terms

The independence of the density on the angle means that we have many terms of the following form to evaluate:

$$\iiint \rho(r',z')\phi(r,r',z,z',\theta,\theta')r'\mathrm{d}r'\mathrm{d}\theta'\mathrm{d}z' \qquad (5.60)$$

where the dependence of ρ on θ' has been suppressed due to the angular independence assumption stated earlier. Rearranging then gives us the following integral.

$$\iint r'\mathrm{d}r'\mathrm{d}z'\rho(r',z')\int \mathrm{d}\theta'\phi(r,r',z,z',\theta') \qquad (5.61)$$

As all choices of *theta* will lead to the same results, we choose $\theta = 0$. The difficulty therefore lies with the function:

$$\phi_m(r,r',z,z') = \int_{-\pi}^{\pi} \mathrm{d}\theta'\phi(r,r',z,z',\theta') \qquad (5.62)$$

For the pair potential defined in equation (5.22). This integral is not analytically solvable. It is best to solve all these integrals numerically at the start of the iteration. However for a 426×1024 grid defined before, storing the value of this integral at every discrete (r,r',z,z') point in the calculation would lead to the necessary storage for such a calculation is massive. However by substitution of variables one may arrive at an equivalent expression:

$$\phi_m(r,r',z,z') = \exp(\sqrt{q}) \int_{\pi-\arccos(\frac{q}{gc^2}-\frac{1}{g})}^{\pi+\arccos(\frac{q}{gc^2}-\frac{1}{g})} \exp(-c\sqrt{1-g\cos(x)})\mathrm{d}x \qquad (5.63)$$

where the parameters are:

$$q = \frac{d^2}{\lambda^2} \tag{5.64}$$

$$c = \frac{\sqrt{r^2 + r'^2 + (z - z')^2}}{\lambda} \tag{5.65}$$

$$g = \frac{2rr'}{r^2 + r'^2 + (z - z')^2} \tag{5.66}$$

For any given problem there will only be 3 values of q to consider, and g cannot exceed 1 or be less than 0. Thus one only needs to solve this integral a few thousand times and interpolate the results in order to find the value at any (r, r', z, z')

5.7 Theoretical polymer-colloidal fluid structures

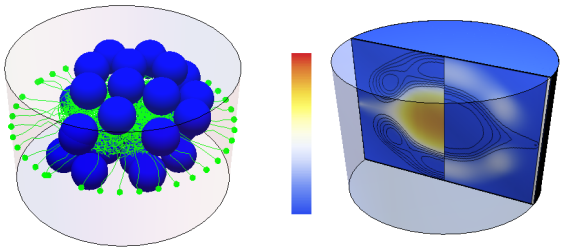

Figure 5.4: Left: Snapshot of a Monte Carlo simulation of 40 polymers of 100 beads each tethered around the circumference of a nanopore, in the presence of free and globular macromolecules (blue spheres). Right: Packing fraction (n_3 weighted density), resulting from a DFT calculation of the same system, in which azimuthal symmetry has been assumed. On either side of a vertical plane of symmetry, it represents the proportion of the space that is filled by, respectively, polymers and spheres.

The studied system consists of 40 polymers, treated as identical beads on a chain and anchored to a ring inside a open-ended, hollow and impermeable cylinder, in the presence of a colloidal fluid of large spheres to represent globular macromolecules (Figure 5.4). Classical density functional theory is used to calculate polymer and fluid densities, and the densities are assumed to be rotationally symmetric around the central axis of the pore. It is similar to the work in our previous chapter, but extended by the application of Fundamental Measure Theory (FMT) [76] to accurately describe the density of finite-sized hard spheres. It includes hard-sphere (excluded-volume) and polymer

entanglement effects, as well as attractive interactions of strengths, ϵ_{pp}, ϵ_{pc} and ϵ_{cc} for the polymer-polymer, polymer-colloidal and colloid-colloid densities, respectively. Parameters here are chosen to emulate the NPC; they can be easily adjusted, however, to represent any artificial nanopore device. The range λ for the attractive interactions is set to be 1 nm and $\epsilon_{cc} = 0$, i.e there is no condensation of the fluid in absence of the polymers. As before, the pore diameter is set to 50nm, the polymers are defined by a contour length of 100 nm, a Kuhn (segment) length identical to the bead diameter 1 nm, and the fluid by spheres of 8 nm diameter (the unhydrated diameter of nuclear transport receptors) [80]. An excess chemical potential is referenced with respect to the chemical potential ($\mu_{ex} = 0$) that yields a fluid bulk density of $6 \times 10^{-6} nm^{-3}$, i.e., $10\mu M$, the approximate concentration of nuclear transport receptors in the cytoplasm [81]. An excess chemical potential $\mu_{ex} = \pm 2$ corresponds to an approximately 10-fold increase/decrease of the bulk concentration.

We represent the polymer/colloid densities on a vertical cross-section through the pore as illustrated in figure 5.4. We subdivide this cross-section into two sides through the $r = 0$ axis of symmetry. On the left hand side we plot the packing fraction of the polymers on a false colour scale, overlaid with a contour map of the colloidal particle packing fraction. On the right hand side we plot the packing fraction of the colloidal particles and overlay a contour map of the polymer packing fraction. The false colour scale in all plots is unitless and is fixed to range from 0 to 1. All the plots are reproduced in the supplementary information on colour scales that are optimised for each panel to emphasize the approximate positions of the components.

As in our previous calculations, we find that tethered polymers have multiple phases when the colloidal particle density is small (see top panels of figure 5.5 and figure 5.6). Broadly, one can categorise the resulting polymer density as either a "wall" phase, where the majority of polymers are near their tethering point at the wall, or a "central" phase where the polymers stretch away from their anchoring point to meet in the centre of the cylinder. Depending on the parameters, only one of these two phases is stable, while the other can exist as a metastable solution of the system. The central phase becomes more stable on increasing the inter-polymer interaction. If the attraction is not strong enough, the wall phase will be favoured. There is a cross-over in the free energies of the central phase and the wall phase. This crossover can be understood from the balance between, on one hand, the energetic cost of keeping interacting polymers apart, and on the other hand, the entropic cost of stretching the polymers towards the centre. Provided that the interaction strength is strong enough, the entropic cost of the stretching the polymers can

be compensated by the resulting gain in binding energy. For this work, we have chosen a range of inter-polymer interaction strengths that are physiologically relevant, which coincides with the range where the polymers are near to this wall/central phase boundary, where we also anticipate the most interesting physical and eventually technological behaviour to occur.

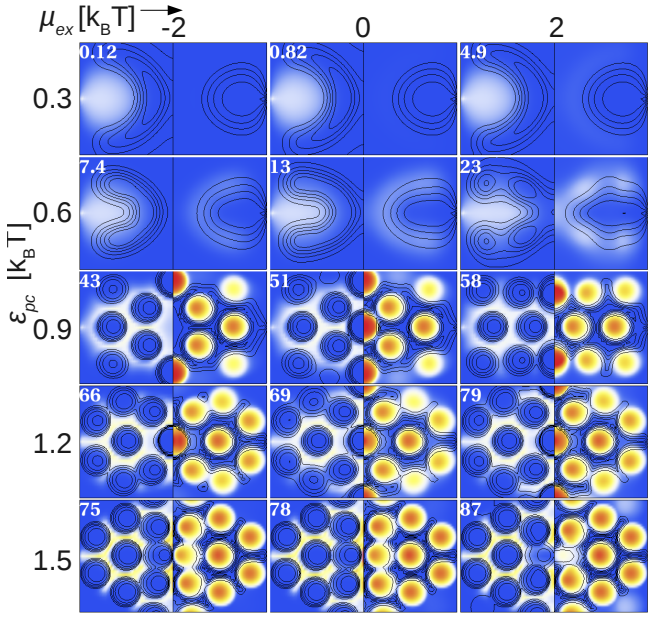

Figure 5.5: n_3 plots demonstrating the effect of changing the external chemical potential μ_{ex} and the interaction potential between the polymer and the fluid ϵ_{pc} on the collective structure. In this case $\epsilon_{pp} = 0.05$. The fluid can have a significant impact upon the polymer structure. The results shown are the minimum free energy solutions that were found.

figure 5.5 and figure 5.6 give an overview of the effect of the colloidal particles on the polymer distribution for polymer/polymer interactions (ϵ_{pp}) that, in the absence of colloidal particles, yield wall and central phases, respectively. Several general features of the polymer/colloid distributions can be observed. As expected, the pores become more filled on increasing the polymer/colloid attraction or increasing the bulk concentration of the colloidal particles. This is apparent from the increasing number of colloidal particles in the pore as well as from the colour maps (where blue corresponds to zero packing fraction).

In addition, stronger polymer/colloid attraction cause greater localization of the colloidal particles at certain favoured positions, as visible for $\epsilon_{pc} \gtrapprox 0.6$ $k_B T$ in figure 5.5 and figure 5.6. When the attraction between the colloidal particles and the polymers is strong enough relative to the

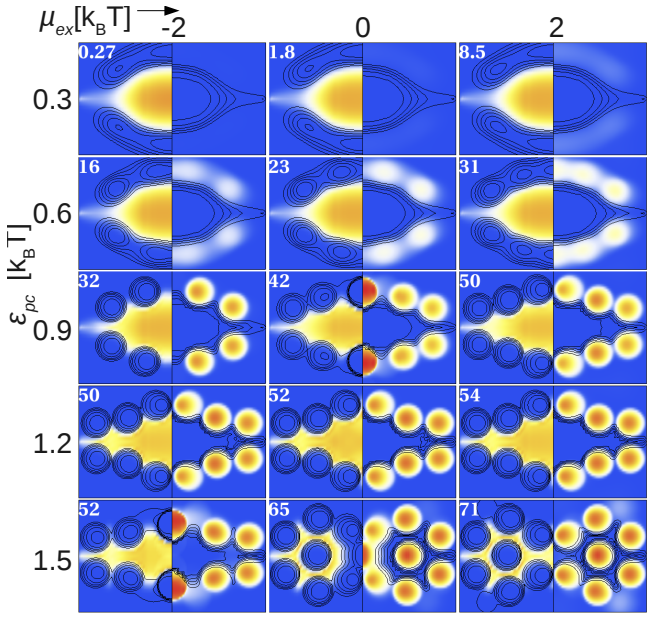

Figure 5.6: Demonstration of the effect of transport receptors for $\epsilon_{pp} = 0.10$ for various external chemical potentials μ_{ex} and the interaction potentials between the polymer and the fluid ϵ_{pc}. These plots show the how the collective structure is changed.

interpolymer attraction, it is thermodynamically favourable to form a quasi-lattice structure. Different kinds of packing are observed, where the colloidal particles can be arranged into pentagonal or hexagonal structures. The spaces between the colloidal particles are filled with polymers, which act as a glue that holds the colloidal particles together. As the colloidal particles have no attraction with one another, they are held in the lattice only by their attraction to the polymers. This is analogous to metallic bonding, where positive metal ions are held in a regular structure through their attraction to a sea of (negatively charged) electrons. It should be stressed that these structures are the equilibrium, minimum free energy solutions. In reality, dynamic phenomena, such as polymer entanglement, might frustrate the formation of these phases, possibly leading to non-equilibrium, amorphous glassy states.

For $\epsilon_{pc} > 1.5$ k$_B T$ density of the colloidal particles increasingly resembles a collection of delta functions centred at a few very specific positions. In practice, this leads to increasing numerical inaccuracies and corresponding difficulties in converging to the minimum free energy solutions. Hence, we have here restricted our observations and conclusions to $\epsilon_{pc} \leq 1.5$ k$_B T$ here, noting that for stronger polymer/colloid interactions the general trends appear to continue: accumulation of

colloidal particles at sharply defined positions in a lattice.

A consistent feature of all the calculations is the low polymer/colloid miscibility. Regions where there is a large packing fraction of polymers are unlikely to have a significant packing fraction of colloidal particles and *vice versa*. It is entropically unfavourable for polymers and large molecules to mix due to the large reduction in possible conformations of a tethered polymer when there is a large particle near it. Colloids and polymers have poor miscibility in general [37], until the polymer/colloid interactions are strong enough to overcome the entropic costs of inter-sparsing polymers with finite-size colloidal particles. Not surprisingly, this transition occurs more readily ($\epsilon_{pc} \gtrapprox 0.9\ \mathrm{k_B}T$, figure 5.5) for weaker polymer/polymer interactions than for the stronger polymer/polymer interactions that — in absence of colloidal particles — yield a central polymer condensate for low polymer/colloid interactions (in which case the transition occurs at $\epsilon_{pc} \gtrapprox 1.5\ \mathrm{k_B}T$, figure 5.6).

We observe a few other effects that are more specifically dependent on the inter-polymer attraction strength. In figure 5.5 the strength of this attraction is such that in the absence of the colloidal particles, the polymers are in a wall phase, leaving an aperture along the central axis of the channel. The addition of the colloidal particles initially ($\epsilon_{pc} = 0.6\ \mathrm{k_B}T$) leads to a moderate blocking ("clogging") of the central aperture by the colloidal particles, until, for $\epsilon_{pc} \gtrapprox 0.9\ \mathrm{k_B}T$ the earlier mentioned polymer/colloid lattice is formed, completely blocking the pore.

When the inter-polymer attractions are strong enough to form a central phase, as in figure 5.6, the colloidal particles have more difficulty in penetrating into the polymer network. Nevertheless, the colloidal particles still become increasingly localised with increasing polymer/colloid attraction, but only on the surface of the polymer condensate. Once the polymer/colloid attraction is strong enough then the familiar lattice formation is observed.

In figure 5.7 we illustrate that the system can, for identical parameter settings, converge to different states. Some of these states will be metastable. The relative stability of these phases can be tuned via the polymer/colloid interaction. In the case for $\epsilon_{pp} = 0.07$ we see a crossover in the free energies of the centrally condensed state and the wall condensed state, where the centrally condensed state becomes more stable. In the complete absence of colloidal particles (the bulk density of the colloidal particles being zero) the wall phase is favoured. The addition of colloidal particles of a certain attraction to the polymers will make the central state favoured. They cause the pore to switch from an open to a closed state.

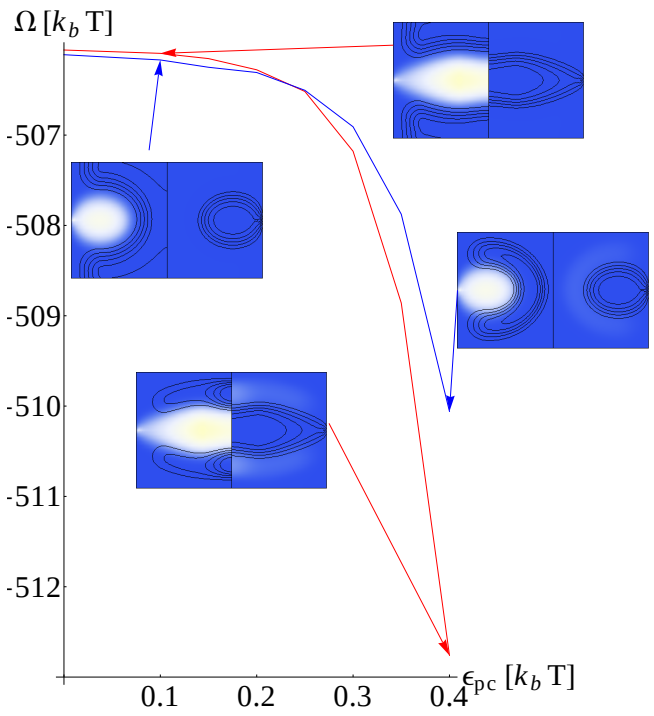

Figure 5.7: grand potential of phases within the pore for the case when $\epsilon_{pp} = 0.1$ and $\mu = -2$. The graph gives grand potentials of the different phases found within the pore, as a function of ϵ_{pc}. This shows which phase is favoured at different values of the interaction potential.

In figure 5.8 we show the grand potential of the system as the polymers and colloidal particles begin to mix to form polymer/colloid networks. There are increasingly rapid changes in the grand potential as the polymer/colloid interaction crosses the threshold necessary for the polymers and the colloidal particles to mix, at $\epsilon_{pc} \approx 0.7$, with a corresponding large increase in the number of colloidal particles found in the system.

The results thus far are summarised in figure 5.9, showing the approximate regions of stable phases against the inter-polymer and polymer/colloid interaction. We subdivide the observed phases into three rough categories: the two familiar central/wall phases described before, and a third phase where the interactions between the polymers and the colloidal particles is strong enough to form a lattice structure as can be seen at the lower parts of figure 5.5 and figure 5.6. Increasing the polymer/colloid interaction has the effect of stabilizing the central phase at the expense of the wall phase. In general, as one increases the polymer/colloid attraction, such that the ratio of the inter-polymer interaction to the polymer/colloid interactions becomes small, there will be the formation of lattice states. These phases are not homogeneous, as the colloidal particles

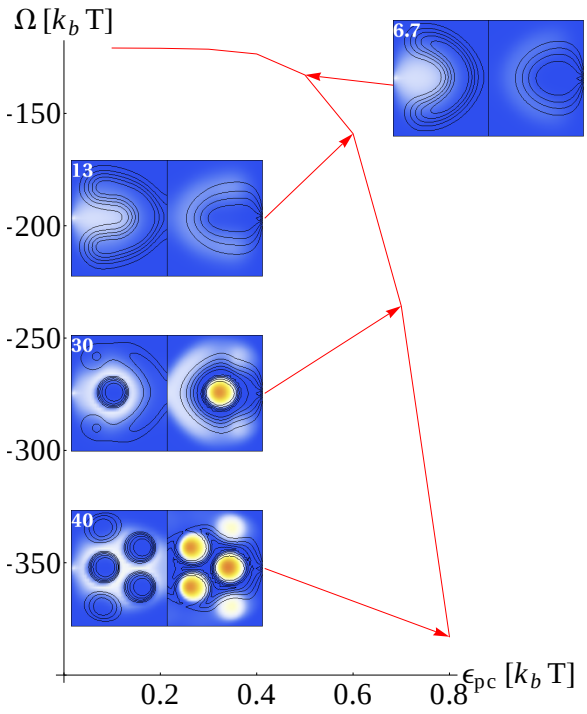

Figure 5.8: Transition of a wall state into a polymer/colloidal-particle network, plotted are the grand potentials against polymer/colloid attraction for $\epsilon_{pp} = 0.05$ and $\mu_{ex} = 0$. Large attractions between the polymers and the colloidal particles cause the formation of polymer/colloid networks.

can be arranged in differing types of lattices.

All the results thus far have been obtained with attractive interactions between the polymers and the colloidal particles. In the absence of these interactions, very few colloidal particles are found within the pore. In fact, the physiological concentration of NTRs within the cell, $10\mu M$ would correspond to less than 1 NTR within the pore if it were absent of nups.

The results thus far have been obtained for a single polymer layer in a cylindrical nanopore. Having explored the different types of behaviour for this simple model system, we next investigate if it is reproduced in a system that more closely resembles the nups in the NPC central channel. As before, we set a channel diameter to 50 nm, but tether the polymers uniformly over a range of 30 nm (centred around $z = 0$), to more closely resemble the vertebrate NPC structure[82]. The 216 nups in the channel are approximated as chains of beads with 0.76 nm diameter (consistent with twice the 0.38 nm average length per amino acid in the nups), and a total stretched length of 161 nm, the average of the contour length of the FG domains in the human NPC[83].

Trends similar to those seen previously are apparent. The more realistic treatment of the

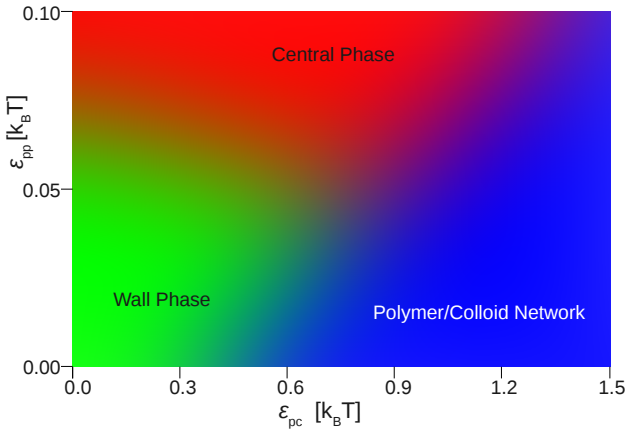

Figure 5.9: Approximate phase map of the combined polymer/colloid system at different ϵ_{pp} and ϵ_{pc}, showing the most stable phase for these different parameters at $\mu_{ex} = 0$. The wall phase is reminiscent of brush-like polymer arrangements localised at the channel wall (e.g., "virtual gate" and "reduction of dimensionality" models for the NPC); the central phase corresponds to a cohesive polymer condensate blocking the pore ("selective-phase" model for the NPC); and the polymer/colloid network emerges from our calculations for large numbers of NTRs in the NPC, as suggested by experiment.

geometry will clearly make a quantitative difference to the location of phase boundaries seen in figure 5.9, but the qualitative structure of the boundaries will remain. The increases in the number of polymers and polymer length have made the central phase more stable, despite this being offset by the decreased bond length, particle diameter and the smearing out of the polymer tethering points, which taken alone would make the wall phase more favourable. As such, the central/wall dichotomy of structures that is seen in the previous calculations still exists but is less readily apparent, as even at weak interactions the polymers will extend into the central channel. However, increasing the number of polymers appears to make intermixing between the colloidal particles and polymers less likely, the formation of "lattice" states appears to be frustrated when the polymers are attractive to one another; the colloidal particles appear to be more localised on the polymer surface. That is, when $\epsilon_{pp} = 0.05$ and $\epsilon_{pc} = 1.0$, we find a lattice state in the single polymer layer, but a centrally condensed polymer phase in figure 5.10. At low polymer/polymer affinity, lattice states are observed in figure 5.10, as the colloidal particles can more readily penetrate the polymers. The change in the tethering conditions also results in a larger number of colloidal particles in the pore.

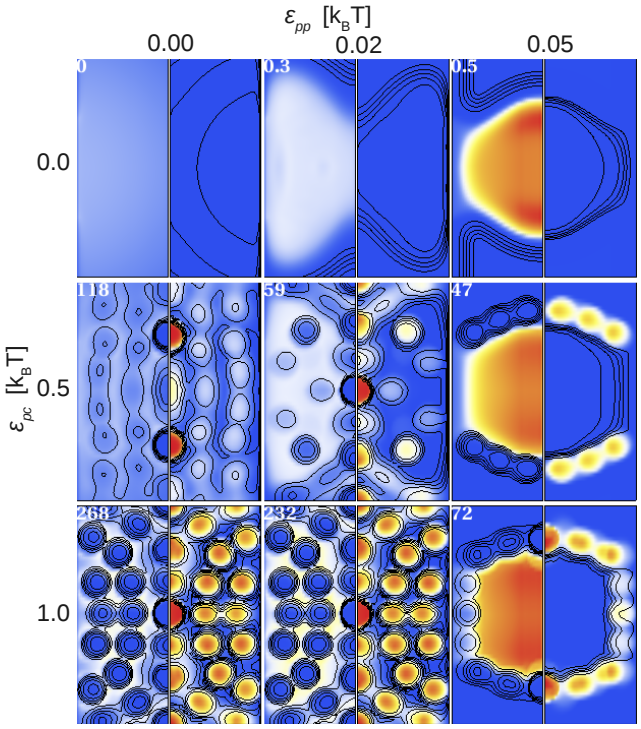

Figure 5.10: Equilibrium polymer and colloid packing fractions for a polymer tethering distribution that more closely matches the NPC structure. The results are represented by vertical cross sections of the pore for different strengths of polymer/polymer and polymer/colloid interactions. For clarity the results are displayed over twice the vertical (z) range compared to the previous figures.

We have established that a system of tethered interacting polymers in the presence of attractive spherical macromolecules can adopt a rich range of configurations inside a cylindrical pore. Much of our motivation for this study has been to determine whether biological function can be related to such physical behaviour. The selectivity of nucleocytoplasmic transport of biomolecules through the NPC is a particular feature that requires explanation, and it has been alluded to here and in chapter 3 that a pore where the polymers reside near the wall is more open for transport (less selective) than a pore where they accumulate near the axis. We have now shown, using our simplified model, that free quasispherical macromolecules affect this open or shut behaviour in a complex fashion, and that they can also penetrate a centrally condensed polymer plug to form a composite mixture with potentially distinct physical properties.

In general, we find that the presence of colloidal particles can cause a complete shift in polymer density profiles in a nanopore; that significant rearrangements of polymer/colloid configuration can be induced by a marginal changes ($\lesssim 0.1\ \mathrm{k_B}T$) in interaction strengths; and that several

metastable phases can be observed. As illustrated in Figures 2–5, the structure of polymers and colloidal particles in nanopores can be very rich. This richness can be attributed to the combined effects of confinement and complex many-particle interactions.

The here presented equilibrium structures enable us to qualitatively discuss various possible mechanisms of selective and tunable macromolecular/colloidal transport through polymer-coated nanopores. In one scenario, colloidal particles with a weak polymer-affinity will move relatively freely into an open central aperture (top of figure 5.5), while blocking the aperture for non-interacting particles. Such colloidal particles may also be used to tune the size-exclusion limit for non-interacting particles by deliberately narrowing the central aperture in the pore. In another scenario (figure 5.7), colloidal particles with weak polymer-affinity can cause the polymers to stretch across the pore, thus blocking all macromolecular transport that in the absence of these particles may be allowed. For larger polymer/colloid affinity, colloidal particles can be used to break through a polymer condensate or central phase (bottom of figure 5.6), thus facilitating transport that is otherwise inhibited along the central axis of the pore.

It is important to note that, as a consequence of the assumption that the density profiles of both polymers and colloidal particles are azimuthally symmetric, the phases here would be slightly modified if the calculations were performed in three dimensions. In chapter 4, the effect of the relaxation of the azimuthal symmetry condition was explored. The system can break the symmetry when there are attractive interactions between the polymers [84], forming distinct clumps at the wall. However, the important dichotomy of central/wall phases remains. It should be noted, of course, that the current "network" phases observed would become full lattices in three dimensions.

In the biological context of the NPC, we can identify several of the previously proposed paradigms for the transport barrier. For low nup/nup (polymer/polymer) interactions and little affinity between nups and NTRs ("wall phase" in figure 5.9), the nups will be in the wall phase and the transport barrier will be predominantly entropic in nature. [20] Such a moderate affinity between nups and NTRs will not significantly change the nups structure (top half of figure 5.5). The NTRs will not mix with the nups but will coat their surface, reducing or blocking the central aperture of the pore, discouraging unspecific transport. In such a model, the NTRs would form a key part of the selectivity barrier blocking the transport of inert molecules. However, such a model might contravene experimental evidence, as in digitonin-permeabilised cells most NTRs are washed out of the cell, yet the barrier to inert molecules is still observed to be functioning.

[85] This parameter range is also reminiscent of the reduction-of-dimensionality model, [21] which postulates that cargoes, when bound to NTRs, slide over the surface of the nups in a roughly one-dimensional random walk along the NPC central axis.

For stronger nups-nups interactions and low-to-moderate affinity between nups and NTRs ("central phase" in figure 5.9), the nups will form a condensate that stretches across the NPC channel. The barrier to transport will thus be predominantly energetic, as proposed in the selective-phase model. [13] Such a nups structure will be more resistant to penetration by NTRs (top half of figure 5.6), which will mainly be found on the surface of the nups condensate, and effectively follow a bimodal distribution as a function of vertical position in the pore, such as indeed is reported by super-resolution fluorescence microscopy for 18 nm diameter quantum dots [74] and for NTRs [73, 86]. Selective transport may be facilitated by the presence of a metastable wall phase for the nups, especially if the free energy difference between the wall and central phase is small. At present, the role of NTRs in such a rearrangement is difficult to gauge from these calculations, not least because they rather seem to promote a transition from wall to central phase, the opposite of what would be required for transport (figure 5.7).

Experiments suggest that the NPC can accommodate up to 100 NTRs, [70] which is a 3-orders-of-magnitude enhancement of the local receptor concentration in the NPC compared to that within the cell. Such large numbers of NTRs only accumulate in the pore for relatively high affinity between nups and NTRs, and appear more compatible with the central phase (figure 5.6) or the polymer/colloid networks formed when the NTRs penetrate the nups (lower parts of figure 5.5 and figure 5.6). The latter case ("polymer/colloid network" in figure 5.9) would correspond to a gel-like state as proposed in the selective-phase model, but with the NTRs playing a significant role in its cohesiveness. The NPC central channel would thus act as a potential well rather than a potential barrier for NTRs, but the free energy costs of nups rearrangement for cargo transport may be significant. It is also worth noting that, in this parameter range, the amount of NTRs in the NPC is only moderately dependent on their concentration in the surrounding liquid: $\pm 10 \sim 20\%$ for an approximately 10-fold increase/decrease in bulk concentration ($\mu_{ex} = \pm 2 k_B T$).

Taken together, these observations indicate that different proposed models for transport correspond to distinctly different behaviour of NTRs in the NPC. This is particularly interesting because recently developed super-resolution fluorescence microscopy techniques [73, 86, 74, 87, 88, 89, 90] now increasingly yield experimental access to single molecule probability distributions during trans-

port events, and in some cases to the NTR distributions [73, 86], as noted above.

Finally, our results call for caution in defining parameters for modelling any polymer-coated nanopores, since small changes in parameters can lead to significant changes in polymer behaviour, in particular in the presence of macromolecules or other colloidal particles with affinity for the polymers. In addition, the presence of well-defined metastable states implies that modelling results need to be carefully examined to establish the correct equilibrium configurations of the system. Obviously, when attempting to extrapolate our model to the NPC we have ignored various complicating biological factors, such as the chemical heterogeneity of the polymers or the exact hourglass shape of the NPC channel. A fully realistic treatment of the NPC would have to incorporate all of these aspects but would also need an accurate specification of the parameters involved; an ungainly combination of an ever-expanding phase space for the model together with difficulty in making exact predictions of biological behaviour. Whilst the quantitative nature of our results would change were we to account for full biological complexity, we expect the characteristics of the phases observed to remain similar. This is illustrated by the comparison between our minimal single polymer layer model and a polymer tethering distribution that more closely resembles the NPC: the qualitative picture — wall/central dichotomy and lattice states — remains the same despite significant changes in factors such as tethering positions and polymer lengths.

In conclusion, in this chapter we have expanded our polymers in cylinder model to include the effect of free monomeric particles. These particles are included to attempt to model the effect of NTRs on the polymer distribution. We find that these particles have a non-negligible effect on the polymer distributions we discussed in chapter 3. Indeed, small numbers of such particles can lead to substantial rearrangements of the polymers in the pore.

Having established the main physical principles behind our minimal model, we are now ready to test it against experiment. In the next chapter we show how well our model compares with various experiments performing on NPCs or NPC constituents.

Chapter 6

Comparison with Experiment and Simulations

Thus far our model has been more theoretical in nature. However, any model must be tested thoroughly against real biological experiments in order to determine the accuracy of the model. In this chapter we compare findings obtained from our theory with such experiments.

6.1 Planar polymer brushes

The multitude of intermolecular interactions present in the NPC makes modelling of the pore a formidable task. In our model, we impose the condition that all the polymers interact in the same way, which is obviously a major simplification. As the full form of all the intermolecular interactions within the pore is unknown, the "parameter space" of such a problem is huge. Attempts to model all the interactions would thus be a fruitless endeavour, as there is a large number of parameters that would have to be varied in order to gain accurate information. The large number of molecular species in the NPC also pose difficulty for any density functional theory model, as minimizing a functional over many such degrees of freedom is a daunting task. Therefore in our approach, we deal with homopolymers and map the full phase behaviour of polymers within pore. The parameters in the homopolymer model therefore measure the "average" interaction felt between the polymers. Thus it is assumed that the homopolymer model can describe a wide range of intermolecular interactions as long as the suitable interaction parameters are chosen.

There is no *a priori* way to determine these interaction parameters theoretically, so our model

needs to be compared to experimental results in order to validate our approach of representing the interaction parameters. We have done this using comparisons with both AFM measurements of real NPCs, as well as comparing our results with measurements on planar brushes of nups.

The area where our model has the greatest applicability is for the case when there is a single type of nup. Even in this system there are different types of intermolecular interactions, but each subunit of the nup is taken to interact in the same way. The work of the Richter group in San Sebastian has produced results on the systems where there is only a single kind nup[91, 92]. These nups are then end tethered to a planar surface and the thickness of the resulting films can be measured using several different experimental methods: Surface Ellipsometry, Atomic Force Microscopy and Quartz Crystal Microbalance. The DFT model is the same as described in chapter 3, except that now all the polymers are tethered to the bottom of the cylinder to replicate a planar polymer brush. Such DFT results will have edge effects, as they are not truly planar with periodic boundary conditions. Thus, when analysing the density profiles of such calculations, we only analyse the inner parts of the cylinder (away from the wall), so that there are no boundary effects. The calculations were tested at different system radii in order to confirm that this didn't affect the results. Provided that the radius of the cylinder we are using for the modelling is large enough, the inner part of the density profile will be consistent with similar calculations performed with planar boundary conditions.

We again assume the same form for the interaction that we have used in our previous chapters:

$$\phi(\mathbf{r}) = \begin{cases} \infty & |\mathbf{r}| < d \\ \epsilon \exp(-(|\mathbf{r}| - d)/\lambda) & |\mathbf{r}| \geq d \end{cases} \tag{6.1}$$

which is a potential consistent with the hydrophobic interactions thought to be important in the pore. We can then vary ϵ and measure the thickness to determine which sorts of interactions best describe different nups.

Different nups have different physical properties. In our modelling of planar polymer films the difference between the nups is represented by the changes in their length. The nups that are modelled are: nsp1, nup98Glyco and PSF1320. These nups are cohesive and are essential for NPC function[8]. These nups have contour lengths of approximately 600, 485 and 307 amino acids respectively. We take each polymer as consisting of 0.76 nm subunits, corresponding to twice the length of an amino acid.

The measurement of the thickness of a film is ambiguous, as there is no sharp cut off of the

polymer density, rather, there is a continuous decrease. We define the thickness of a film in density functional theory as being the point at which the density of the film falls to below 0.001 of the maximum. This cut off point is largely arbitrary, we could just as easily choose 0.01 or 0.005, however this does not lead to huge changes in the values of the thickness extracted. This is illustrated by plotting the polymer density profiles on a logarithmic scale.

The only other parameters that are included from the experiment are the tethering density of the nups. Thus our model has just one parameter that can be varied, ϵ the strength of the interaction. The λ, which represents the range of the interaction, is set to be 1 nm, consistent with experiments on the possible range of the hydrophobic interaction[37]. The effects of varying λ produce results that are similar to varying ϵ, as you are just increasing or decreasing the interaction that each particle is experiencing.

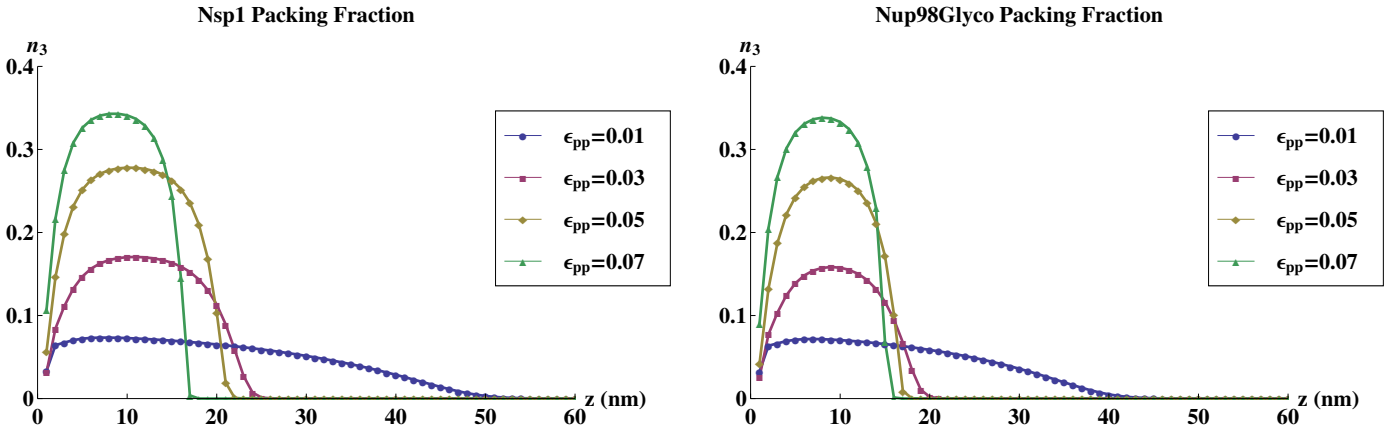

Figure 6.1: Bead packing fraction n_3 of a plane of tethered nsp1 and nup98glyco against vertical distance. The packing fractions shown are for a grafting density of 5.48pmol cm^{-2} of polymers tethered at the bottom of a cylinder of radius 50 nm. The length of nsp1 is taken to be 600 amino acids of length 0.38 nm, and nup98glyco is taken to be 485 amino acids. We change ϵ_{pp} to find the value that best agrees with the experimental results.

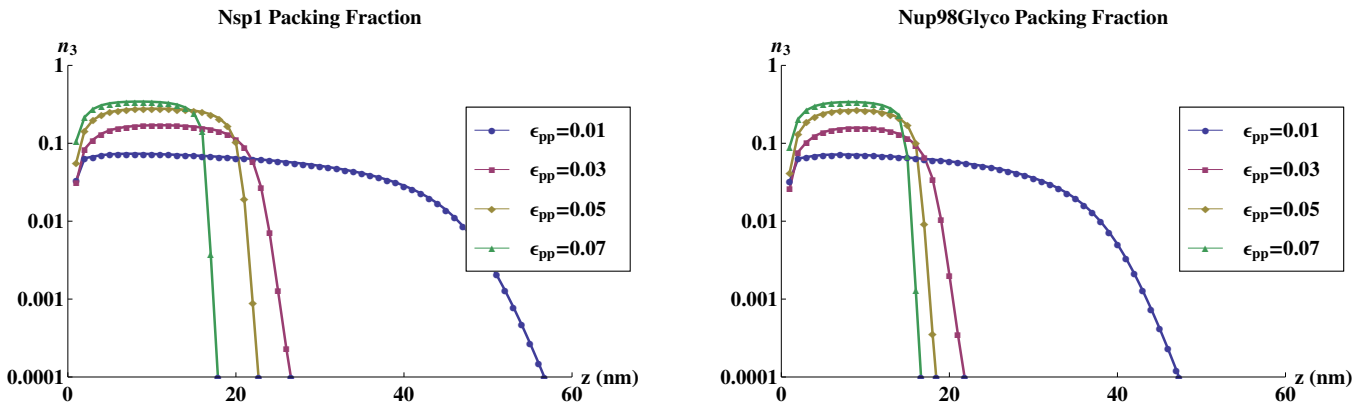

Figure 6.2: Bead packing fraction n_3 of a plane of tethered nsp1 and nup98glyco. The data is the same as in figure 6.1 but plotted on a logarithmic scale. This figure gives an example of the changes in thickness depending on what cut off is chosen.

The density profiles of these polymer brushes are shown in figure 6.1 and again on a logarithmic scale in 6.2. There are several similarities between the simulations of nup98glyco and nsp1, which should be expected as the only difference in these calculations are the lengths of the polymers. At low interaction strengths (small ϵ) the polymers stretch out quite far. The dominant term under this regime is the hard sphere repulsion between the polymer beads. As the interaction strength is increased the polymer profiles go more into a tighter parabolic shape. The increase in the attraction causes a collapse of the polymer brush. These results agree well with the theory of polymer brushes[93]. This allows us to plot a range of thickness against the interaction strength, as seen in figure 6.3.

These figures can be compared against the thicknesses that were measured in experiment thus allowing us to see what values of ϵ_{pp} best represent the different nups.

Using the experimental data that is represented in 6.4 the thickness of the wild type nsp1 is given by 25 ± 8 nm and for nup98glyco the thickness is 17 ± 3 nm. These correspond to ϵ_{pp} ranges of our calculations of between 0.03 and $0.05 k_b T$ for nsp1 and 0.05 and $0.07 k_b T$ for nup98glyco.

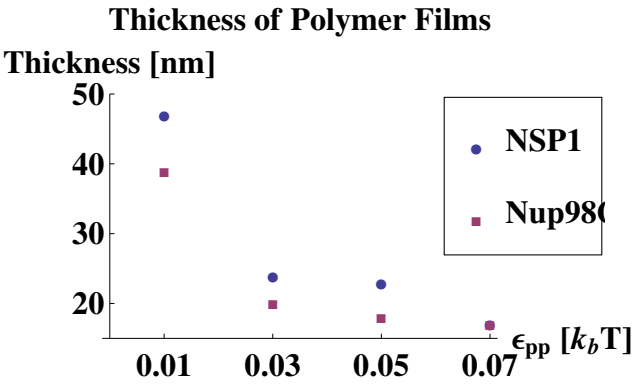

Figure 6.3: Thickness of an nsp1 film at different values of the interaction strength ϵ. The thickness was measured using the methods described in the text. There is an error on each measurement of the thicknesses, which is difficult to quantify, but can be seen from 6.2.

Simulations have also been performed by Miao et al. [33] on a planar array of nsp1. These simulations attempt to include molecular detail that is usually ignored in other simulations, including ours. However, the simulations were performed on only a part of the nsp1 with a total end to end length of 41.6 nm. The simulations were performed with 25 such subsections of nsp1, on a 13 by 13 nm array. This corresponds to a areal density of 24.5 pmol cm^{-2}. These simulations find a brush height of between 7-8 nm. Whilst our simulations are of a different nature, with much longer (242 nm) nsp1, the results are consistent with the simulations, with the ratio of chain size to brush height of 0.17 for the simulations and 0.1 for our calculations. The discrepancy could be caused by the different grafting density of nsp1 used in the simulations.

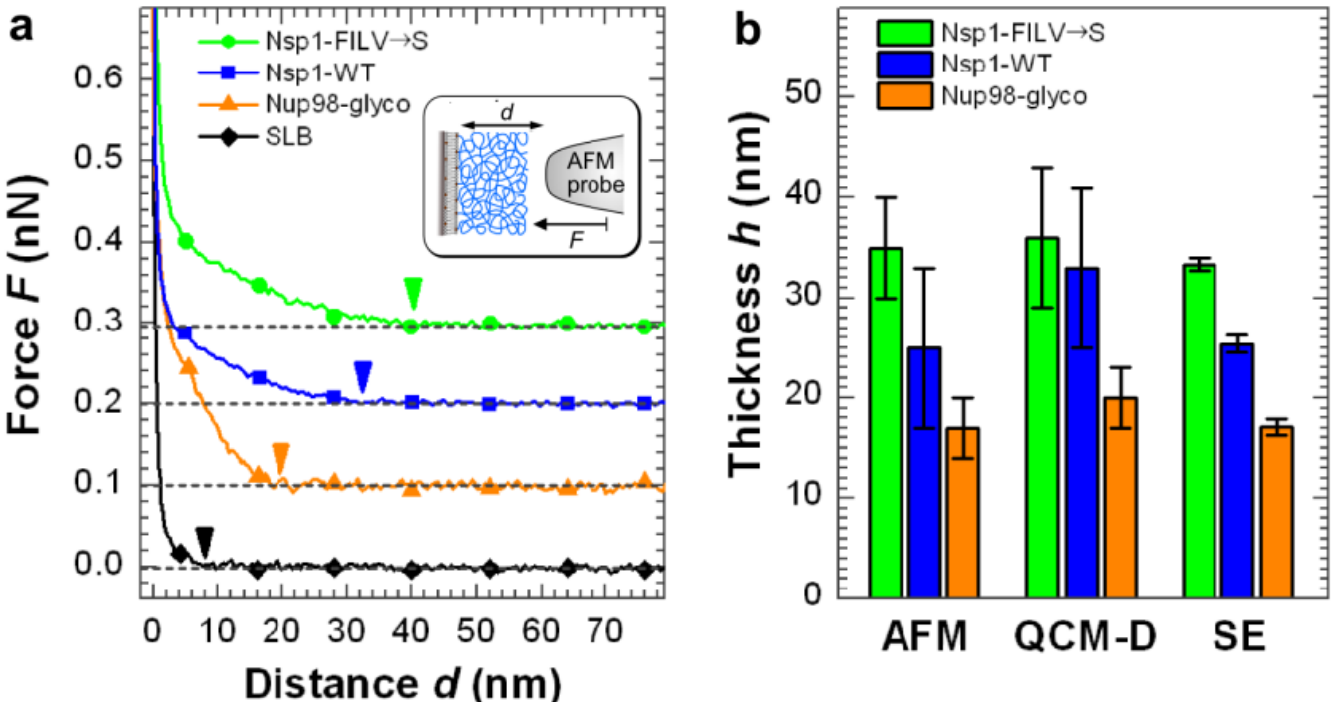

Figure 6.4: Figure taken from Eisele *et al*, Biophys. J. Volume 105, Issue 8, 15 October 2013, Pages 18601870. A) shows AFM indentation assays on nup films on various types. The thickness is determined in AFM by checking the difference between the onset of the repulsive forces (marked by the arrow heads) and $d = 0$. B) shows the thicknesses of various different nup films (nup98glyco, wild type nsp1, and a modification of nsp1) using the 3 different methods mentioned before (AFM,QCM-D,SE)

6.2 Extension to mixtures of plane polymer brushes with NTRs

These experiments can be taken further to incorporate the effects that NTRs may cause on the polymer films. It was previously reported by Lim et al that NTRs cause reversible collapse in films of nups [72]. The precise interaction between the nups and the NTRs is of great importance in our model, because as we have seen already, different NTR-nup interaction strength can lead to great differences in equilibrium phases. Currently, experiments have not precisely determined where the NTRs will be localised in the film, therefore this is an area where our model has predictive power and is able to guide experiment.

Richter and collaborators expanded their experiments to include the effects of NTRs by adding a solution of NTF2 to the planar polymer brushes. NTF2 is another NTR found within the cell, similar to the importins which we modelled in chapter 5. The interaction between NTF2 and the the nups is ϵ_{pf} The main difference of this model compared to our model of interacting importins in the NPC is that, once again, the nups are tethered at the bottom of the cylinder. In addition, the radius of the NTF2 is taken to be 2.5 nm, different from the 4 nm radius that we used when modelling the importins. We chose this radius by overlaying a sphere over the molecular structure of NTF2 taken from x-ray crystallography measurements of the NTF2 [94].

By measuring both the thickness of the film after exposure to an NTR solution and the number of NTRs bound to the film, the thermodynamics of NTR binding to films of nups can be determined. The comparisons between experimental and theoretical data are shown in figure 6.5 and 6.6.

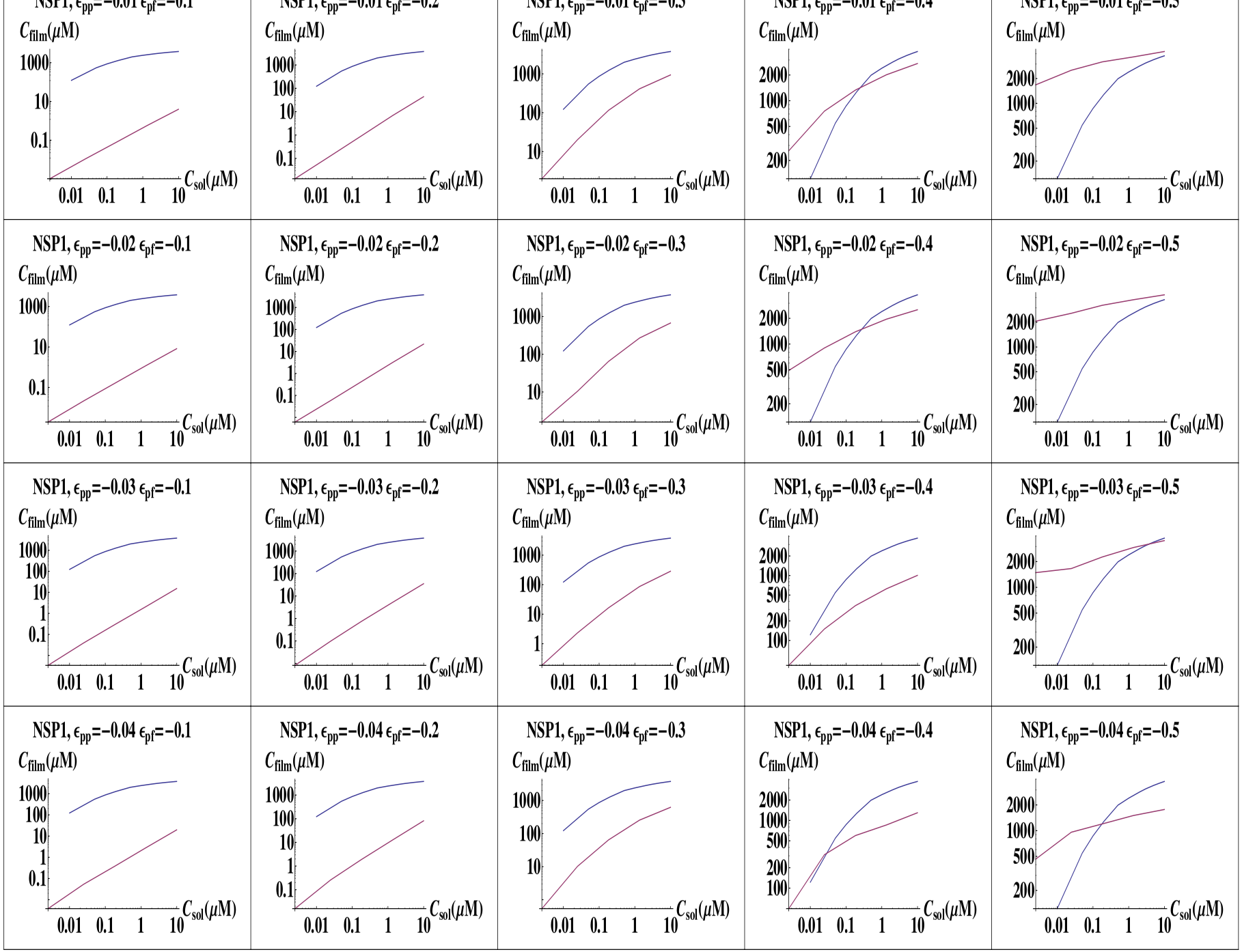

Figure 6.5: Comparison of the total concentration of NTRs in the nup film c_{film} against the concentration of NTRs in solution (c_{sol}) between experiment (blue) and theory (red) for all the different values of the nup parameters ϵ_{pp} and ϵ_{pf} used in the modelling work. In general, increasing the concentration of NTRs in solution increases the number of NTRs absorbed into the film. The qualitative behaviour seen in experiments can be captured by our simple model.

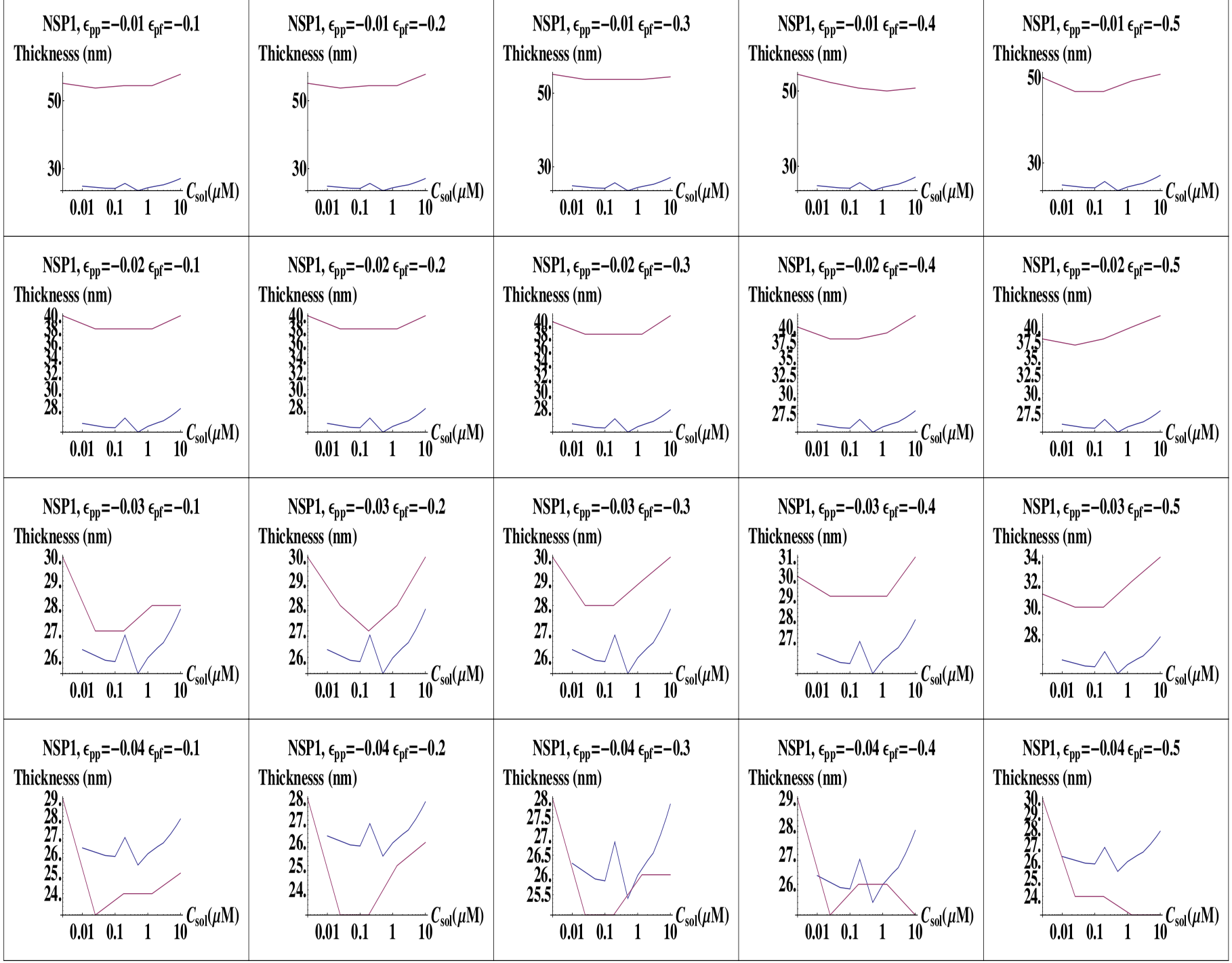

Figure 6.6: Comparison of the nup/NTR film thickness against concentration of NTRs in solution between experiment (blue) and theory (red) for all the different values of the nup and NTR parameters ϵ_{pp} and ϵ_{pf} used in the modelling work. We can obtain thicknesses that agree well with the values that are obtained in the experimental model, though the exact behaviour is difficult to capture.

By comparing the difference between the theoretical and experimental density and thickness curves, we can determine which set of microscopic parameters have the best agreement with the experimental results. The variances indicate that the best set of theoretical parameters are between $\epsilon_{pp} = 0.03$ and $\epsilon_{pp} = 0.04k_bT$ and $\epsilon_{pf} = 0.4k_bT$ and $\epsilon_{pf} = 0.5k_bT$ The ϵ_{pp} are consistent with the results obtained when films without NTRs were modelled, as is expected.

The theoretical results match the experimental results to within around a factor of 2 over 4 orders of magnitude. However, the precise amount of NTRs absorbed by the film differs in the experimental and theoretical approaches. There could be a few reasons for this disparity, however we hypothesise that the disparity is caused by the over estimation of the hard sphere repulsion of NTF2. While we overlay a 2.5 nm over the NTF2 molecule to model it is a hard sphere, there are significant volumes of empty space without the space. A truly accurate representation of the NTF2 would result in a smaller effective hard sphere diameter, resulting in more molecules being absorbed.

By looking at the theoretical densities of the films we are able to make a prediction about the behaviour of the NTRs interacting with nup films. For the set of parameters where we find the best agreement, the combined NTF2/nup density is shown in figure 6.7 Our finding is that the experimental data, as compared with our modelling data, suggests that the NTF2 sit on the surface of the nsp1 film. Upon increasing the concentration of NTRs in solution, the number of nups adsorbed upon the film increases. This increase cannot go on indefinitely, once the density on the surface of the film approaches the maximum, which is set by the packing fraction, then the number of NTF2 adsorbed to the surface will no longer increase, either the NTF2 will permeate into the pore, or will remain in solution without influencing the nup film. Once this saturation limit is reached, the effect of further NTF2 on the nup film is minimal. The best matching results appear to be close to the transition point where the NTF2 begins to permeate the film.

6.3 Comparison with AFM of intact Nuclear Pore Complexes

In the previous section, we compared the accuracy of our model against a simplified model system consisting of proteins found in the NPC. However, we would like to extend this further and see how our model compares against a full NPC, where factors such as the NPC geometry will play

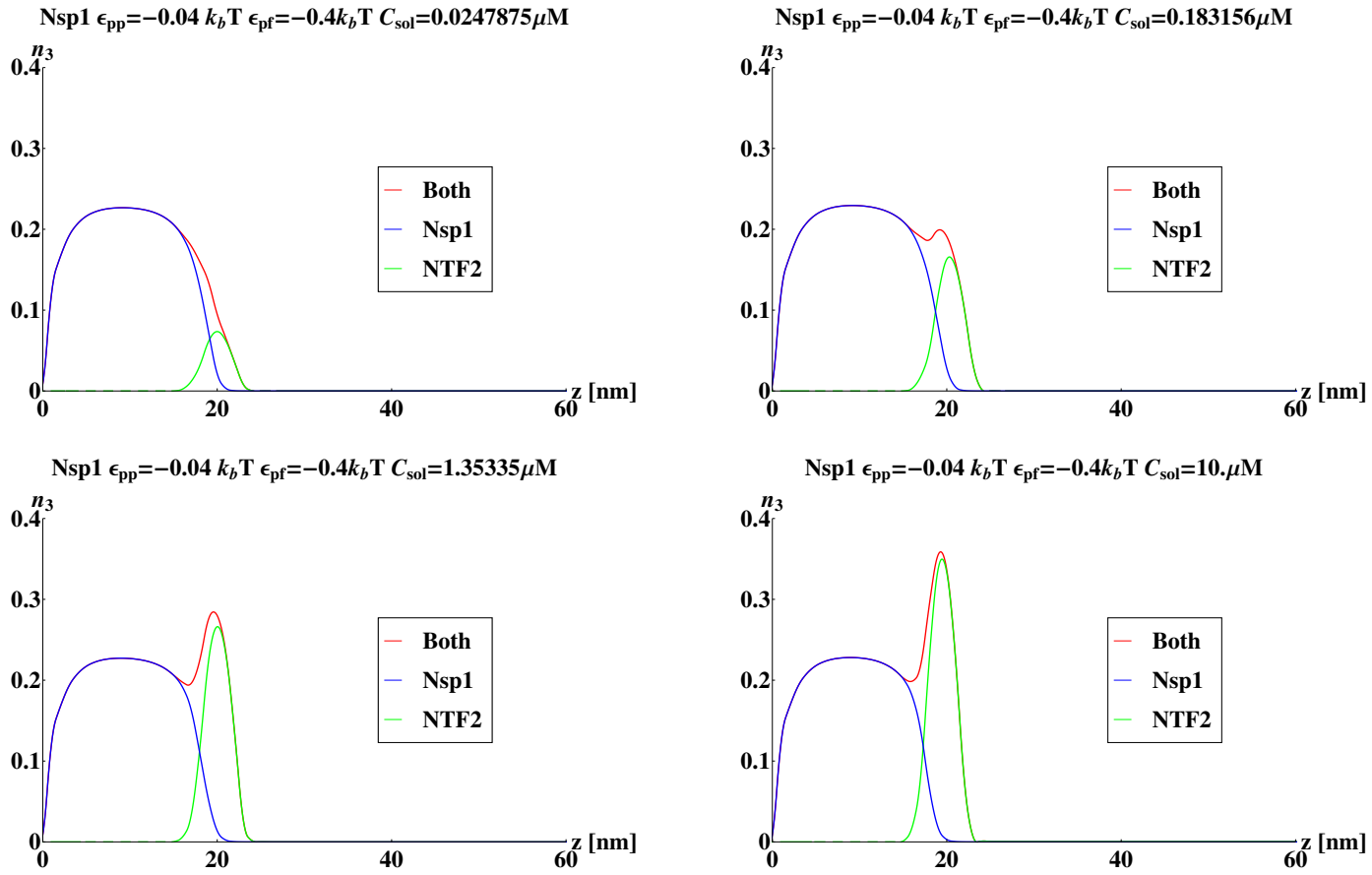

Figure 6.7: Theoretical packing fractions of NTF2 and nsp1 at the interaction parameters which agree the best with experimental data, at different values of NTF2 concentration in solution C_{sol}. These interaction parameters are determined from the comparison between the experimental and theoretical thicknesses and the adsorption curves.

an important part. There have been many experiments performed on the NPC. We shall compare our theoretical results with experimental results obtained by atomic force microscopy (AFM) on full intact functional pores.

Atomic force microscopy can measure the mechanical response of the NPC due to indentation by the probe. This force spectroscopy is something that can be readily compared with similar theoretical results. In particular, atomic force microscopy measurements of the pore can give a stiffness map of the inside of the pore, giving us information about where the pore is stiffest. In the AFM experimental method, the deflection of the tip is measured and these values are converted to a force. From the force curve, the stiffness is obtained by taking a derivative of the force. An example of these AFM results is summarised in figure 6.8.

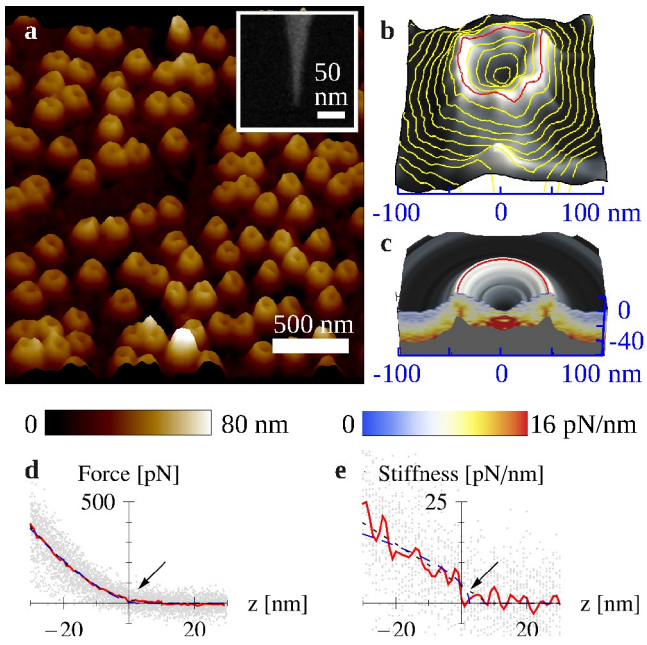

Figure 6.8: Overview of experimental results obtained when performing AFM on NPCs. Taken from Bestembayeva and Kramer *et al.* (a) shows an AFM image of the nuclear envelope taken with AFM, as can be seen, there are many NPCs perforating the surface. (b) Reconstruction of a single NPC from force spectroscopy. (c) is the version of b where the results have been rotationally averaged, where the blue to red colour scale represents the magnitude of the stiffness. (d) and (e) are force and stiffness curves respectively, where the force and stiffness are plotted as a function of tip-sample distance.

As can be seen in figure 6.8, the stiffness map of the pore suggests that it is stiffest in the centre. This is in line with the central plug mentioned in chapter 1. The force map of the NPC can be obtained theoretically from density functional theory with some simple modifications to the functional. However, the only force curve that we can get in this way is the $r = 0$ axis, due to the rotational symmetry assumption that we impose on the system.

$$F_{\mathrm{AFM}}[\rho(\mathbf{r}), z_c] = F_p[\rho(\mathbf{r})] + \int \mathrm{d}\mathbf{r}\, V_{\mathrm{tip}}(\mathbf{r}, z_c)\rho(\mathbf{r}) \tag{6.2}$$

Equation (6.2) shows the modification of the functional to account for the AFM tip. F_p is the functional of the polymers in the absence of any tip, as seen in the chapter 3. The addition we make is by adding a potential of the form V_{tip} that accounts for the interaction between the polymers and the tip. The form of interaction between the tip and the polymers is assumed to be exclusive only, i.e. the tip and the polymers cannot occupy the same space, but there are no further long range attractive or repulsive forces between the tip and the polymers. This assumption can be

justified from the shape of the experimental force curves. The coordinate z_c gives the position of the end of the tip along the central axis of the NPC. The rest of the tip potential is defined by the manufacturer's details, such as aspect ratio and tip radius.

To match our theory against experiment, we take z_c along different points along the central axis of the pore, and record the free energy at each point. The theoretical force curve is then given by:

$$\text{Force(z)} = \frac{\partial F_{\text{AFM}}[\rho(\mathbf{r}), z_c]}{\partial z_c}|_{z_c=z} \tag{6.3}$$

Using this theoretical method, we can then compare what polymer regime (corresponding to different e_{pp}) best agrees with the experimental force curves obtained. Note that in these calculations, the effect of the NTRs has not been included. Experimental controls were performed to wash the pores of NTRs, however these control experiments do not perfectly demonstrate whether or not the pore was completely washed out, however, the resulting force curves did not display a large difference from the full pore experiments. The results of the theoretical AFM calculations are shown in figure 6.9.

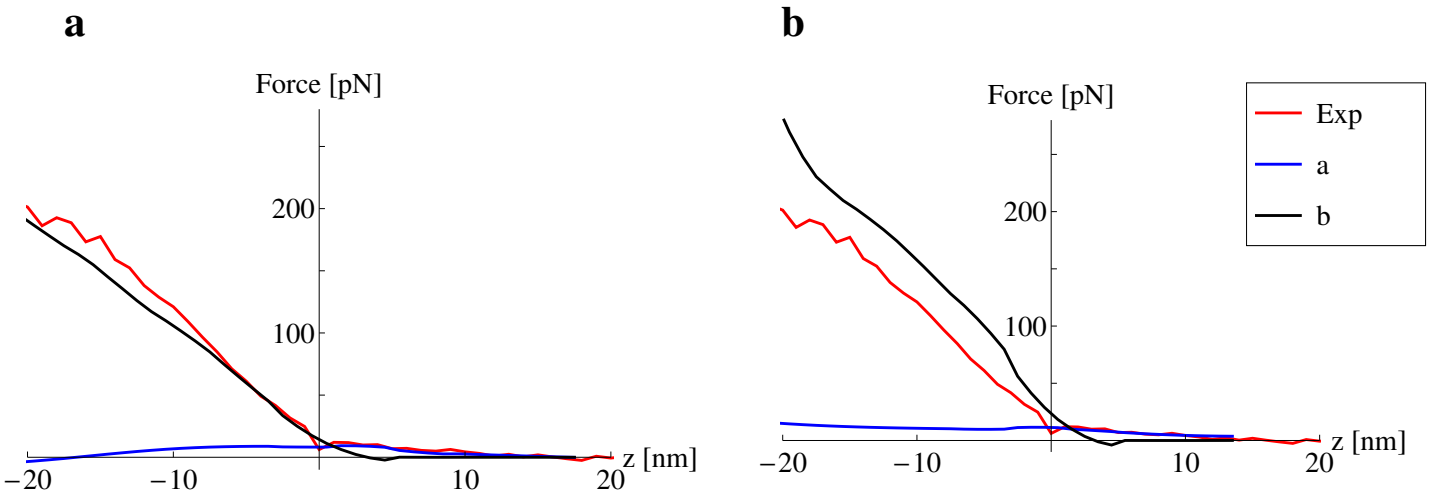

Figure 6.9: Comparison of experimental and theoretical force curves on intact Nuclear Pore Complexes for a tip of a) 2 nm radius and b) 4 nm radius against experimental force curves of a tip of $2-4$ nm. The different curves represent the AFM experimental force curve (red) and the theoretical curves at, $\epsilon_{pp} = 0.02$ (blue) and $\epsilon_{pp} = 0.05$ (black). We obatined the theoretical force curve by indenting the pore with an external potential and meauring the free energy difference at different values of the indentation. We then differentiate this to obtain the force. The experimental force curves were obtained in AFM by indenting NPCs with a tip and measuring the deflection. The curves show encouraging agreement between our minimal model and full AFM experiments.

From this figure, it can be seen that the case when $\epsilon_{pp} = 0.05$ matches extremely well with the data collected on the NPC with a 2 nm tip. At $\epsilon_{pp} = 0.05$ the majority of the polymers are tightly condensed with a sizeable central plug present. These calculations therefore support the hypothesis that the central plug is caused by a meshwork of nups extending into the central channel of the pore, as opposed to the idea that it is merely cargo in transit[3]. Another piece of evidence comes from the shape of the force curve obtained from the experiments, which shows an abrupt increase in the force around $z = 0$, the contact point. This supports the gel model of polymers. If the polymers were more freely fluctuating, the expectation would be that the force curve would increase exponentially.

In conclusion, in this chapter we compared the findings of our model against experimental evidence collected by our collaborators. Despite the many simplifications in our model we find that it does a reasonable job of capturing many aspects of nup behaviour as seen in the various experiments. In particular, we are able to obtain very good agreement with AFM experiments on intact NPCs.

Having compared our model against the structural experiments on nup structure, we take it further to see how well our model captures the dynamics of the NPC, such as facilitated transport.

Chapter 7

Theoretical Transport Measurements

Despite continuing progress in the determination of NPC scaffold structure, the transport channel of the NPC itself still eludes molecular scale characterisation. As discussed in chapter 1, molecular dynamics simulations suffer from their need to include assumptions about the parameters involved in order to make progress. This can lead to diverging results between the different molecular dynamics approaches. In this chapter, we try to determine the viability of various structures against experiment, and proceed by exclusion.

In order for a pore to be considered functional there are several criteria that must be fulfilled. These criteria come from experimentally measured details of the NPC.

- The NPC must be permeable to small cargoes. Passive transport of small cargoes is a well known facet of the NPC transport. Cargoes of up to 65 kDa (5-6 nm in diameter [95]) are able to transverse the pore without the need to bind to nuclear transport receptors.

- NTRs themselves must be able to transverse the pore. NTRs are known to continuously shuttle across the pore.[13, 70]

- Cargo selectivity. Cargoes above the size limit for passive diffusion should be excluded from transversing the pore. However, if these cargoes are bound to NTRs they should be able to cross. Even cargoes of large radii[15] should be able to cross provided they are bound with enough NTRs. As seen from viral transport, even cargoes of similar dimensions to the NPC are able to cross over from the cytoplasm to the nucleus.

In order to determine transport rates a similar method to that used in the theoretical AFM experiments is used. We represent the transversing particles as an external potential in the func-

tional. This external potential has the properties that match those of an NTR or a cargo.

$$F_{\mathrm{T}}[\rho(\mathbf{r}), z_c] = F[\rho_f(\mathbf{r}), \rho_p(\mathbf{r})] + \int \mathrm{d}\mathbf{r}\, V_{\mathrm{Pext}}(\mathbf{r}, z_c)\rho_p(\mathbf{r}) + \int \mathrm{d}\mathbf{r}\, V_{\mathrm{Fext}}(\mathbf{r}, z_c)\rho_f(\mathbf{r}) \tag{7.1}$$

F_{T} is the modified free energy functional for transport. It is the free energy functional that changes as a functional z_c, the distance along the central axis of the cargo in question . ρ_p and ρ_f are the density of the polymers and the NTRs respectively. V_{Pext} and V_{Fext} are the external potentials corresponding to the interaction of one cargo or NTR with the polymers and the NTRs. This is given by:

$$V_{\mathrm{Ext}}(\mathbf{r}, z_c) = \begin{cases} \infty & |\mathbf{r}| < d_{\mathrm{exc}} \\ \epsilon_{\mathrm{Ext}} \exp(-(|\mathbf{r}| - d_{\mathrm{exc}})/\lambda) & |\mathbf{r}| \geq d_{\mathrm{exc}} \end{cases} \tag{7.2}$$

where ϵ_{Ext} is the energy of the interaction of the cargo with the particles on its surface, d_{exc} is the excluded volume of the cargo.

By calculating F_T at different positions along the pore, we can obtain a free energy curve for cargoes at different points along the central axis of the NPC. We assume symmetry in the z axis at $z = 0$. We use a concentration of $10\mu M$ for NTRs. Using this free energy curve we can obtain transport rates.

There are several assumptions that have to be made in order to determine the transport viability. Firstly, the calculations performed determine the states at equilibrium. I.e., there is a succession of equilibrium states as we move the cargo/NTR through the pore. It is possible that there are non-equilibrium effects during the transport process. We assume that the equilibrium relaxation time of the components of the system is fast compared to the movement of the cargoes through the pore. Secondly, we can only determine transport along the central axis of the pore, due to the rotational symmetry assumption employed (see chapter 4). It has been hypothesized that cargoes can travel along different channels, such as along the side of the pore[73], however this is something that our model cannot capture. In the limit of large cargoes, this assumption becomes more valid as there are less ways a cargo can fit through as it approaches the size of the pore. Thirdly, we assume that the cooperative effects of cargo transport are negligible. We determine the free energy by dragging a single particle through the pore, this ignores the possibility that the transport is the result of many particles moving through the pore.

As discussed previously, when the pore is modelled with 216 polymers of contour length 161 nm, the discussed dichotomy between central and wall phases is lessened. If we return to the phase

map that we plotted before, there now only exists a transition between the polymers and fluid being separated and the mixing of these states in a network. Excluded volume interactions alone are enough to provide a full filling of the central channel of the pore. The important values are the parameters ϵ_{pp} and ϵ_{pf} the strength of the interaction between the fluid and the polymers and the strength of interaction between the polymers themselves. We restrict the other interaction parameters by assuming that the range of the interactions λ is approximately 1 nm, in agreement with experiment. Different ϵ_{pp} correspond to different behaviours of the nups within the central channel. With low ϵ_{pp} indicating the polymers are more freely fluctuating, whereas a large value of ϵ_{pp} corresponds to a more gel like state.

We discuss the pore permeability barriers in terms of free energy. If there is a large free energy cost to the translocation of any particular cargo, this means that the time for transversal is very large, i.e. far larger than physiological time scales. However small free energy barriers allow for easier transport of cargoes. The precise rates at which cargoes go through the pore will depend on not only the free energy barrier, but their attempt frequency, which depends on parameters such as the diffusion constant of the particle. As a general rule, transport over free energy barriers of size F_b is given by:

$$R = A \exp(-F_b/k_bT) \tag{7.3}$$

where R is the rate of transport and A is the prefactor which is the "attempt frequency" with which particles attempt to cross the barrier. This factor will depend on the precise form of the barrier and the damping constant γ, which is related to the number of collisions. However, we can relate this attempt frequency with the damping constant γ which is of the order 10^{12} [96] for importin-β. Thus we set A to be γ. This simple form of transport rates show that the rate is exponentially suppressed with increasing free energy barriers. A free energy barrier of 27 k_bT would correspond to transport rates of 1 particle s^{-1}. We consider barriers of $30k_bT$ as being essentially impermeable to cargoes. This barrier correspond to the upper limit of bovine serum albumin (BSA) transport measured in reference [13]. The BSA particle is inert and should not be able to cross the NPC.

7.1 Barrier to inert particles

One of the most vital aspects of the NPC is that it presents a barrier to inert particles, that is to say particles which are not bound to NTRs. We present data here that shows at which conditions the NPC is impermeable to inert particles. As discussed previously, the exclusion limit for inert particles is around $5-6$ nm diameter. We test whether particles larger than this are excluded by doing dragging inert (non-interacting with the polymers or the NTRs beyond the hard sphere repulsion) particles through the central axis of the pore. We drag particles of 8 nm diameter through the pore. As mentioned, we vary ϵ_{pp} and ϵ_{pf} and measure the total barrier to transport. These results are summarised in figure 7.1

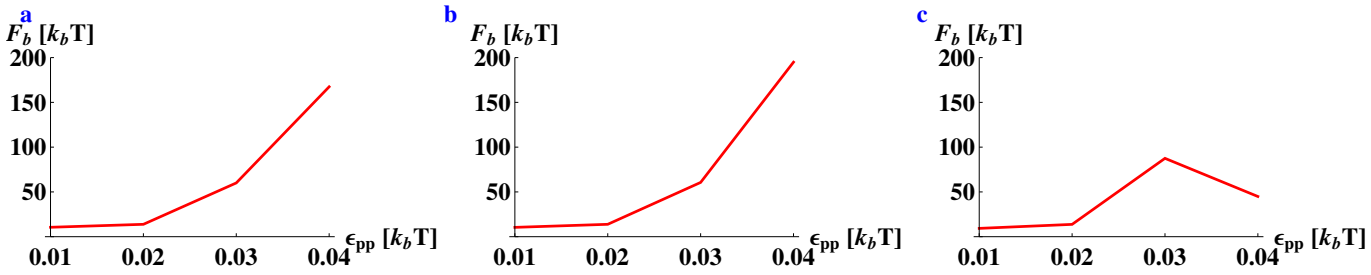

Figure 7.1: The total free energy barrier (the free energy difference between the cargo being outside the pore and in the middle of the pore at $z = 0$) presented to 8nm diameter inert particles at different ϵ_{pp} for the cases where $\epsilon_{pf} = 0.1k_bT$ (a), $\epsilon_{pf} = 0.2k_bT$ (b) and $\epsilon_{pf} = 0.3k_bT$ (c).

From figure 7.1 we can see the general trends in terms of the barrier facing inert particles. At low ϵ_{pp} there is not a large barrier presented to the polymers. This regime, where the polymers are more freely moving and fluctuating, would correspond more to the "virtual gate" model of NPC barrier organisation[20]. Upon increasing ϵ_{pp} further, the barrier starts increasing exponentially. In this regime, the polymers are more tightly condensed, increasing the energetic cost for any translocation.

The barrier facing inert particles does not depend too strongly upon the value of ϵ_{pf}, until we get to the point at $\epsilon_{pp} = 0.04$ and $\epsilon_{pf} = 0.3$, where, as we have discussed before, the central region of the pore is mainly constituted of NTRs. When we reach this value, the barrier facing inert particles actually decreases, probably because for these parameters the barrier is constituted of NTRs rather than polymers, leading to different effects determining the size of the barrier. At this

point, the cost of dragging a particle through the centre of the pore is due to the disruption of the NTR-polymer interactions, rather than polymer-polymer interactions as before. However, even in this case the free energy cost is still $50k_bT$, which is too large for inert particle translocation (as per our discussion in the previous section).

A functioning barrier appears to require that there be a significant agglomeration of polymers or NTRs in the centre of the pore. The free energy cost for particles above the passive diffusion size limit is not very large when there are no attractive interaction between the polymers themselves. This leads to the idea that reasonable (as defined by the criteria in the previous section) free energy barriers to inert molecules are largely enthalpic in nature, that is to say the cost is mainly associated with disruption of the bonding of the polymers or the NTRs. We know we can restrict our range of physiologically reasonable interaction parameters to cases with ϵ_{pp} approximately larger than $0.03k_bT$. Repeating these calculations with inert cargoes of larger radii results in larger free energy barriers, as is to be expected.

7.2 Passive diffusion

As discussed in the opening of this chapter, one element of NPC functionality is the permeability of the NPC to particles below a certain size limit. These macromolecules are able to diffuse through the pore without binding to transport receptors. This means that there isn't a large free energy barrier present to these molecules, even in the absence of attractive interactions between the passively diffusing molecules and the nups. We test the free energy barrier presented to a 4 nm diameter particle.

We see a similar trend as that observed in the previous section, as seen in figure 7.2, which is to be expected as the calculations are functionally the same, the only difference being that in this set of calculations the radius of the cargoes is halved. Most of these parameter sets of ϵ_{pp} and ϵ_{pf} correspond to situations where passive transport is allowed, (barriers of up to $20k_bT$ do not pose significant problems for particles with these attempt frequencies). Once again we see that increasing ϵ_{pp} decreases the rate at which particle would be able to move through the pore. Again, the point $\epsilon_{pp} = 0.04$ and $\epsilon_{pf} = 0.3$ diverges from this trend due to the fact that the centre of the pore is constituted by NTRs.

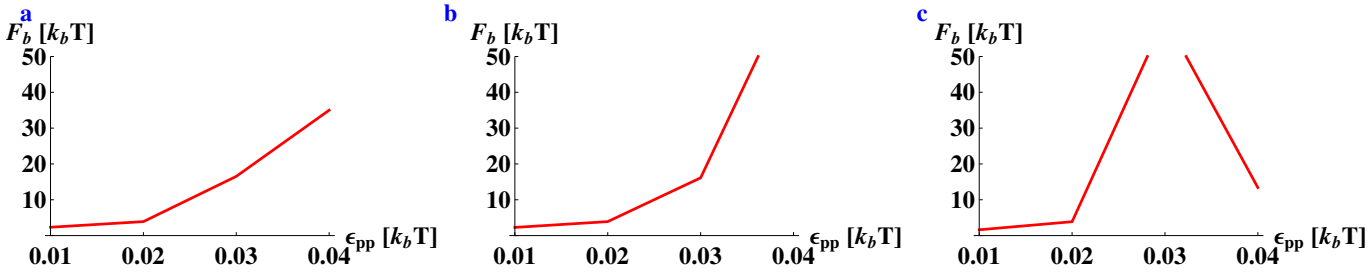

Figure 7.2: The total free energy barrier (the free energy difference between the cargo being outside the pore and in the middle of the pore at $z = 0$) presented to small 4nm diameter particles below the size exclusion limit of passive diffusion through the pore. Results presented as free energy barrier against increasing ϵ_{pp} at different ϵ_{pp} for the cases where $\epsilon_{pf} = 0.1$ (a), $\epsilon_{pf} = 0.2$ (b) and $\epsilon_{pf} = 0.3$ (c).

7.3 NTR transport

One of the points mentioned above is that NTRs are able to cross the NPC by themselves. Experiments [13, 70, 97, 98] on cells show that when fluorescently NTRs are injected into either the nucleus or the cytoplasm, their distribution quickly equilibrates such that they can be found throughout the whole cell.

In terms of physical language, this means that the free energy barrier to NTRs across the NPC is not inhibitively large. We can use our model from chapter 5 to determine the free energy barriers facing individual NTRs. The form of the external potential that we choose for the functional equation 7.1 is the same as used for NTR interactions with the nups. An example of the particle dragging procedure is shown in figure 7.3

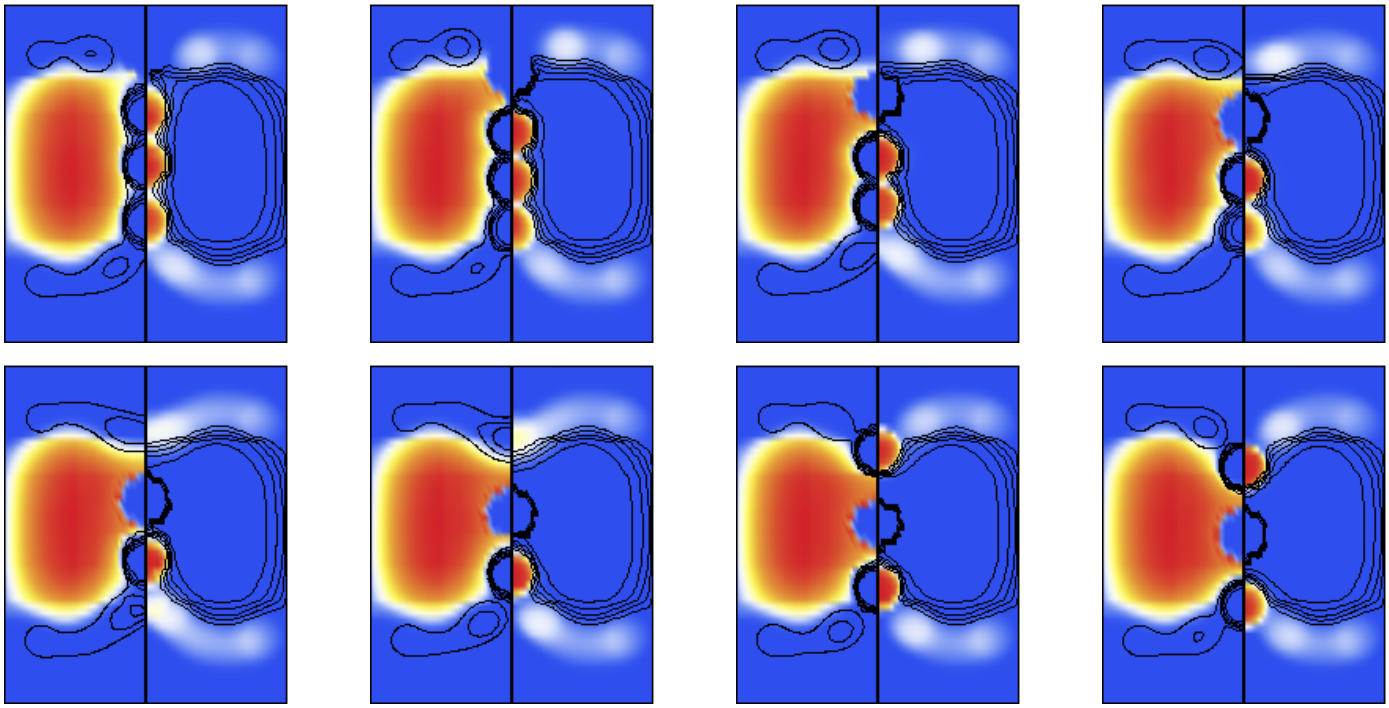

Figure 7.3: Changes in the density of the nups and NTRs as an external potential representing an NTR is dragged through the centre of the pore from the top. The plot is of the same form as seen in 5.4 The sequence goes from left to right, top to bottom. The polymers are disrupted by the initial insertion of the particle, however, the initial and final states are similar, with the external potential taking the place of one of the NTRs. These figures correspond to $\epsilon_{pp} = 0.04$ and $\epsilon_{pf} = 0.3 k_b T$.

The resulting free energy curves from calculations at various points can be seen in figure 7.4.

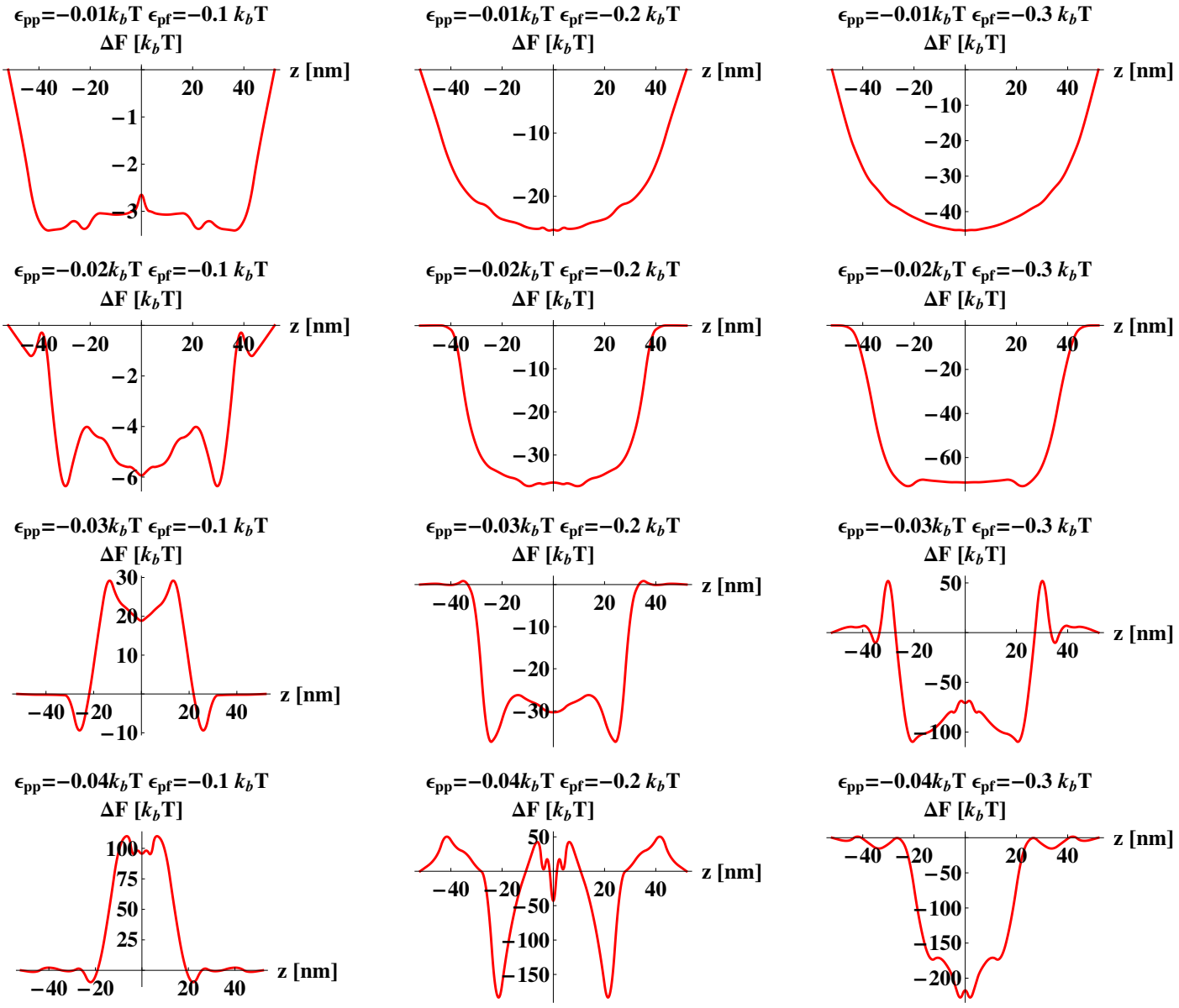

Figure 7.4: Free energy change ΔF as a single NTR, specified as an external potential, is dragged through the central axis of the pore along z. $z = 0$ corresponds to the half way point between the top and bottom of the pore. A variety of different behaviours can be observed.

All of these free energy curves correspond to equilibrium polymer structures given in figure 7.5.

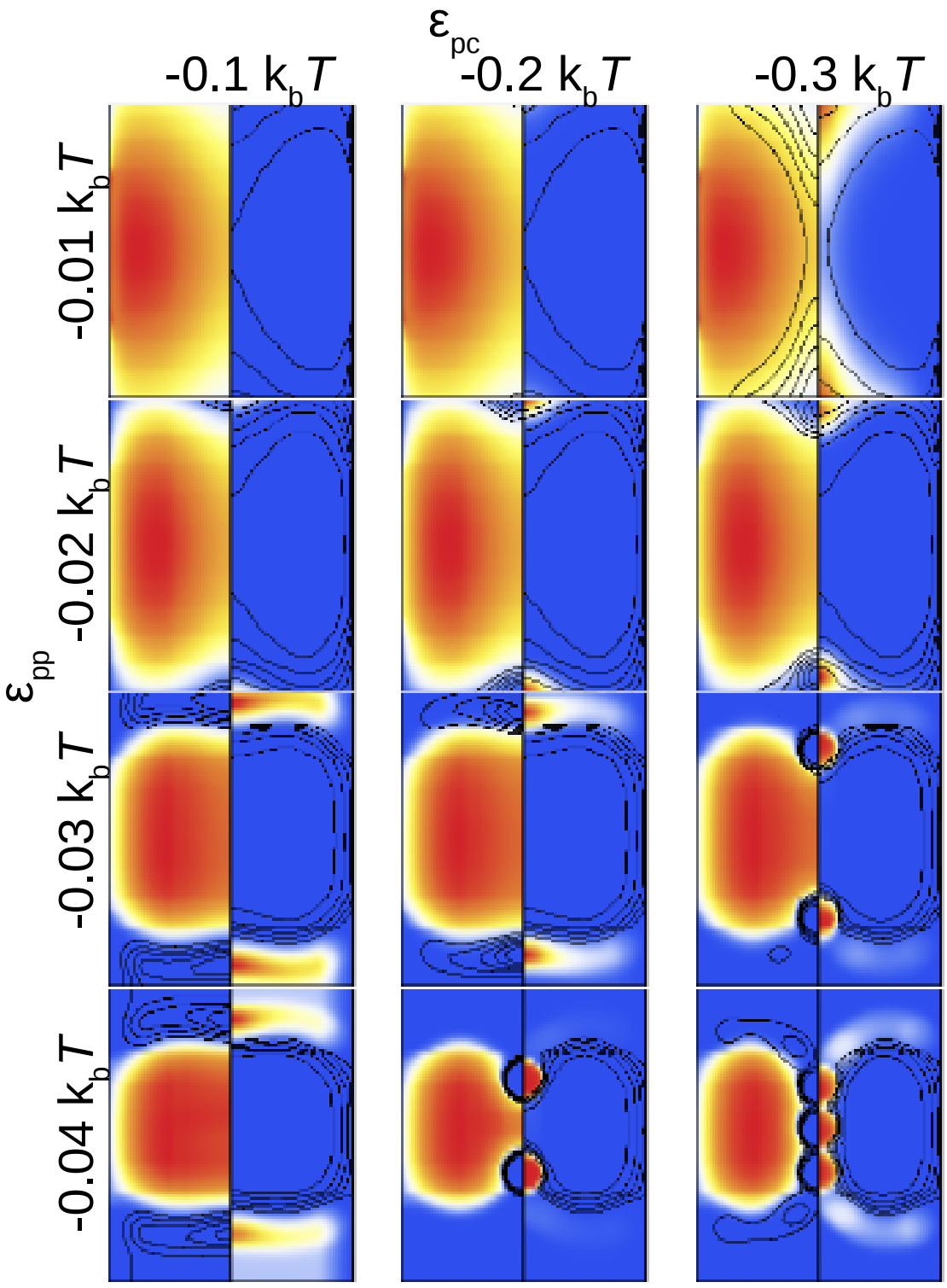

Figure 7.5: Density profiles of NTRs and nups without external potentials, corresponding to the different interaction parameters seen in figure 7.4. The density profiles are plotted in the same way as explained in 5.4. The NTR/nup distributions can change quite dramatically for different ϵ_{pp} and ϵ_{pc}.

For each set of parameters ϵ_{pp} and ϵ_{pf} we can obtain a separate free energy curve for dragging a single particle through the pore. These curves can often be difficult to interpret in terms of an exact rate of transport through the pore. It can be seen in figure 7.4 there are different types of free energy curves that we can categorise. These can be roughly thought of as follows: potential barriers, where there is a free energy cost to any NTR entering into the polymer condensate; double wells, where the NTRs prefer to sit on the surface of the polymer condensate and potential wells where the preference of the NTRs is to enter into the polymer condensate. From figure 7.4 we can note several trends in terms of ϵ_{pp} and ϵ_{pf}.

For lower ϵ_{pp}, this is easier for single NTRs to enter the pore, as can be seen in the case $\epsilon_{pp} = 0.01k_bT$, where increasing ϵ_{pf} results in larger potential well. For low ϵ_{pf}, such as at $\epsilon_{pf} = 0.1k_bT$, increasing ϵ_{pp} results in larger potential energy barriers. This can be understood physically as the energy cost of displacing the polymers. At large ϵ_{pp}, the polymers prefer to be in the centre of the pore (as discussed in chapter 3). By dragging a particle through, these polymers are displaced, thus increasing the surface area of the polymers. This energy cost cannot be offset by the attraction between the NTR being dragged through with the polymers.

Despite this, and perhaps unintuitively, at larger ϵ_{pf} an opposite trend can be observed. That is to say, as ϵ_{pp} is increased, the resulting potential well becomes deeper. At these larger ϵ_{pp}, the polymers form into a denser condensate. This denser concentration of polymers lead to larger attraction towards the NTRs, as the larger concentration of binding sites on the surface makes it more favourable for NTRs to be near the polymers.

The free energy curve results appear to contradict the results seen in figure 7.5, in that the by moving an NTR into the polymer condensate the free energy appears to be lowered, then why isn't this the true equilibrium state? This arises from the fact that we are arbitrarily moving a single NTR particle through a set of exact positions. There is a large entropic cost to localising particles in set positions that is essentially ignored in this approach. These free energy curves essentially tell where the optimum position for a single NTR is, but when there is a large reservoir of NTRs that are interacting with one another, different effects are present.

It is hard to determine from these free energy curves which parameters precisely NTRs would be free to transverse across the pore, if anywhere. The areas of the phase diagram where there is a barrier can be excluded, i.e., the regions where ϵ_{pf} is not significantly larger than ϵ_{pp}, such as the cases where $\epsilon_{pp} = 0.03k_bT$ and $\epsilon_{pf} = 0.1k_bT$. The cases where there are potential wells or

double wells are harder to distinguish. Large potential wells would seem to indicate that there are large agglomerations of NTRs in the pore. Physiologically, the concentration of NTRs in the cell is of the order of $10\ \mu M$. In a 25 nm cylinder of length 60 nm, this would correspond to less than one NTR in the pore (and even less if we consider the amount of space taken up by the polymers). However, the concentration of NTRs in the NPC is orders of magnitude larger than this. Therefore, we should consider a potential well for a single NTR to be the physiologically most reasonable state.

Physically, large potential wells would mean that NTRs are strongly attracted to the pore. However, once they are within the pore, it would be hard for them to leave. This raises an important question: If there is such a strong propensity for NTRs to enter the pore, how can they leave? It could be that there are cooperative effects at work which cannot be captured in single particle dragging calculations that we perform here. For instance, for the case $\epsilon_{pp} = 0.04 k_b T$ and $\epsilon_{pf} = 0.3 k_b T$ we see in figure 7.4 that there is a large potential well for a single NTR. However, we can also see in figure 7.3, that the original NTR distribution corresponds to a number of polymers with a central "plug" of NTRs. One can imagine a substitution of one NTR from the cytoplasm or the nucleus for another within that central plug, thus allowing "transport" of an NTR in a sense, even though the NTR that traverses is not the original one that enters. The free energy curve of such an event may look different to the curve obtained when one drags through a single particle from the top to the bottom. This effect cannot be captured in single particle dragging calculations that we have performed so far, but is a plausible hypothesis for empty NTRs (NTRs not bound with cargoes) translocation, given that we also know that the physiologically amplified concentrations of NTRs within the NPC also raise similar questions of particle escape. For example, in the case where $\epsilon_{pp} = 0.04 k_b T$ and $\epsilon_{pf} = 0.3 k_b T$, the total number of NTRs in the pore (excluding the external potential NTR) is 20, and after the external potential reaches the centre, the total number of NTRs is 18.4. This means some of the NTRs bound within the pore have escaped as the external potential is moved into the centre, resulting in a flux of particles through one side. However, were one to do simple Langevin dynamics of a single NTR moving in such a large potential well, the particle would get stuck in the well and wouldn't leave, meaning no flux of NTRs would be measured.

7.4 Cargo transport

We now come to facilitated cargo transport. This means cargoes which are larger than the size exclusion limit of passive diffusion through the NPC but can still diffuse through the pore if they bind to an NTR. This kind of calculations bring extra complications compared to those discussed in the previous sections. The cargoes that we drag through are now attractive to NTRs but have no interaction beyond excluded volume interactions with the polymers. A new parameter has to be introduced, controlling the strength of the interaction of the cargo with the NTRs. Instead of representing this interaction explicitly we introduce a factor σ_s, the surface density of transport receptors on the cargo, defined as $N_s/4\pi R_c^2$ where N_s is the number of NTRs bound on the surface and R_c is the radius of the cargo. We take this surface density to be fixed throughout the translocation process. This surface density is uniform around the cargo. We approximate the a priori surface coverage of cargoes with NTRs with a single phenomenological parameter that describes the average coverage of cargoes with NTRs. However, attempting to introduce non-uniform interactions around the cargo surface would lead to problems when we perform our cargo dragging experiments, as then the orientation of cargoes going through the pore becomes important. This cannot be effectively captured in a model where the azimuthal symmetry assumption is used. In addition to this, the cargoes might change their orientation as they translocate through the pore, leading to a large number of possible free energy curves. This is something that our model cannot capture effectively. The assumption that the surface density of NTRs around the cargo is the same essentially averages all the orientations through the pore. This is the only way to proceed in the current framework.

We do not allow any of the NTRs that are on the cargo surface to relax away from that position. If this calculation were to be performed naively, that is to say if we were to add an external potential to our functional that attracted NTRs and simply excluded polymers, the NTRs can rearrange around the cargo surface as the cargo is dragged through the pore. This leads to fluctuations in free energy that are purely due to the interaction between the NTRs on the cargo surface and the cargo, i.e., the rearrangement of the NTRs on the cargo surface. However, these free energies are not relevant when we consider the transport of cargoes through the pore, as the strength of the bond between the cargo and the NTR is not the rate defining step in facilitated transport. The important interaction is between the importins on the surface and the nups. Therefore we introduce a constant fixed density of NTRs around the cargo and drag the cargo-NTR complex

through. This ensures that the only effects we measure when we are dragging the particles through are the ones that are important for transport.

The impact of these surface densities on the equilibrium distributions are shown in figure 7.6

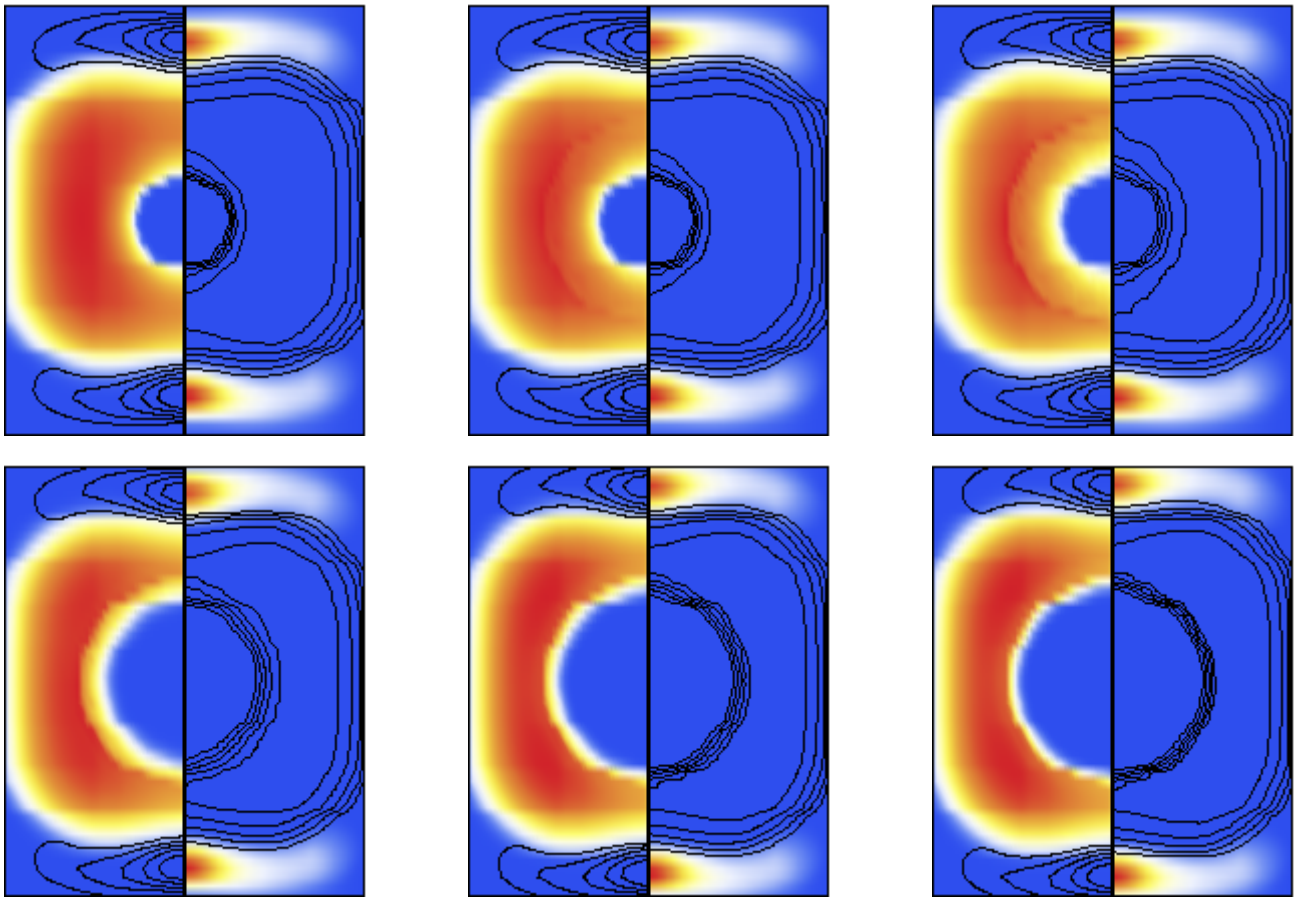

Figure 7.6: Effect of changing the surface density of NTRs bound to a cargo particle on the resultant nup/NTR distributions. In this case, a cargo particle of diameter 12 nm at $z = 0$ for $\epsilon_{pp} = 0.04 k_b T$ and $\epsilon_{pf} = 0.2 k_b T$. From left to right, top to bottom, the surface density of transport receptors is increased from 0 to 0.05 nm^{-2}, corresponding to 0,4.5,9.00,13.5,18,22.5 NTRs bound onto the cargo surface. As the surface density of the transport receptors is increased, the resulting size of the cargo-NTR complex is increased, resulting in a larger exclusion of nups from the cargo. When the cargo is covered in transport receptors, there is a essentially a 16 nm increase in the diameter of the resulting complex.

Once more, we measure the free energy change as we drag particles through the pore. There is now an extra degree of freedom to consider in our calculations; the surface density of transport receptors. However, by looking at our previous results, there are certain values of the parameters that we know do not correspond to a viable pore, such as at low ϵ_{pp} when the pores would be leaky

to inert particles.

The cargo transport curves with different values of the surface density and ϵ_{pp} and ϵ_{pf} are shown in figure 7.7

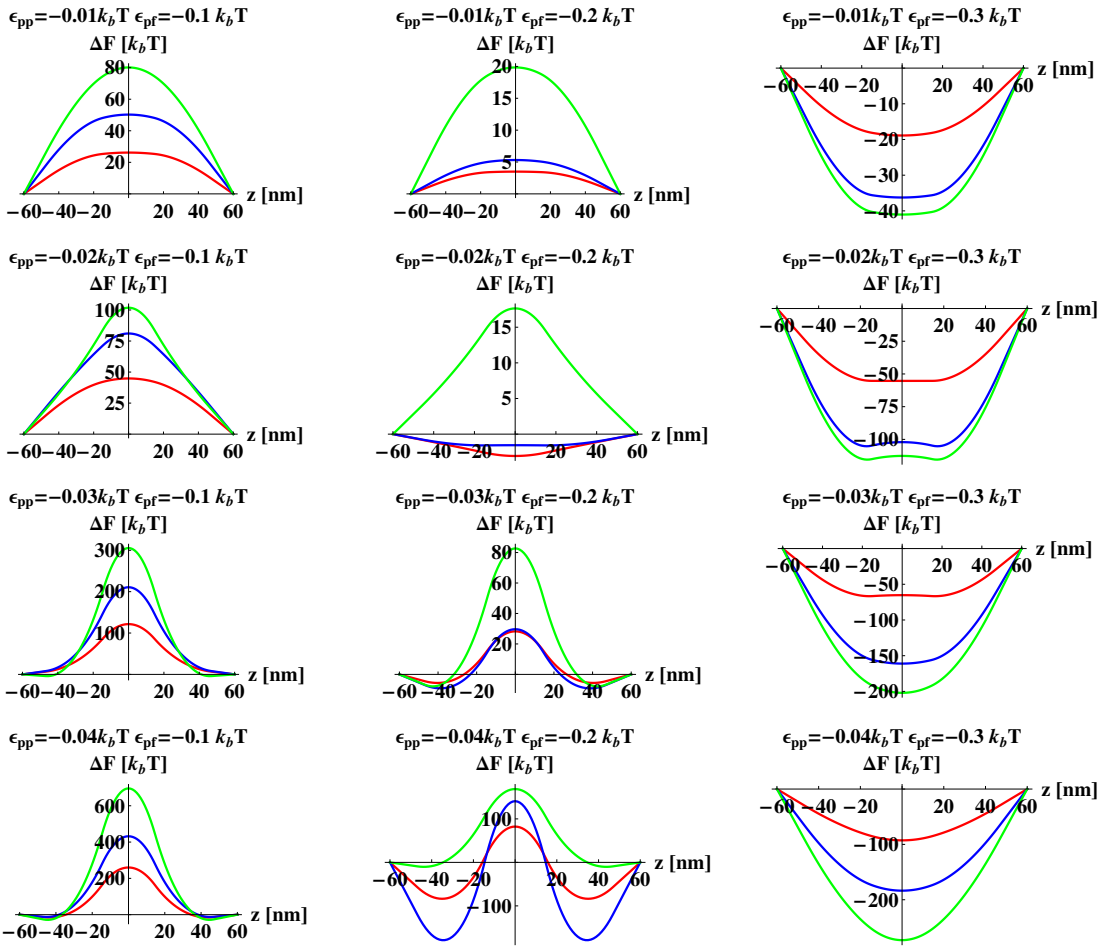

Figure 7.7: Changes in free energy for moving a 8 nm diameter cargo through the pore along the central axis, with different values of surface density of absorbed NTRs. Red corresponds to 2 NTRs on the surface, blue is 4, and green is 6. These free energy curves therefore describe complexes which can be up to 24 nm in length. We look at the free energy curves presented for different values of ϵ_{pp} and ϵ_{pf}.

The free energy curves show that we see similar distinction of free energy curves that we have observed before. That is to say: potential barriers to transport, double wells corresponding to a preference of the cargoes to sit on the surface and potential wells which mean that the cargoes like to enter into the pore. The impact of increasing or decreasing the surface density can be seen from what type of free energy curve is present. For instance for $\epsilon_{pp} = 0.03k_bT$ and $\epsilon_{pf} = 0.1k_bT$ the free energy curve is a barrier at a surface density of $\sigma_s = 0.01$. If the surface density is increased further,

the size of the barrier increases further. In these states, the strength of the nup-NTR interaction is not strong enough to overcome the effect of displacing the centrally placed polymers. As ϵ_{pf} is increased further, then eventually well states are observed. This confirms the finding stated in the section on NTR transport that the strength of NTR-nup interactions must be significantly stronger than the nup-nup interactions. These interaction parameters (such as $\epsilon_{pp} = 0.03$ and $\epsilon_{pf} = 0.1$) can therefore be thought of as non-viable for transport. It is possible to refine these calculations even further by changing the surface density of NTRs to get the optimum surface density for transport.

These calculations can be performed at larger (6nm) cargo radii. As can be seen in figure 7.8

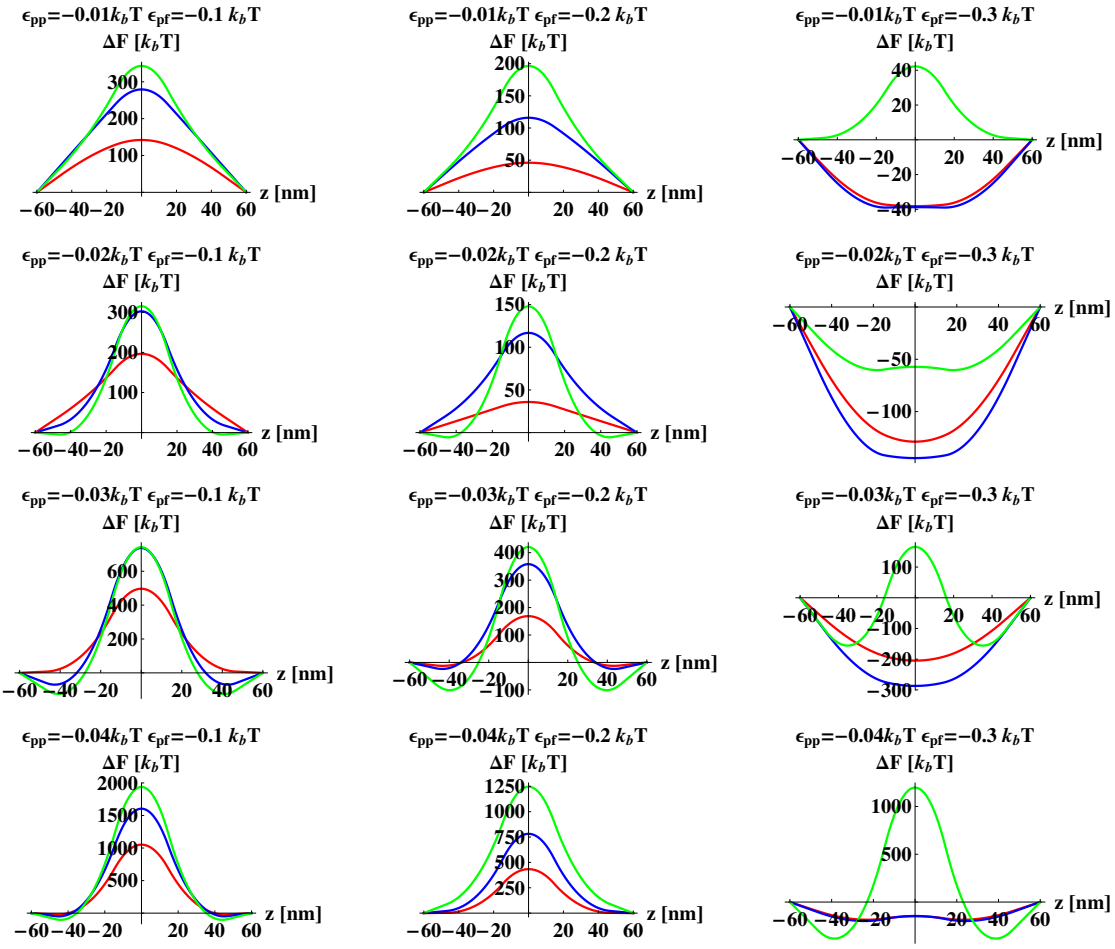

Figure 7.8: Changes in free energy at different $\epsilon_{pp}, \epsilon_{pf}$ for moving a 12 nm diameter cargo through the pore, with different values of surface density of absorbed NTRs. Red corresponds to 4.5 NTRs on the cargo surface, blue is 9, and green is 13.5. These full complexes could be up to 28 nm in diameter, a significant proportion of the nuclear pore complex diameter.

Similar phases can be observed in figure 7.8 as were seen in figure 7.7. There exist the same kind of free energy curves that we have categorised before (wells, barriers and double wells). Despite the increase in the cargo complex diameter, these cargoes of larger diameter can still go through if the surface density of NTRs is in the right range. Experimental results corroborate these findings well. The NPC is capable of allowing through even very large cargoes [15, 99]. We interpret this through the surface density of NTRs. Even very large cargoes should be able to get through if they are bound to an appropriate number of NTRs.

7.5 Viability of different intermolecular interaction parameters for the functional NPCs

In this section we summarise all the results so far using the criteria we defined at the beginning to define a viable NPC. To determine whether a specific free energy curve corresponds to a viable or non-viable NPC structure we use the following conventions:

- We take the value of 30 k_bT as the size for a barrier to be effective. I.e. barrier crossing is a event rare enough to consider the barrier impermeable. We take this value from the simple value of the rate crossing defined in equation 7.3 and use a physiologically reasonable value of the attempt frequency. Using the simple form of the barrier crossing rate, we know that a barrier of $30k_bT$ corresponds to roughly 0.1 crossings per second. Functional nuclear pores cannot leak more than this[13].

- NTR bound cargoes and NTRs should not face potential barriers. There remains a question of interpretation of the free energy curves which are potential wells for NTRs and cargoes. However, this situation at least means that cargoes and NTRs are able to enter into the pore. It could be that a physiological factor that we have thus far ignored, such as the action of RanGTP on the NTR-FG or NTR-cargo interaction plays a key role in allowing cargoes and NTRs to leave the NPC.

Using these conventions and the criteria for viability defined in the opening of this chapter, we represent graphically which values of ϵ_{pp} and ϵ_{pf} result in a viable pore.

We represent the 4 different criteria we have considered in a square as follows:

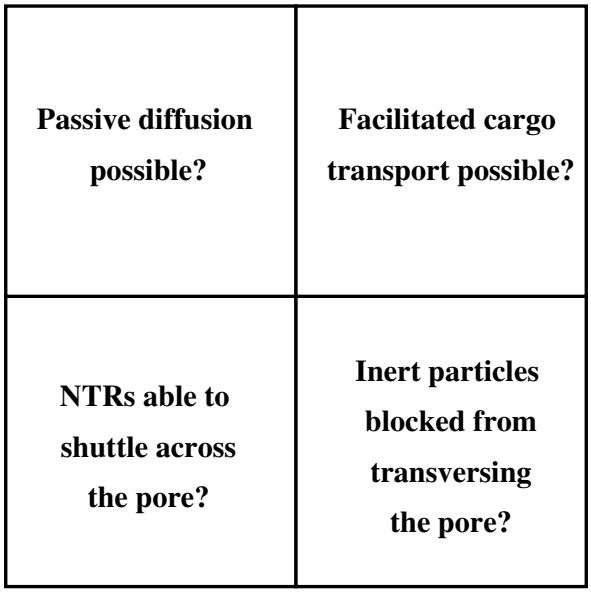

Figure 7.9: Key questions regarding NPC functionality. Passive diffusion is determined by barriers facing inert particles below the size limit being below the $30k_bT$ barrier size. Inert particles blocked is measured in the same way, i.e the barrier facing inert particles above the size limit is greater than 30 k_bT. Cargo transport and NTR transport are determined by the absence of any potential barriers greater than $30k_bT$ to the presented particles.

We then plot an array of these squares at the different values of the interactions we have considered. If the answer to the question is true (functional) then the square is white. If the answer to the question is false (leading to non-functional aspects) then the square is shaded red. The functionality map is shown in figure 7.10.

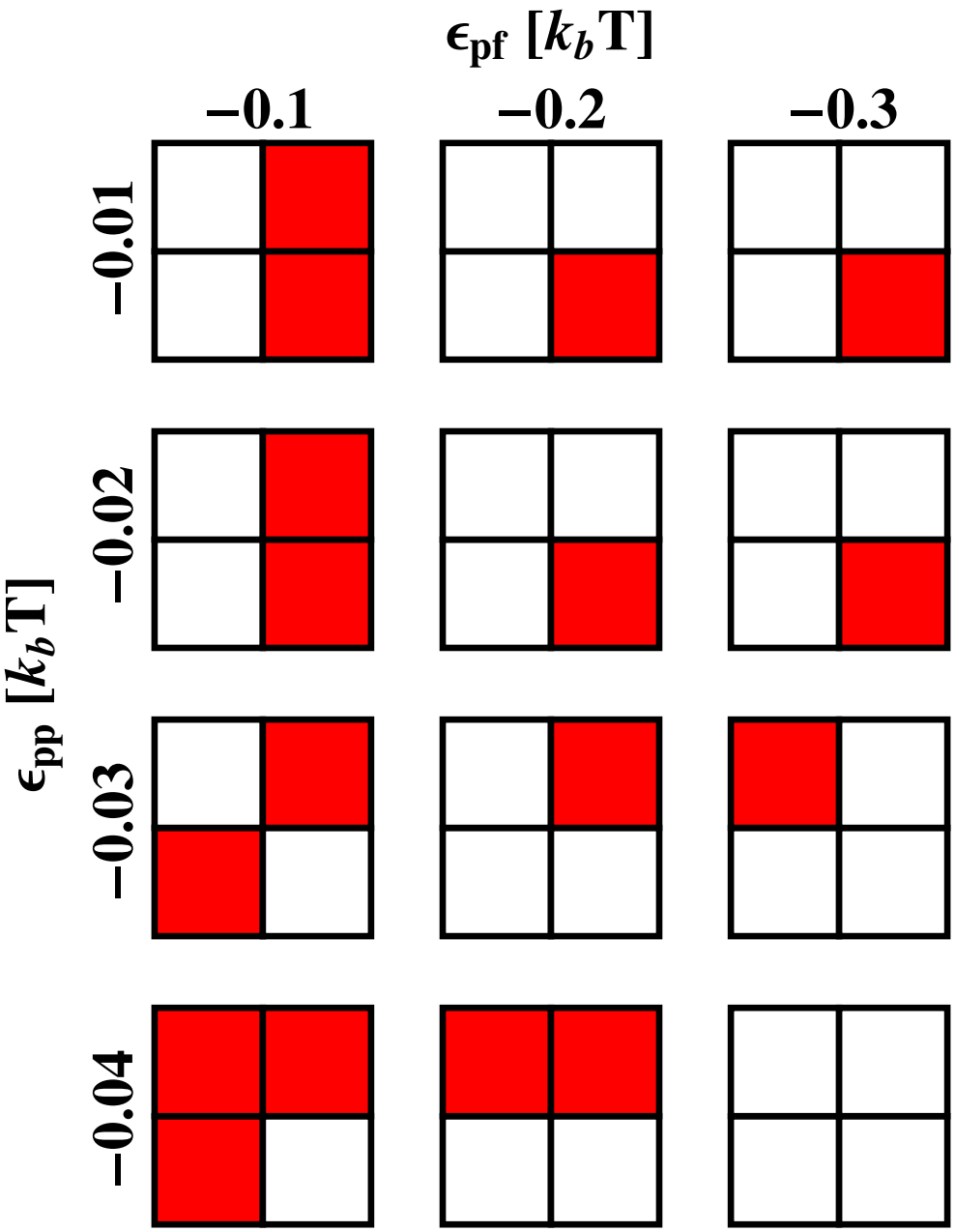

Figure 7.10: Functionality map of NPC transport at different interaction parameters. Each row corresponds to a value of ϵ_{pp} going from 0.01 to 0.04 k_bT and each column corresponds to a different value of ϵ_{pf} going from 0.1 to $0.3k_bT$. The square is shaded red or white depending on whether the functional aspects outlined in 7.9 are present or not. In general, the less red in each square, the more viable those particular interaction parameters are in explaining NPC functionality.

As can be seen from the figure 7.10, there is only one parameter set where all of the quadrants of the square are white. This is at $\epsilon_{pp} = 0.04$ and $\epsilon_{pf} = 0.3k_bT$. Therefore by elimination we suggest that this parameter set is the one best suited for transport. Considering the previous chapter where we attempted to determine which interaction parameters best agree with the experiment, the parameters we found to coincide with functional NPCs match quite well. The range of our exploration of transport was somewhat limited due to convergence problems we had when performing calculations at larger interaction parameters ($\epsilon_{pp} > 0.04k_bT$ and $\epsilon_{pf} > 0.3k_bT$. It could be possible that transport measurements at these larger parameters sets would also result in functional pores.

The physically interesting feature of the density profiles at $\epsilon_{pp} = 0.04$ and $\epsilon_{pf} = 0.3k_bT$ is that the centre of the pore is blocked with NTRs. As has been mentioned previously, the hypothesis that the NTRs are a vital component of the NPC permeability barrier is one that has been gaining traction [72]. Our transport measurements, with caveats, seem to support this hypothesis. Even thinking in very simple terms, the fact that the concentration of transport receptors in the NPC is orders of magnitude higher than the cytoplasmic concentration would imply that they have a large physical effect on the structure of the NPC. These structural changes can lead to different permeability barriers.

We have proceeded by elimination, and shown the scenarios where functional transport cannot occur. For instance, weakly interacting polymers do not form an effective barrier against inert particles. In addition, there is a need for there to be strong interactions between the polymers and the NTRs. Whilst the latter has been known for some time, the former (polymer-polymer interactions) is still contentious. For example, the entropic brush model does not require there to be strong interactions between the nups for a permeability barrier to be present. Our findings indicate that this is not sufficient to ensure pore functionality, as the free energy cost of an inert cargo to travel through the centre of the pore is not large enough to prevent leakage.

Previous work has focussed on whether the permeability barrier is enthalpic or entropic in nature[20, 13]. These transport measurements suggest that the main requirement for barriers is a reasonably attractive potential between the polymers.

In summary, in this chapter we have attempted to discern which parameters best agree with the functionality of NPC. We have explored transport through the central axis of the NPC of particles of various sizes and interactions, corresponding to different cargoes. By measuring the free energy

curves presented to these cargoes, we are able to determine what type of polymer structure best explains the physiological function of the NPC.

Chapter 8

Concluding Remarks and Outlook

In this thesis, we have taken a step by step approach to building a model of NPC function. We explored the state of current NPC modelling[100] before constructing our mean field model of the NPC[101]. We then used the mean field model with many different parameter choices in order to establish the phase behaviour of the fg-nups in the NPC. Due to uncertainty about NPC interactions, as well as the simplifications of our model, it was vital to explore our model over many different parameters.

This lead to our initial conclusions regarding the bimodality of cylindrically bound tethered polymers. Whilst the bimodality is lessened when we consider more realistic polymers arrangements, it was important in demonstrating that even small changes in interaction parameters can lead to large changes in polymer structure, suggesting that even a small number of NTRs could have a large impact on the polymer arrangement in the pore.

We tested this by including NTRs explicitly in our model[102]. By adding NTRs we were able to explicitly measure the effect of the NTRs on the polymers. In addition to the central and the wall phase identified previously, there also exist polymer-NTR networks, where the NTRs are arranged in a lattice. We showed in this model that the presence of NTRs is sufficient to cause large conformational changes in the nups.

We have also devoted a chapter to examining the azimuthal symmetry assumption present in this work, and whether the use of this assumption changes our qualitative assumptions.

Finally, we compare our model to experimental measurements of nups and NPC, and determine which of our model parameters best agree with known aspects of nuclear pore selectivity.

Given more time, this work could be expanded in several ways. Firstly, more steps can be

taken in an attempt to more faithfully reproduce the structural heterogeneity of the the FG nups. It would be important to demonstrate for a variety of parameter choices that our qualitative assumptions are not affected by structural heterogeneity.

Repeating the theoretical AFM indentation experiments with NTRs included would also be important in establishing that a central plug is consistent with a condensation of NTRs. In addition to this, expanding the range of the transport experiments to a greater number of parameters to test whether the point we have identified as acceptable for transport is unique or just one of many points. The effect of Ran has thus far been ignored in our models. Ran is vital for NPC directionality as well as freeing cargoes from NTRs. RanGTP could possibly be included in our model by having a spatially dependent interaction strength between the NTRs and the FG repeats.

Another are that could be improved is extending the calculations to three dimensions. Which is conceptually easy but computationally difficult. This would allow studies of translocation pathways beyond the just the central axis. In general, extending this work to include dynamics properly would require the formulation of a dynamic density functional theory for the polymer-NTR mixture, though this is theoretically challenging.

In the context of our work, the currently favoured approach of modelling the NPC remains molecular dynamics simulations[42, 34, 35]. As computational speed advances even further this trend will continue. The advantage of the mean field method is in its simplicity and ability to motivate intuitive arguments about NPC function. We have shown that even a very simplistic model of the NPC is still able to capture many of the NPC's functional aspects, as well as having reasonable agreement with experiment. This is despite the fact that almost all detailed molecular detail has been ignored. We hope our work can develop intuitive insight into the NPC, as well as helping the understanding and fabrication of simple polymer-coated nanopore devices.

References

[1] A. Hoelz, E. W. Debler, and G. Blobel, "The structure of the nuclear pore complex," *Annu. Rev. Biochem.*, vol. 80, no. 1, pp. 613–643, 2011.

[2] D. Stoffler, B. Feja, B. Fahrenkrog, J. Walz, D. Typke, and U. Aebi, "Cryo-electron tomography provides novel insights into nuclear pore architecture: Implications for nucleocytoplasmic transport," *J. Mol. Biol.*, vol. 328, no. 1, pp. 119 – 130, 2003.

[3] M. Beck, F. Förster, M. Ecke, J. M. Plitzko, F. Melchior, G. Gerisch, W. Baumeister, and O. Medalia, "Nuclear pore complex structure and dynamics revealed by cryoelectron tomography," *Science*, vol. 306, no. 5700, pp. 1387–1390, 2004.

[4] S. G. Brohawn, J. R. Partridge, J. R. Whittle, and T. U. Schwartz, "The nuclear pore complex has entered the atomic age," *Structure*, vol. 17, no. 9, pp. 1156 – 1168, 2009.

[5] D. Görlich and U. Kutay, "Transport between the cell nucleus and the cytoplasm," *Annu. Rev. Cell Dev. Bi.*, vol. 15, no. 1, pp. 607–660, 1999. PMID: 10611974.

[6] D. Görlich, N. Panté, U. Kutay, U. Aebi, and F. R. Bischoff, "Identification of different roles for rangdp and rangtp in nuclear protein import," *EMBO J.*, vol. 15, no. 20, pp. 5584–5594, 1996.

[7] E. Izaurralde, U. Kutay, C. von Kobbe, I. W. Mattaj, and D. Görlich, "The asymmetric distribution of the constituents of the ran system is essential for transport into and out of the nucleus," *EMBO J.*, vol. 16, no. 21, pp. 6535–6547, 1997.

[8] L. A. Strawn, T. Shen, N. Shulga, D. S. Goldfarb, and S. R. Wente, "Minimal nuclear pore complexes define fg repeat domains essential for transport," *Nat. Cell. Biol.*, vol. 6, no. 3, pp. 197–206, 2004.

[9] M. K. Iovine, J. L. Watkins, and S. R. Wente, "The glfg repetitive region of the nucleoporin nup116p interacts with kap95p, an essential yeast nuclear import factor.," *J. Cell. Biol.*, vol. 131, no. 6, pp. 1699–1713, 1995.

[10] M. Rexach and G. Blobel, "Protein import into nuclei: association and dissociation reactions involving transport substrate, transport factors, and nucleoporins," *Cell*, vol. 83, no. 5, pp. 683 – 692, 1995.

[11] R. Bayliss, K. Ribbeck, D. Akin, H. M. Kent, C. M. Feldherr, D. Görlich, and M. Stewart, "Interaction between ntf2 and xfxfg-containing nucleoporins is required to mediate nuclear import of rangdp," *J. Mol. Biol.*, vol. 293, no. 3, pp. 579 – 593, 1999.

[12] A. A. Labokha, S. Gradmann, S. Frey, B. B. Hulsmann, H. Urlaub, M. Baldus, and D. Görlich, "Systematic analysis of barrier-forming fg hydrogels from xenopus nuclear pore complexes," *EMBO J.*, vol. 32, no. 2, pp. 204–218, 2012.

[13] K. Ribbeck and D. Görlich, "Kinetic analysis of translocation through nuclear pore complexes," *EMBO J.*, vol. 20, no. 6, pp. 1320–1330, 2001.

[14] U. F. Greber and A. Fassati, "Nuclear import of viral dna genomes," *Traffic*, vol. 4, no. 3, pp. 136–143, 2003.

[15] S. Au and N. Panté, "Nuclear transport of baculovirus: Revealing the nuclear pore complex passage," *J. Struct. Biol.*, vol. 177, no. 1, pp. 90 – 98, 2012.

[16] W. Yang, J. Gelles, and S. M. Musser, "Imaging of single-molecule translocation through nuclear pore complexes," *Proc. Natl. Acad. Sci. USA*, vol. 101, no. 35, pp. 12887–12892, 2004.

[17] U. Kubitscheck, D. Grünwald, A. Hoekstra, D. Rohleder, T. Kues, J. P. Siebrasse, and R. Peters, "Nuclear transport of single molecules: dwell times at the nuclear pore complex," *J. Cell Biol.*, vol. 168, no. 2, pp. 233–243, 2005.

[18] B. Naim, D. Zbaida, S. Dagan, R. Kapon, and Z. Reich, "Cargo surface hydrophobicity is sufficient to overcome the nuclear pore complex selectivity barrier," *EMBO J.*., vol. 28, no. 18, pp. 2697 – 2705, 2009.

[19] B. B. Hülsmann, A. A. Labokha, and D. Görlich, "The permeability of reconstituted nuclear pores provides direct evidence for the selective phase model," *Cell*, vol. 150, no. 4, pp. 738 – 751, 2012.

[20] R. Y. H. Lim, B. Fahrenkrog, J. Koser, K. Schwarz-Herion, J. Deng, and U. Aebi, "Nanomechanical basis of selective gating by the nuclear pore complex," *Science*, vol. 318, no. 5850, pp. 640–643, 2007.

[21] R. Peters, "Translocation through the nuclear pore complex: Selectivity and speed by reduction-of-dimensionality," *Traffic*, vol. 6, no. 5, pp. 421–427, 2005.

[22] M. Tagliazucchi and I. Szleifer, "Stimuli-responsive polymers grafted to nanopores and other nano-curved surfaces: structure, chemical equilibrium and transport," *Soft Matter*, vol. 8, pp. 7292–7305, 2012.

[23] S. P. Adiga and D. W. Brenner, "Stimuli-responsive polymer brushes for flow control through nanopores," *J. Funct. Biom.*, vol. 3, no. 2, pp. 239–256, 2012.

[24] F. Alber, S. Dokudovskaya, L. M. Veenhoff, W. Zhang, J. Kipper, D. Devos, A. Suprapto, O. Karni-Schmidt, R. Williams, B. T. Chait, A. Sali, and M. P. Rout, "The molecular architecture of the nuclear pore complex," *Nature*, vol. 450, no. 7170, pp. 695–701, 2007.

[25] J. Yamada, J. L. Phillips, S. Patel, G. Goldfien, A. Calestagne-Morelli, H. Huang, R. Reza, J. Acheson, V. V. Krishnan, S. Newsam, A. Gopinathan, E. Y. Lau, M. E. Colvin, V. N. Uversky, and M. F. Rexach, "A bimodal distribution of two distinct categories of intrinsically disordered structures with separate functions in fg nucleoporins," *Mol. Cell. Proteomics*, vol. 9, pp. 2205–2224, OCT 2010.

[26] T. Bickel and R. Bruinsma, "The nuclear pore complex mystery and anomalous diffusion in reversible gels," *Biophys. J.*, vol. 83, no. 6, pp. 3079–3087, 2002.

[27] B. Nielsen, C. Jeppesen, and J. H. Ipsen, "Managing free-energy barriers in nuclear pore transport," *J. Biol. Phys.*, vol. 32, pp. 465–472, 2006.

[28] A. Zilman, S. Di Talia, B. T. Chait, M. P. Rout, and M. O. Magnasco, "Efficiency, selectivity, and robustness of nucleocytoplasmic transport," *PLoS Comput. Biol.*, vol. 3, p. e125, 07 2007.

[29] A. Zilman, S. Di Talia, T. Jovanovic-Talisman, B. T. Chait, M. P. Rout, and M. O. Magnasco, "Enhancement of transport selectivity through nano-channels by non-specific competition," *PLoS Comput Biol*, vol. 6, p. e1000804, 06 2010.

[30] D. Chatterjee and B. J. Cherayil, "Subdiffusion as a model of transport through the nuclear pore complex," *J. Chem. Phys.*, vol. 135, no. 15, p. 155101, 2011.

[31] V. Melnikov, "The kramers problem: Fifty years of development," *Phys. Rep.*, vol. 209, no. 12, pp. 1 – 71, 1991.

[32] M. Karplus and J. A. McCammon, "Molecular dynamics simulations of biomolecules," *Nat. Struct. Mol. Biol.*, vol. 9, no. 9, pp. 646–652, 2002.

[33] L. Miao and K. Schulten, "Transport-related structures and processes of the nuclear pore complex studied through molecular dynamics," *Structure*, vol. 17, no. 3, pp. 449–459, 2009.

[34] J. S. Mincer and S. M. Simon, "Simulations of nuclear pore transport yield mechanistic insights and quantitative predictions," *Proc. Natl. Acad. Sci. USA*, vol. 108, no. 31, pp. E351–E358, 2011.

[35] R. Moussavi-Baygi, Y. Jamali, R. Karimi, and M. R. K. Mofrad, "Biophysical coarse-grained modeling provides insights into transport through the nuclear pore complex," *Biophys. J.*, vol. 100, pp. 1410–1419, MAR 16 2011.

[36] T. Kustanovich and Y. Rabin, "Metastable network model of protein transport through nuclear pores," *Biophys. J.*, vol. 86, pp. 2008–2016, APR 2004.

[37] J. N. Israelachvili, *Intermolecular and Surface Forces.* Academic Press, 3rd ed., 2011.

[38] S. Frey, R. P. Richter, and D. Görlich, "Fg-rich repeats of nuclear pore proteins form a three-dimensional meshwork with hydrogel-like properties," *Science*, vol. 314, no. 5800, pp. 815–817, 2006.

[39] K. Ribbeck and D. Görlich, "The permeability barrier of nuclear pore complexes appears to operate via hydrophobic exclusion," *EMBO J.*, vol. 21, no. 11, pp. 2664–2671, 2002.

[40] A. Kramer, I. Liashkovich, Y. Ludwig, and V. Shahin, "Atomic force microscopy visualises a hydrophobic meshwork in the central channel of the nuclear pore," *Pflug. Arch. Eur. J. Phys.*, vol. 456, pp. 155–162, 2008.

[41] S. P. Adiga and D. W. Brenner, "Flow control through polymer-grafted smart nanofluidic channels: molecular dynamics simulations," *Nano Lett.*, vol. 5, no. 12, pp. 2509–2514, 2005.

[42] D. Ando, R. Zandi, Y. Kim, M. Colvin, M. Rexach, and A. Gopinathan, "Nuclear pore complex protein sequences determine overall copolymer brush structure and function," *Biophysical Journal*, vol. 106, no. 9, pp. 1997 – 2007, 2014.

[43] T. A. Isgro and K. Schulten, "Binding dynamics of isolated nucleoporin repeat regions to importin-," *Structure*, vol. 13, no. 12, pp. 1869 – 1879, 2005.

[44] T. A. Isgro and K. Schulten, "Association of nuclear pore fg-repeat domains to ntf2 import and export complexes," *J. Mol. Biol.*, vol. 366, no. 1, pp. 330 – 345, 2007.

[45] T. A. Isgro and K. Schulten, "Cse1p-binding dynamics reveal a binding pattern for fg-repeat nucleoporins on transport receptors," *Structure*, vol. 15, no. 8, pp. 977 – 991, 2007.

[46] L. Miao and K. Schulten, "Probing a structural model of the nuclear pore complex channel through molecular dynamics," *Biophys. J.*, vol. 98, no. 8, pp. 1658 – 1667, 2010.

[47] R. Evans, "The nature of the liquid-vapour interface and other topics in the statistical mechanics of non-uniform, classical fluids," *Adv. Phys.*, vol. 28, no. 2, pp. 143–200, 1979.

[48] O. Peleg, M. Tagliazucchi, M. Kröger, Y. Rabin, and I. Szleifer, "Morphology control of hairy nanopores," *ACS Nano*, vol. 5, no. 6, pp. 4737–4747, 2011.

[49] N. Metropolis, "Equation of state calculations by fast computing machines," *J. Chem. Phys.*, vol. 21, no. 6, 1953.

[50] A. G. Koutsioubas, N. Spiliopoulos, D. L. Anastassopoulos, A. A. Vradis, and C. Toprakcioglu, "Formation of polymer brushes inside cylindrical pores: A computer simulation study," *J. Chem. Phys.*, vol. 131, no. 4, p. 044901, 2009.

[51] R. Wang, P. Virnau, and K. Binder, "Conformational properties of polymer mushrooms under spherical and cylindrical confinement," *Macromol. Theory Simul.*, vol. 19, no. 5, pp. 258–268, 2010.

[52] D. I. Dimitrov, A. Milchev, and K. Binder, "Polymer brushes in cylindrical pores: Simulation versus scaling theory," *J. Chem. Phys.*, vol. 125, no. 3, p. 034905, 2006.

[53] S. A. Egorov, A. Milchev, L. Klushin, and K. Binder, "Structural properties of concave cylindrical brushes interacting with free chains," *Soft Matter*, vol. 7, pp. 5669–5676, 2011.

[54] M. Tagliazucchi, O. Peleg, M. Kröger, Y. Rabin, and I. Szleifer, "Effect of charge, hydrophobicity, and sequence of nucleoporins on the translocation of model particles through the nuclear pore complex," *Proc. Natl. Acad. Sci.*, p. in press, 2013.

[55] P. Hohenberg and W. Kohn, "Inhomogeneous electron gas," *Phys. Rev.*, vol. 136, pp. B864–B871, Nov 1964.

[56] A. Isihara, "The gibbs-bogoliubov inequality dagger," *J. Phys. A: Gen. Phys.*, vol. 1, 1968.

[57] V. Kalikmanov, *Statistical Physics of Fluids: Basic Concepts and Applications*. Springer, 1st ed., 2001.

[58] R. Y. H. Lim, N.-P. Huang, J. Koser, J. Deng, K. H. A. Lau, K. Schwarz-Herion, B. Fahrenkrog, and U. Aebi, "Flexible phenylalanine-glycine nucleoporins as entropic barriers to nucleocytoplasmic transport," *Proc. Natl. Acad. Sci. USA*, vol. 103, no. 25, pp. 9512–9517, 2006.

[59] R. Peters, "Translocation through the nuclear pore: Kaps pave the way," *BioEssays*, vol. 31, no. 4, pp. 466–477, 2009.

[60] S. R. Wente and M. P. Rout, "The nuclear pore complex and nuclear transport," *Cold Spring Harbor Perspect. Biol.*, vol. 2, no. 10, 2010.

[61] T. Jamali, Y. Jamali, M. Mehrbod, and M. R. K. Mofrad, "Nuclear pore complex: Biochemistry and biophysics of nucleocytoplasmic transport in health and disease," *Int. Rev. Cell Mol. Biol.*, vol. 287, pp. 233–286, 2011.

[62] G. H. Frederikson, *The Equilibrium Theory of Inhomogenous Polymers*. Oxford University Press, 1st ed., 2006.

[63] U. M. B. Marconi and P. Tarazona, "Dynamical density functional theory of liquids," *J. Chem. Phys.*, vol. 110, p. 8032, 1999.

[64] U. M. B. Marconi and S. Melchionna, "Phase space approach to dynamical density functional theory," *J. Chem. Phys.*, vol. 126, p. 184109, 2007.

[65] M. S. Wertheim, "Thermodynamic perturbation theory of polymerization," *J. Chem. Phys.*, vol. 87, no. 12, pp. 7323–7331, 1987.

[66] S. A. Egorov, "Interactions between polymer brushes in solvents of variable quality: A density functional theory study," *J. Chem. Phys.*, vol. 129, no. 6, p. 064901, 2008.

[67] A. Kramer, D. Osmanovic, J. Bailey, A. H. Harker, I. J. Ford, E. V. Orlova, G. Charras, A. Fassati, and B. W. Hoogenboom. in preparation.

[68] T. Kreer, S. Metzger, M. Müller, K. Binder, and J. Baschnagel, "Static properties of end-tethered polymers in good solution: A comparison between different models," *J. Chem. Phys.*, vol. 120, no. 8, 2004.

[69] A. Mulero, C. Galn, M. Parra, and F. Cuadros, "Equations of state for hard spheres and hard disks," in *Theory and Simulation of Hard-Sphere Fluids and Related Systems* (A. Mulero, ed.), vol. 753 of *Lecture Notes in Physics*, pp. 37–109, Springer Berlin Heidelberg, 2008.

[70] A. Paradise, M. K. Levin, G. Korza, and J. H. Carson, "Significant proportions of nuclear transport proteins with reduced intracellular mobilities resolved by fluorescence correlation spectroscopy," *J. Mol. Biol.*, vol. 365, no. 1, pp. 50 – 65, 2007.

[71] T. Jovanovic-Talisman, J. Tetenbaum-Novatt, A. S. McKenney, A. Zilman, R. Peters, M. P. Rout, and B. T. Chait, "Artificial nanopores that mimic the transport selectivity of the nuclear pore complex," *Nature*, vol. 457, no. 7232, pp. 1023–1027, 2009.

[72] R. L. Schoch, L. E. Kapinos, and R. Y. H. Lim, "Nuclear transport receptor binding avidity triggers a self-healing collapse transition in fg-nucleoporin molecular brushes," *Proc. Natl. Acad. Sci. USA*, vol. 109, no. 42, pp. 16911–16916, 2012.

[73] J. Ma, A. Goryaynov, A. Sarma, and W. Yang, "Self-regulated viscous channel in the nuclear pore complex," *Proc. Natl. Acad. Sci. USA*, vol. 109, no. 19, pp. 7326–7331, 2012.

[74] A. R. Lowe, J. J. Siegel, P. Kalab, M. Siu, K. Weis, and J. T. Liphardt, "Selectivity mechanism of the nuclear pore complex characterized by single cargo tracking," *Nature*, vol. 467, no. 7315, pp. 600–603, 2010.

[75] Y. Rosenfeld, "Free-energy model for the inhomogeneous hard-sphere fluid mixture and density-functional theory of freezing," *Phys. Rev. Lett.*, vol. 63, pp. 980–983, Aug 1989.

[76] R. Roth, "Fundamental measure theory for hard sphere mixtures, a review," *J. Phys. Condens. Matter*, vol. 22, no. 6, p. 063102, 2010.

[77] Y.-X. Yu and J. Wu, "Density functional theory for inhomogeneous mixtures of polymeric fluids," *The Journal of Chemical Physics*, vol. 117, no. 5, pp. 2368–2376, 2002.

[78] A. Malijevsky, "Fundamental measure theory in cylindrical geometry," *The Journal of Chemical Physics*, vol. 126, no. 13, p. 134710, 2007.

[79] N. J. Mariani, C. Mocciaro, M. A. Campesi, and G. F. Barreto, "On the computation of fundamental measure theory in pores with cylindrical symmetry," *The Journal of Chemical Physics*, vol. 132, no. 20, p. 204104, 2010.

[80] J. K. Forwood, A. Lange, U. Zachariae, M. Marfori, C. Preast, H. Grubmller, M. Stewart, A. H. Corbett, and B. Kobe, "Quantitative structural analysis of importin- flexibility: Paradigm for solenoid protein structures," *Structure*, vol. 18, no. 9, pp. 1171 – 1183, 2010.

[81] S. Jakel, J.-M. Mingot, P. Schwarzmaier, E. Hartmann, and D. Görlich, "Importins fulfil a dual function as nuclear import receptors and cytoplasmic chaperones for exposed basic domains," *EMBO J.*, vol. 21, no. 3, pp. 377–386, 2002.

[82] E. Grossman, O. Medalia, and M. Zwerger, "Functional architecture of the nuclear pore complex," *Annual Review of Biophysics*, vol. 41, no. 1, pp. 557–584, 2012. PMID: 22577827.

[83] O. Peleg and R. Y. H. Lim, "Converging on the function of intrinsically disordered nucleoporins in the nuclear pore complex," *Biol. Chem.*, vol. 391, no. 7, pp. 719–730, 2010.

[84] Y. Wu, G. Cheng, K. Katsov, S. W. Sides, J. Wang, J. Tang, G. H. Fredrickson, M. Moskovits, and G. D. Stucky, "Composite mesostructures by nano-confinement," *Natur. Mat.*, vol. 3, pp. 816–822, 2004.

[85] S. A. Adam, R. S. Marr, and L. Gerace, "Nuclear protein import in permeabilized mammalian cells requires soluble cytoplasmic factors.," *J. Cell. Biol.*, vol. 111, no. 3, pp. 807–816, 1990.

[86] A. Goryaynov, J. Ma, and W. Yang, "Single-molecule studies of nucleocytoplasmic transport: from one dimension to three dimensions," *Integr. Biol.*, vol. 4, pp. 10–21, 2012.

[87] W. Yang and S. M. Musser, "Nuclear import time and transport efficiency depend on importin concentration," *J. Cell. Biol.*, vol. 174, no. 7, pp. 951–961, 2006.

[88] D. Grünwald and R. H. Singer, "In vivo imaging of labelled endogenous [bgr]-actin mrna during nucleocytoplasmic transport," *Nature*, vol. 467, no. 7315, pp. 604–607, 2010.

[89] A. Mor, S. Suliman, R. Ben-Yishay, S. Yunger, Y. Brody, and Y. Shav-Tal, "Dynamics of single mrnp nucleocytoplasmic transport and export through the nuclear pore in living cells," *Nat. Cell. Biol.*, vol. 12, no. 6, pp. 543–552, 2010.

[90] R. L. Adams and S. R. Wente, "Uncovering nuclear pore complexity with innovation," *cell*, vol. 152, no. 6, pp. 1218–1221, 2013.

[91] N. B. Eisele, S. Frey, J. Piehler, D. Grlich, and R. P. Richter, "Ultrathin nucleoporin phenylalanineglycine repeat films and their interaction with nuclear transport receptors," *EMBO reports*, vol. 11, no. 5, pp. 366–372, 2010.

[92] N. B. Eisele, F. I. Andersson, S. Frey, and R. P. Richter, "Viscoelasticity of thin biomolecular films: A case study on nucleoporin phenylalanine-glycine repeats grafted to a histidine-tag capturing qcm-d sensor," *Biomacromolecules*, vol. 13, no. 8, pp. 2322–2332, 2012.

[93] R. R. Netz and M. Schick, "Polymer brushes: from self-consistent field theory to classical theory," *Macromolecules*, vol. 31, no. 15, pp. 5105–5122, 1998.

[94] R. Bayliss, S. W. Leung, R. P. Baker, B. Quimby, A. H. Corbett, and M. Stewart, "Structural basis for the interaction between ntf2 and nucleoporin fxfg repeats," *The EMBO Journal*, vol. 21, no. 12, pp. 2843–2853, 2002.

[95] D. Mohr, S. Frey, T. Fischer, T. Gttler, and D. Grlich, "Characterisation of the passive permeability barrier of nuclear pore complexes," *The EMBO Journal*, vol. 28, no. 17, pp. 2541–2553, 2009.

[96] J. Wu, A. H. Corbett, and K. M. Berland, "The intracellular mobility of nuclear import receptors and {NLS} cargoes," *Biophysical Journal*, vol. 96, no. 9, pp. 3840 – 3849, 2009.

[97] S. Kose, N. Imamoto, T. Tachibana, T. Shimamoto, and Y. Yoneda, "Ran-unassisted nuclear migration of a 97-kd component of nuclear poretargeting complex," *The Journal of Cell Biology*, vol. 139, no. 4, pp. 841–849, 1997.

[98] S. Nakielny and G. Dreyfuss, "Import and export of the nuclear protein import receptor transportin by a mechanism independent of {GTP} hydrolysis," *Current Biology*, vol. 8, no. 2, pp. 89 – 95, 1998.

[99] N. Pante and M. Kann, "Nuclear pore complex is able to transport macromolecules with diameters of 39 nm," *Mol. Biol. Cell*, vol. 13, no. 2, 2002.

[100] D. Osmanović, A. Fassati, I. J. Ford, and B. W. Hoogenboom, "Physical modelling of the nuclear pore complex," *Soft Matter*, vol. 9, pp. 10442–10451, 2013.

[101] D. Osmanovic, J. Bailey, A. H. Harker, A. Fassati, B. W. Hoogenboom, and I. J. Ford, "Bistable collective behavior of polymers tethered in a nanopore," *Phys. Rev. E*, vol. 85, p. 061917, 2012.

[102] D. Osmanovic, I. Ford, and B. Hoogenboom, "Model inspired by nuclear pore complex suggests possible roles for nuclear transport receptors in determining its structure," *Biophysical Journal*, vol. 105, no. 12, pp. 2781 – 2789, 2013.